6. Surface and Interface Characterization

While the *bulk material properties* treated in Part C of this handbook are obviously important, the surface characteristics of materials are also of great significance. They are responsible for the appearances of materials and surface phenomena, and they have a crucial influence on the interactions of materials with gases or fluids (in corrosion, for example; Chap. 12), contacting solids (as in friction and wear; Chap. 13) or biospecies (Chap. 14), and materials–environment interactions (Chap. 15). Surface and interface characterization have been important topics for very many years. Indeed, it was known in antiquity that impurities could be detrimental to the quality of metals, and that keying and contamination were important to adhesion in architecture and also in the fine arts. In contemporary technologies, surface modification or functional coatings are frequently used to tailor the processing of advanced materials. Some components, such as quantum-well devices and x-ray mirrors, are composed of multilayers with individual layer thicknesses in the low nanometer range. Quality assurance of industrial processes, as well as the development of advanced surface-modified or coated components, requires chemical information on material surfaces and (buried) interfaces with high sensitivity and high lateral and depth resolution. In this chapter we present the methods applicable to the chemical and physical characterization of surfaces and interfaces.

This chapter covers the three main techniques of surface chemical analysis: Auger electron spectroscopy (AES), x-ray photoelectron spectroscopy (XPS), and secondary ion mass spectrometry (SIMS), which are all still rapidly developing in terms of instrumentation, standards, and applications. AES is excellent for elemental analysis at spatial resolutions down to 10 nm, and XPS can define chemical states down to 10 µm. Both analyze the outermost atom layers and, with sputter depth profiling, layers up to 1 µm thick.

Dynamic SIMS incorporates depth profiling and can detect atomic compositions significantly below 1 ppm. Static SIMS retains this high sensitivity for the surface atomic or molecular layer but provides chemistry-related details not available with AES or XPS. New reference data, measurement standards, and documentary standards from ISO will continue to be developed for surface chemical analysis over the coming years.

The chapter also discusses surface physical analysis (topography characterization), which encompasses measurement, visualization, and quantification. This is critical to both component form and surface finish at macro-, micro-, and nanoscales. The principal methods of surface topography measurement are stylus profilometry, optical scanning techniques, and scanning probe microscopy (SPM). These methods, based on acquiring topography data from point-by-point scans, give quantitative information on surface height with respect to position. The integral methods, which are based on a different approach, produce parameters that represent some average property of the surface under examination. Measurement methods, as well as their application and limitations, are briefly reviewed, including standardization and traceability issues.

6.1 Surface Chemical Analysis

The principal methods of surface chemical analysis are Auger electron spectroscopy (AES), x-ray photoelectron spectroscopy (XPS), and secondary ion mass spectrometry (SIMS). These three methods provide analyses of the outermost atomic layers at a solid surface, but each has distinct attributes which lead to each having dominance in different sectors of analysis. Additionally, each may be coupled with ion sputtering, to erode the surface whilst analyzing, in order to generate a composition depth profile. These profiles may typically be over layers up to 100 nm thick or, when required, up to 1 μm thick or more. The depth resolutions can approach atomic levels. Useful figures to remember are that an atomic layer is about 0.25 nm thick and contains about 1.6×10^{19} atoms m^{-2} or 1.6×10^{15} atoms cm^{-2}. All of the above methods operate with the samples inserted into an ultrahigh vacuum system where the base pressure is designed to be 10^{-8} Pa (10^{-10} Torr) but that, with fast throughputs or gassy samples, may degrade to 10^{-5} Pa (10^{-7} Torr). Thus, all samples need to be vacuum-compatible solids.

We shall describe the basics of each of the methods later, but it is useful, here, to outline the attributes of the methods so that the reader can focus early on their method of choice.

In Auger electron spectroscopy (AES), the exciting radiation is a focused electron beam, and in the latest instruments, resolutions ≤ 5 nm are achieved. This provides elemental analysis with detectabilities reaching 0.1%, but not at the same time as very high spatial resolution. Additionally, the higher the spatial resolution, the more robust the sample should be, since the electron beam fluence on the sample is then very high. Thus, metals, oxides, semiconductors or some ceramics are readily analyzed, although at the highest flux density the surface of compounds may be eroded. In AES, there is chemical information, but it is not as easily observed as in XPS. In XPS, the peaks are simpler and so quantification is generally more accurate, the chemical shifts are clearer, detectability is similar to in AES, but the spatial resolution is significantly poorer. Typically, ≤ 5 μm spatial resolution is the best achieved in the latest instruments. In XPS, with a lower flux of charged particles, ceramics and other insulators may be analyzed more readily than with AES, although if spatial resolution ≤ 5 μm is required, AES must generally be used, and efforts then need to be taken to avoid any charging or damage problems.

For layers with compositions that change within the outermost 8 nm, information on the layering may be obtained by XPS or angle-resolved XPS. If the compositions vary over greater depths, sputter depth profiling is used, generally with AES or, if more convenient or for particular information, with XPS. The sputtering is usually conducted in situ for AES and may be in situ or in a linked vacuum vessel for XPS.

Where greater detectability is required, as for studying dopant distributions in semiconductor device fabrication, SIMS is the technique of choice. Modern SIMS instruments have resolutions of around 100 nm, but critical to semiconductor work is the ability to detect levels as low as 0.01 ppm. In SIMS, the ion intensities

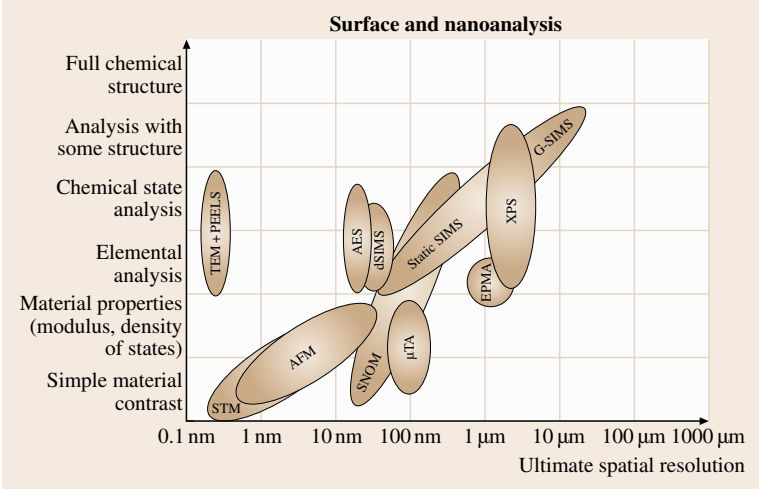

Fig. 6.1 The resolution and information content of a range of analytical methods (STM = scanning tunneling microscopy, AFM = atomic force microscopy, TEM = transmission electron microscopy, PEELS = parallel electron energy loss spectroscopy, SNOM = scanning near-field optical microscopy, μTA = microthermal analysis, EPMA = electron probe microscopy) that can be used at surfaces (after *Gilmore* et al. [6.1])

Table 6.1 Methodology selection table for surface analysis

Method	**AES**		**XPS**		**Dynamic SIMS**		**Static SIMS**	
Configuration	Traditional	High-energy resolution	Traditional	Imaging	Imaging	Depth profiling	Gas source	Liquid metal ion source
Section	Sect. 6.1.1		Sect. 6.1.2		Sect. 6.1.3		Sect. 6.1.3	
Best spatial resolution	5 nm	5 nm	20 μm	2 μm	50 nm	50 μm	5 μm	80 nm
Best depth resolution	0.3 nm	0.3 nm	0.3 nm	1.5 nm	3 nm	0.3 nm	0.3 nm	0.3 nm
Approx. sensitivity	0.5%	1%	1%	3%	0.01 ppm	0.01 ppm	0.01%	0.01%
Typical information depth	10 nm	10 nm	10 nm	10 nm	3 nm	3 nm	0.5 nm	0.5 nm
Elements not analyzed	H, He	H, He	H, He	H, He				
Information								
Elemental	√	√	√	√	√	√	√	√
Isotopic					√	√	√	√
Chemical		√	√	√			√	√
Molecular			√				√	√
Material								
Metal	√	√	√	√	√	√	√	√
Semiconductor	√	√	√	√	√	√	√	√
Insulator or ceramic			√	√	√	√	√	√
Polymer, organic or bio			√	√			√	√

depend sensitively on the matrix, and so quantification is difficult for concentration levels above 1%, but in the more dilute regime the intensity is proportional to the composition. SIMS has thus found a dominant role here. The use of a mass spectrometer in SIMS allows isotopes to be separated, and this leads to a useful range of very precise diffusion studies with isotopic markers. The above considerations for SIMS cover the technique that is often called dynamic SIMS (d-SIMS). Another form of SIMS, static SIMS (SSIMS), is used to study the outermost surface, and here detailed information is available to analyze complex molecules that is not available in XPS. This is less routine but has significant promise for the future.

Figure 6.1 [6.1] shows a diagram of the spatial resolution and information content of these and other techniques, which helps to place the more popularly used methods in context. Additional information is given in Table 6.1. These analytical techniques have all been in use in both industry and the academic sector since the end of the 1960s, but it is only more recently that fast throughput, highly reliable instruments have become available and also that good infrastructures have been developed to support analysts generally. Documentary standards for conducting analysis were started early by ASTM [6.2]. In 1993, international activity started in the ISO in technical committee TC201 on surface chemical analysis. Details may be found at the website given in reference [6.3] or on the National Physical Laboratory (NPL) website [6.4], following the route *International Standardisation and Traceability*. Table 6.2 shows the titles of ISO standards published to date, and Table 6.3 the standards currently in draft. One-page articles on most of the published standards are given in the journal *Surface and Interface Analysis*. The relevant references are listed in the final column in Table 6.2.

Whilst consistent working depends on documentary standards, much quantitative measurement depends on accurate data and traceable measurement standards. This requires reference data, reference procedures, and certified reference materials. Some of these are available at the NPL website [6.4], some on the website of the US National Institute of Standards and Technology (NIST) [6.5], and reference materials may be found from several of the national metrology institutes and independent suppliers. Further assistance can be found in essential textbooks [6.6–8] or online at usergroups [6.9]. We shall cite these as appropriate in the text below. Of particular importance is ISO 18115 and the amendments in which ≈ 800 terms used in surface analysis and scanning probe microscopy are defined. Relevant terms are used and defined here, consistent with that international standard. We first consider issues for measurement by AES and XPS and then for dynamic and static SIMS.

Table 6.2 Published ISO Standards from ISO TC201

No.	ISO standard	Title (SCA = surface chemical analysis)	Title and author
1	14237	SCA – Secondary ion mass spectrometry – Determination of boron atomic concentration in silicon using uniformly doped materials	[6.10]
2	14606	SCA – Sputter depth profiling – Optimization using layered systems as reference materials	[6.11]
3	14975	SCA – Information formats	[6.12]
4	14976	SCA – Data transfer format	[6.13]
5	15470	SCA – X-ray photoelectron spectroscopy – Description of selected instrumental performance parameters	
6	15471	SCA – Auger electron spectroscopy – Description of selected instrumental performance parameters	
7	15472	SCA – X-ray photoelectron spectrometers – Calibration of energy scales	[6.14]
8	TR 15969	SCA – Depth profiling – Measurement of sputtered depth	[6.15]
9	TR 16268	SCA – Proposed procedure for certifying the retained areic dose in a working reference material produced by ion implantation	
10	17560	SCA – Secondary ion mass spectrometry – Method for depth profiling of boron in silicon	[6.16]
11	17973	SCA – Medium-resolution Auger electron spectrometers – Calibration of energy scales for elemental analysis	[6.17]
12	17974	SCA – High-resolution Auger electron spectrometers – Calibration of energy scales for elemental and chemical-state analysis	[6.18]
13	18114	SCA – Secondary ion mass spectrometry – Determination of relative sensitivity factors from ion-implanted reference materials	[6.19]
14	18115	SCA – Vocabulary	[6.20]
15	18115Amd1	SCA – Vocabulary	[6.21]
16	18115Amd2	SCA – Vocabulary	[6.22]
17	18116	SCA – Guidelines for preparation and mounting of specimens for analysis	
18	18117	SCA – Handling of specimens prior to analysis	
19	18118	SCA – Auger electron spectroscopy and x-ray photoelectron spectroscopy – Guide to the use of experimentally determined relative sensitivity factors for the quantitative analysis of homogeneous materials	[6.23]
20	TR 18392	SCA – X-ray photoelectron spectroscopy – Procedures for determining backgrounds	[6.24]
21	18394	SCA – Auger electron spectroscopy – Derivation of chemical information	[6.25]
22	18516	SCA – Auger electron spectroscopy and x-ray photoelectron spectroscopy – Determination of lateral resolution	[6.26]
23	19318	SCA – X-ray photoelectron spectroscopy – Reporting of methods used for charge control and charge correction	[6.27]
24	TR 19319	SCA – Auger electron spectroscopy and x-ray photoelectron spectroscopy – Determination of lateral resolution, analysis area, and sample area viewed by the analyzer	[6.28]
25	20341	SCA – Secondary ion mass spectrometry – Method for estimating depth resolution parameters with multiple delta-layer reference materials	[6.29]
26	20903	SCA – Auger electron spectroscopy and x-ray photoelectron spectroscopy – Methods used to determine peak intensities and information required when reporting results	[6.30]
27	21270	SCA – X-ray photoelectron and Auger electron spectrometers – Linearity of intensity scale	[6.31]
28	22048	SCA – Information format for static secondary ion mass spectrometry	[6.32]
29	TR 22335	SCA – Depth profiling – Measurement of sputtering rate: mesh-replica method using a mechanical stylus profilometer	
30	23812	SCA – Secondary ion mass spectrometry – Method for depth calibration for silicon using multiple delta-layer reference materials	
31	23830	SCA – Secondary ion mass spectrometry – Repeatability and constancy of the relative-intensity scale in static secondary ion mass spectrometry	
32	24236	SCA – Auger electron spectroscopy – Repeatability and constancy of intensity scale	[6.33]
33	24237	SCA – X-ray photoelectron spectroscopy – Repeatability and constancy of intensity scale	[6.34]
34	29081	SCA – Auger electron spectroscopy – Reporting of methods used for charge control and charge correction	

Table 6.3 ISO standards from ISO TC201 for AES, SIMS, and XPS in draft

No.	ISO std.	Title[a]
1	10810	SCA – X-ray photoelectron spectroscopy – Guidelines for analysis
2	12406	SCA – Secondary ion mass spectrometry – Method for depth profiling of arsenic in silicon
3	13084	SCA – Secondary ion mass spectrometry – Calibration of the mass scale for a time-of-flight secondary ion mass spectrometer
4	13424	SCA – X-ray photoelectron spectroscopy – Reporting of results for thin-film analysis
5	TR 14187	SCA – Characterization of nanostructured materials
6	14237	SCA – Secondary ion mass spectrometry – Determination of boron atomic concentration in silicon using uniformly doped materials
7	14701	SCA – X-ray photoelectron spectroscopy – Measurement of silicon oxide thickness
8	16242	SCA – Recording and reporting data in Auger electron spectroscopy (AES)
9	16243	SCA – Recording and reporting data in x-ray photoelectron spectroscopy (XPS)
10	18115-1	SCA – Vocabulary – Part 1: General terms and terms used in spectroscopy
11	18115-2	SCA – Vocabulary – Part 2: Terms used in scanning probe microscopy
12	TR 19319	SCA – Determination of lateral resolution in beam-based methods

[a] ISO titles spell out the acronyms in full but are abbreviated here for reasons of space:
AES = Auger electron spectroscopy or spectrometer(s)
SCA = Surface chemical analysis
SIMS = Secondary ion mass spectrometry or spectrometer(s)
TR = Technical report
XPS = X-ray photoelectron spectroscopy or spectrometer(s)

6.1.1 Auger Electron Spectroscopy (AES)

General Introduction

In AES, atoms in the surface layers are excited using an electron beam of typically 5 or 10 keV energy, but generally in the range 2–20 keV. In modern instruments this will typically be of 5–50 nA beam current, giving a spatial resolution in the range 20 nm–2 μm and, in carefully designed instruments, below 5 nm. The surface atoms lose an electron from an inner shell and the atoms then de-excite either by an Auger transition – emitting an Auger electron – or by filling with an outer shell electron and emitting an x-ray that would be detected in the complementary technique of electron probe microanalysis (EPMA). In the Auger process, an electron from a higher level E_2 fills the vacant inner shell level E_1, and the quantum of energy liberated is removed by a third electron from a level E_3 that is emitted with a characteristic energy E_A, defined approximately by

$$E_A = E_2 + E_3 - E_1 \,. \tag{6.1}$$

In (6.1), the energies of the bound levels E_1, E_2, and E_3 are taken to be negative quantities. This is shown in Fig. 6.2a. Relaxation effects add small additional energy terms of the order of 5–10 eV, but (6.1) allows us to identify the characteristic peaks in the emitted electron energy spectrum and hence all the elements present except H and He. Core levels deeper than about 2.5 keV have weak ionization cross sections, and so Auger electrons with emitted energies greater than 2.5 keV are weak and are rarely analyzed. Additionally, Auger electrons with energies below 50 eV are superimposed on the large secondary-electron emission background. Thus, the peaks used for analysis generally lie in the kinetic energy range 50–2500 eV, and this conveniently covers all of the elements except H and He.

The reason why AES is both surface specific and surface sensitive lies in the range of the Auger electrons be-

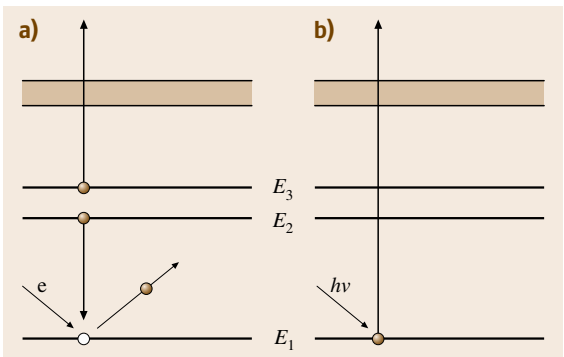

Fig. 6.2a,b Energy level diagram showing emission processes: **(a)** Auger electrons, **(b)** photoelectrons. The *shaded region* shows the conduction or valence bands to which the energy levels are referenced

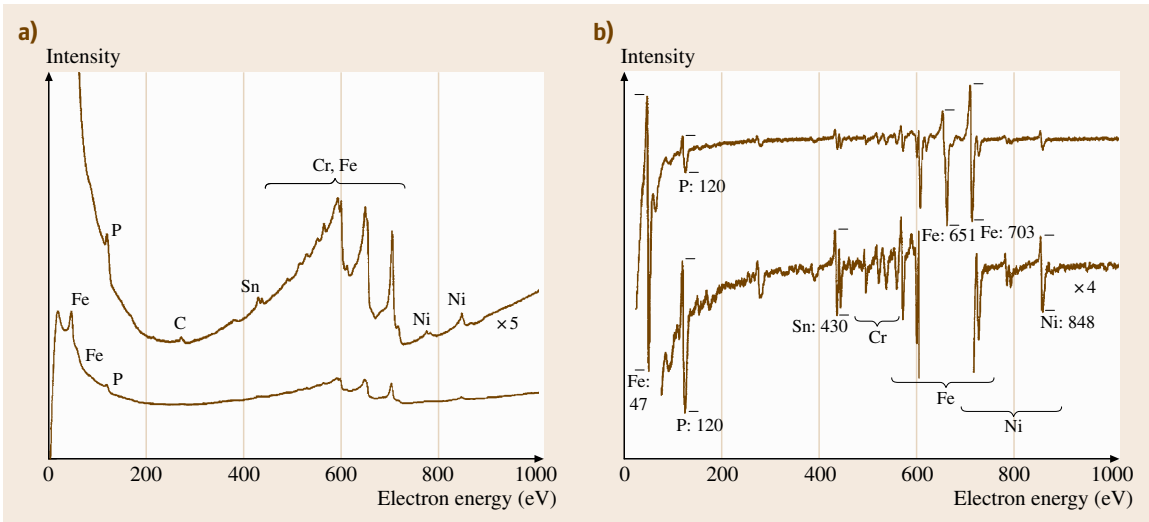

Fig. 6.3a,b Auger electron spectra from the grain boundary fracture surface of a low alloy steel with 0.056 wt % added phosphorus after a temper brittling heat treatment and analyzed using a cylindrical mirror analyzer: **(a)** direct mode presentation, with the *lower curve* magnified five times, and **(b)** differential mode presentation, with the *lower curve* magnified four times (after *Hunt* and *Seah* [6.36]). The fracture is made, in situ, usually by impact, in ultrahigh vacuum to stop the oxidation that would otherwise occur upon air exposure. Oxidation would remove the interesting elements from the spectra

fore inelastic scattering causes them to be lost from the peak and merged with the background. In early work, this electron attenuation length L is given by [6.35]

$$L = \frac{538}{E_A^2} + 0.41\,(aE_A)^{0.5} \text{ monolayers}\,, \qquad (6.2)$$

where a^3 is the atomic volume in nm^3. A typical value of a is 0.25 nm, so that L ranges from one monolayer at low energies to ten monolayers at high energies.

Figure 6.3 shows a typical Auger electron spectrum from studies to characterize material used to aid quantification when analyzing the grain boundary segregation of phosphorus in steel. To obtain this spectrum, the material is fractured, in situ, in the spectrometer, to present the grain boundary surface for analysis. The peaks are labeled for both the direct mode and the differential mode of analysis. Historically, spectra were only presented in the differential mode so that low-energy peaks such as those of P and minor constituents such as Cr, which occur on steeply sloping backgrounds, could be reliably measured. Simple methods of valid background subtraction are not generally available, so even though spectra may be recorded today in the direct mode, they are often subsequently differentiated using a mathematical routine with a function of 2–5 eV width [6.37, 38].

The shapes of the spectra and the positions of the peaks may be found in relevant handbooks [6.39–43]. The transitions in AES are usually written using x-ray nomenclature so that, if the levels 1, 2, and 3 in (6.1) are the $2p_{3/2}$, $3p_{3/2}$, and $3d_{5/2}$ subshells, the transition would be written $L_3M_3M_5$ and, for the metals Ca to Cu, since M_5 is in the valence band, this is often written L_3M_3V. Auger electron peaks involving the valence band are usually broader than those only involving core levels, and those involving two electrons in the valence band can be broader still. The precise energies and shapes of the peaks change with the chemical state. The transitions involving the valence band are the ones most affected by the chemical state and can show peak splitting and shifts of up to 6 eV upon oxidation [6.44]. The three large Fe peaks in Fig. 6.3 are LCC, LCV, and LVV at 600, 651, and 700 eV, respectively, where C represents a core level. The LVV transition is the most strongly affected by oxidation in the series from Ti to Cu, with the effect strongest at Cr [6.44].

For quantitative analysis, many users apply a simple equation of the form

$$X_A = \frac{I_A/I_A^\infty}{\sum_i I_i/I_i^\infty}\,, \qquad (6.3)$$

where X_A is the atomic fraction of A, assumed to be homogeneous over the 20 or so atom layers of the

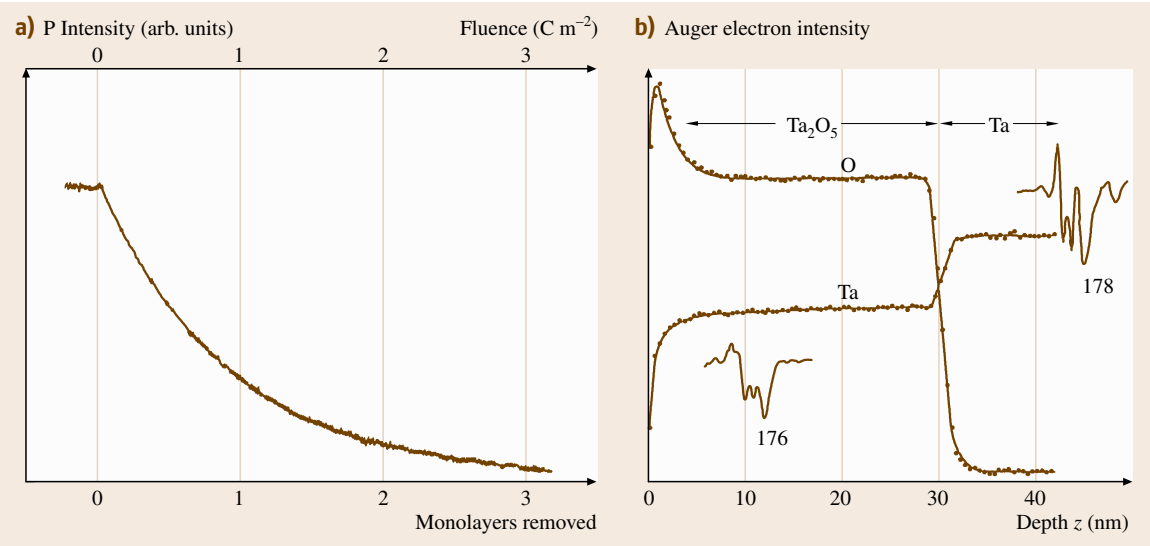

Fig. 6.4a,b Sputter depth profiles for differential signals in AES using argon ions: **(a)** P signal at 120 eV from the low alloy steel in Fig. 6.3b using 3 keV ions (after [6.36]), **(b)** O and Ta signals from a 28.4 nm-thick Ta_2O_5 layer using 2 keV ions (after *Seah* and *Hunt* [6.45]). The steel sample is profiled after fracture, in situ, and so is not air exposed, whereas the Ta_2O_5 layer had been prepared 6 months earlier and kept in laboratory air

analysis. In (6.3), the I_i^{∞} are pure element relative sensitivity factors taken from handbooks [6.39–43]. This gives an approximate result but suffers from three major deficiencies that may be resolved reasonably easily. We shall return to this later but will continue, for the present, to deal with the general usages of AES.

Two major uses that developed early concerned imaging and composition depth profiling using inert gas ion sputtering. Generally, in imaging, most analysts were content to use the peak intensity from the direct spectrum and then to remove an extrapolated background so that the brightness of each point in the image was proportional to the peak height. This is quick and easy in modern multidetector systems. Earlier systems used the signal at the negative peak of the analog differential spectrum. These approaches are simple and practical and can rapidly define points for subsequent analysis, but interpretation of the contrast for samples with significant surface topography or for thin layers with underlying materials with different atomic numbers can be very complex.

Generally, in composition depth profiling, argon ions in the energy range 1–5 keV are used with current density of 1–30 $\mu A/cm^2$. Profiles could either be for monolayers, as exemplified in Fig. 6.4a by the profile for the segregated phosphorus shown in Fig. 6.3b, or for thicker layers, as exemplified in Fig. 6.4b for the tantalum pentoxide certified reference material (CRM) BCR 261 [6.45–48]. The quantification of the depth and the depth resolution are the critical factors here, and these we shall discuss *Sputter Depth Profiling*.

Handling of Samples

In many applications of AES, the samples are prepared in situ in the ultrahigh vacuum of the instrument, and the user will be following a detailed protocol evaluated already in their laboratory or in the published literature. However, where samples have been provided from elsewhere or where the item of interest is the overlayer that is going to be depth-profiled, the samples will usually arrive with surface contamination. This contamination is usually from hydrocarbons, and it attenuates all of the signals to be measured. It is useful to remove these hydrocarbons unless they are the subject of analysis, and for most materials, high-performance liquid chromatography (HPLC)-grade isopropyl alcohol (IPA) is a very effective [6.49] contamination solvent unless dealing with polymers or other materials soluble in IPA. This makes analysis of the surface both clearer and more accurate and, for sputter depth profiling, removes much of the low sputter yield material that may cause loss of depth resolution in the subsequent profile. Samples can then either be stored in

Table 6.4 Kinetic energies, $E_{\mathrm{ref}\,n}$, for reference to the vacuum level. Values in parenthesis are referenced to the Fermi level

Peak number n	Assignment	Kinetic energy, $E_{\mathrm{ref}\ n}$ (eV)	
		Direct spectra	Differential spectra
1	Cu $M_{2,3}VV$	58 (62)	60 (64)
2	Cu L_3VV	914 (919)	915** (920**)
3	Al $KL_{2,3}L_{2,3}$	1388 (1393)	1390** (1395**)
4	Au $M_5N_{6,7}N_{6,7}$	2011* (2016*)	2021 (2026)

* For beam energies below 6 keV and for $0.25\% < R \leq 0.5\%$ add 1 eV
** For $0.27\% < R \leq 0.5\%$ add 1 eV
This table is derived from work in [6.50–52]

clean glass containers [6.49] until needed or analyzed directly.

Details on how samples should be collected and supplied to the analyst are given in ISO 18117 and for mounting them for analysis in ISO 18116, listed in Table 6.2. The guiding principle for mounting the sample is to reduce the presence of any material that causes gases in the vacuum system, contamination of the surface to be analyzed or local charging of insulating material.

We are now ready for analysis and need to consider the spectrometer.

Calibrating the Spectrometer Energy Scale

Depending on the type of spectrometer and its intended use, there are two ISO standards that provide procedures for calibrating the spectrometer energy scale. ISO 17973 is for medium-resolution systems designed for elemental analysis and is suitable for instruments with a relative resolution R of $\leq 0.5\%$, used in either the direct mode or the differential mode with a peak-to-peak differentiation of 2 eV. ISO 17974 is for high-resolution spectrometers intended for both elemental and chemical state analysis. With both standards, high-purity metal foils of the appropriate elements are used with their surfaces cleaned by a light ion sputtering. The exact peak energies are defined by a simple, accurate protocol [6.54], and those are then compared with tabulated values obtained from traceable measurements.

For medium-resolution spectrometers, the peak energies are given in Table 6.4, and for most spectrometers, only Cu and Au foils are required. Note that values are given referenced to both the vacuum level and, in brackets, the Fermi level. In principle, energies can only be accurately referenced to the Fermi level, since the vacuum level – the level in the vacuum of the spectrometer at which a stationary electron exists – varies from point to point in the spectrometer. This will change after bake-out, and depends on local surface work functions. This level generally exists at 4–5 eV above the Fermi level, and for convenience, a value of 4.5 eV is used in these ISO standards and elsewhere. The vacuum level is used here, since all early work and the handbooks [6.39–43] use the vacuum level reference.

A few spectrometers do not measure kinetic energies above 2 keV, and for these, an alternative energy peak is provided in Table 6.4 using Al.

For high-resolution spectrometers, the vacuum level is too vague, and data are Fermi level referenced. High-resolution spectrometers are often also used for XPS, where only Fermi level referencing is used, and this enhances consistency. For high-resolution spectrometers, Cu and Au are again used, except in the exceptional circumstances where the spectrometer scale is limited to 2 keV, in which case Au must again be replaced by Al, as shown in Table 6.5.

To obtain the necessary level of accuracy, either where the resolution R is poorer than 0.07% and when Au is used, or where R is poorer than 0.04% and when Al is used, a correction is required to the tabulated values such that the peaks are located at $E_{\mathrm{ref}\,n}$, where

$$E_{\mathrm{ref}\,n} = E^{\mathrm{o}}_{\mathrm{ref}\,n} + cR + dR^2 \,. \tag{6.4}$$

Table 6.5 Reference values for the peak positions on the kinetic energy scale [6.52] $E^{\mathrm{o}}_{\mathrm{ref}\,n}$ for $R < 0.04\%$ if Al is used, or $R < 0.07\%$ if Au is used

Peak number n	Assignment	$E^{\mathrm{o}}_{\mathrm{ref}\,n}$ (eV)
1	Cu $M_{2,3}VV$	62.37
2	Cu L_3VV	918.69
3	Al $KL_{2,3}L_{2,3}$	1393.09
4	Au $M_5N_{6,7}N_{6,7}$	2015.80

These kinetic energies are referenced to the Fermi level.
This table is a refinement of earlier tables (after [6.50,51,53])

Table 6.6 Corrections to the reference kinetic energies for resolutions poorer than 0.07% when Au is used, or poorer than 0.04% when Al is used

Peak number n	Assignment		c (eV)	d (eV)
1	Cu $M_{2,3}VV$		0.0	0.0
2	Cu L_3VV		0.2	−2.0
3	Al $KL_{2,3}L_{2,3}$		−0.3	−1.8
4	Au $M_5N_{6,7}N_{6,7}$:	5 keV $n(E)$	0.0	0.0
		5 keV $En(E)$	−0.3	4.4
		10 keV $n(E)$	−0.2	0.0
		10 keV $En(E)$	−0.1	0.0

This table is a simplification of a more complex table (after [6.51]) and is consistent with the more complex table for relative resolutions in the range $0\% < R < 0.2\%$ to within 0.015 eV

The values of the coefficients c and d are given in Table 6.6, where the resolution R, given by $\Delta E/E$, is expressed in percent.

In these ISO standards, detail is provided of the signal levels to use, the contributions leading to uncertainties in the final calibration, and methods to ensure, as far as is reasonable, that the instruments are kept in calibration within their stated tolerance limits in order to be fit for purpose.

Repeatability of the Intensity Scale

All electron spectrometers use electron multiplier detectors, and these, unfortunately, age with use. Thus, even though the analyst may use consistent spectrometer settings each time, the absolute intensity of the measured spectrum will slowly reduce. This reduction may be offset by increasing the detector multiplier voltage. However, then the user may observe that the relative intensities of peaks in the spectrum have changed, and if we quantify a spectrum via equations such as (6.3), the calculated value of X – the measured composition – will appear to have changed. These effects mean that the analyst needs to understand the behavior of the multiplier detector [6.55] in order to maintain long-term repeatability of measurements. Indeed, a failure to understand detector behavior can lead to gross spectral distortion [6.56].

With many pulse-counting systems, the electron multiplier is designed to give a sufficiently large output pulse that the detection electronics receives that pulse well separated in magnitude from the ambient noise in the system. However, the pulses from the multiplier have a distribution of intensities, and so it is necessary to increase the multiplier gain until all of the pulses are clearly separated from the background noise. The gain is set by the multiplier voltage, and the separation point is defined by a discriminator in the detector electronics. As the multiplier voltage is increased from a low level, at a voltage usually in the range 1800–2400 V, the count rate suddenly starts to rise, reaching 90% of its maximum over a range of about 250 V. The count rate then rises more slowly to a saturation maximum value [6.57]. The transition from zero to the maximum count rate occurs rapidly except at high count rates [6.57]. At high count rates, the pulse height distribution broadens and the transition occupies a wider voltage range. NPL has adopted a procedure, for single-channel electron multipliers, of setting the multiplier voltage at 500 V more positive than the voltage required to observe 50% of the saturation count rate when set to measure around 100 kc/s. These values are not critical but do lead to precise setting of the multiplier voltage. This gives a reliable result and allows the user to track the multiplier behavior as it ages in order to replace the multiplier at a convenient time. If a significantly lower multiplier voltage than this setting is used, the count rates are lowered and the system becomes very nonlinear. If higher multiplier voltages are used, the linear counting range extends to higher counting rates but this occurs at the expense of the multiplier life [6.58].

In their normal use, all counting systems suffer some loss of counts at high counting rates arising from the counting electronics' dead time. Information on dead time may be found in references [6.57, 58] as well as ISO 21270. ISO 21270 also deals with the diagnoses of the gross nonlinearities that have been seen in the intensity scales of certain designs of detector [6.59, 60].

If the detector is correctly set, it is important to establish the constancy and repeatability of the instrument's intensity response. For AES, the ratio of the intensity of the Cu L_3VV peak to that of the $M_{2,3}VV$ peak is a useful measure, particularly using the peak-to-peak differential heights. Providing that sufficient intensities are acquired to be statistically meaningful,

seven repeat measures of one peak followed by seven of the other allows the trend in the ratio during acquisition to be evaluated as well as the intensity ratio repeatability standard deviation. With around 2 M counts per channel at the peaks, ISO 24236 shows how repeatability standard deviation of better than 0.5% may be attained if the data are recorded at 0.1 eV energy intervals and specific *Savitzky* and *Golay* smoothing [6.37] is used. Any drift in the absolute intensities or of the ratio between measurements may indicate a source, analyzer or detector instability that then needs to be investigated.

Calibrating the Intensity Scale

Interlaboratory studies to compare the shapes of spectra obtained in different laboratories unfortunately show that there are marked differences [6.61] that can lead to variations of a factor of two in quantification if the same relative sensitivity factors are to be used in all laboratories. These differences exist between similar models of spectrometer from the same manufacturer and arise mainly from the age dependence of the detector efficiency $D(E)$. $D(E)$ exhibits a curve that rises with the detected electron kinetic energy E from zero at $E = 0$ to a maximum in the energy range 200–600 eV and then to a slow decline at higher energies. In addition to the detector efficiency, there are electron optical terms to describe the spectrometer transmission function $T(E)$. These need to be combined to give the total instrumental response.

Formally, one may write the intensity–energy response function (IERF) as

$$\text{IERF} = T(E)\,D(E)\,, \tag{6.5}$$

with additional terms, omitted here, that may arise from stray electron or magnetic fields [6.62]. The term $T(E)$ is usually approximately proportional to E for spectrometers operated in the constant $\Delta E/E$ mode, and proportional to E^{-n}, where n ranges from 0 to 1, as the energy increases in the constant ΔE mode. In the constant $\Delta E/E$ mode, all voltages on electron optical elements of the spectrometer are scanned so that they remain in fixed proportion to each other. The resolution then deteriorates as the energy increases. This is the mode generally used for AES, unless high-resolution spectra are required, since very simple spectrometers may then be used with high efficiency and with high intensities at the high energies where the peaks are weak. On the other hand, the constant ΔE mode is used for high-resolution analysis so that ΔE, the spectrometer energy resolution, is maintained at, say, 0.25 eV at all energies. This is usually achieved by setting the pass element of the spectrometer to detect, say, 25 eV electrons, and then scanning this through the spectrum. If we know the IERF, the true spectrum that we need, $n(E)$, is given by

$$n(E) = \frac{I(E)}{\text{IERF}}\,, \tag{6.6}$$

where $I(E)$ is the measured spectrum.

In order to calibrate spectrometers for their absolute or relative IERFs, a series of studies were made using different configurations of an instrumented spectrometer with a Faraday cup detector to measure absolute reference spectra [6.61–64]. These spectra were measured for Cu, Ag, and Au polycrystalline foil samples using a 5 keV electron beam at 30° to the surface normal. Using these spectra, the absolute IERF may be determined for any spectrometer. To facilitate this, a software system has been designed for users to self-calibrate their instruments based on their own measurements for these foils [6.65]. The reason for using three foils when, in principle, one would suffice, is to evaluate the scatter between the three independent IERF derivations in order to calculate the repeatability of the average IERF derivation. These derivations can be consistent to $< 1\%$. In the calibration, certain other diagnostics are important. For instance, internal scattering [6.66] may occur in some spectrometers, and if this has any significant intensity, it leads to uncertainty in the derived IERF. The above-mentioned software diagnoses the extent of the internal scattering using the rules established in [6.66] with the Cu and Ag samples.

The true spectral shape obtained in this way will not change significantly with time provided the IERF is determined at appropriate time intervals. Being absolute, use may then be made of an extremely large volume of theoretical knowledge as well as background removal procedures based on physically meaningful algorithms [6.67,68] in order to interpret different aspects of the spectra.

As noted earlier, many analysts do not use any significant theoretical evaluation of the spectra and simply use the peak-to-peak differential intensity. Relative sensitivity factors for (6.1) are available from several handbooks [6.39–43], but analysis shows that the lack of control of the IERF leads to significant variability. Additionally, different choices of modulation energy for the differentiation increase that variability from source to source [6.69], so that half of the published sensitivity factors for each element differ from the average by more than a factor of 1.5. These issues are addressed below.

Quantitative Analysis of Locally Homogeneous Solids

It is useful to consider the basic derivation of sensitivity factors so that the user appreciates why things are done in certain ways and can link this text with older texts.

The Auger electron intensity per unit beam current into a small solid angle $d\Omega$ for a sample of pure element A involving the XYZ transition I_{AXYZ} may be calculated from the relation for homogeneous systems [6.70].

$$I^{\infty}_{AXYZ} = \gamma_{AXYZ} n_{AX} \sigma_{AX}(E_0) \sec\alpha \times [1 + r_A(E_{AX}, E_0, \alpha)] N_A Q_A(E_{AXYZ}) \times \lambda_A(E_{AXYZ}) \cos\theta \left(\frac{d\Omega}{4\pi}\right) , \quad (6.7)$$

where γ_{AXYZ} is the probability that the ionized core level X in element A is filled with the ejection of an XYZ Auger electron, $\sigma_{AX}(E_0)$ is the ionization cross section of the core level X in element A for electrons of energy E_0, n_{AX} is the population of the level X, α is the angle of incidence of the electron beam from the surface normal, $r_A(E_{AX}, E_0, \alpha)$ is the additional ionization of the core level X with binding energy E_{AX} arising from backscattered energetic electrons, $Q_A(E_{AXYZ})$ is a term discussed later in this section, N_A is the atomic density of the A atoms, $\lambda_A(E_{AXYZ})$ is the inelastic mean free path (IMFP) for the XYZ Auger electrons with energy E_{AXYZ} in sample A, and θ is the angle of emission of the detected electrons from the surface normal.

The inner shell ionization cross section is often calculated using *Gryzinski*'s formula [6.71], but a detailed analysis [6.72] shows that the formula of *Casnati* et al. [6.73] is significantly more accurate. Plots of these cross sections may be found in [6.72].

The parameter γ_{AX} allows for the competing process of x-ray emission, where

$$\gamma_{AX} = 1 - \frac{Z^4}{Z^4 + Z_0^4} , \quad (6.8)$$

with $Z_0 = 32.4$ [6.74] for X = K, 89.4 [6.74] for X = L, 155.9 [6.75] for X = M, and 300 for X = N shell [6.76].

The next term is the backscattering factor $r_A(E_{AX}, E_0, \alpha)$, and this is taken from the work of *Shimizu* [6.77]. General plots of this function may be found in [6.70]. Figure 4 in [6.78] shows the Z dependence of $[1 + r_A(E_{AX}, 5000, 30°)]$ for various E_{AX_i}, where the backscattering enhancement may reach over a factor of two. N_A values are evaluated from published data for elements [6.79, 80]. Figure 5 in [6.78] shows a plot of N_A versus Z. This is strongly periodic and spans a range of values with a factor of eight between the maximum and minimum values. The weak correction factor $Q_A(E_{AXYZ})$ is a term allowing for the reduction in overall escape probability of electrons from the solid arising from elastic scattering [6.81]. This parameter ranges from 0.9 to 1.0 and depends on the element and the electron energy. Values of Q may be taken from the plots of *Seah* and *Gilmore* [6.82]. The inelastic mean free path, $\lambda_A(E)$, can be taken from the TPP-2M formula [6.83] given by

$$\lambda_A(E) = \frac{E}{E_p^2 \left[\beta \ln(\gamma E) - (C/E) + \left(D/E^2\right)\right]} \quad [\text{Å}] , \quad (6.9)$$

where

$$E_p = 28.8 \left(\frac{\rho N_v}{A}\right)^{0.5} \quad [\text{eV}] , \quad (6.10)$$

$$\beta = -0.10 + 0.944 \left(E_p^2 + E_g^2\right)^{-0.5} + 0.069 \rho^{0.1} , \quad (6.11)$$

$$\gamma = 0.191 \rho^{-0.50} , \quad (6.12)$$

$$C = 1.97 - 0.91 W , \quad (6.13)$$

$$D = 53.4 - 20.8 W , \quad (6.14)$$

$$W = \frac{\rho N_v}{A} . \quad (6.15)$$

In these equations, ρ is the density (in g cm^{-3}), N_v is the number of valence electrons per atom, and A is the atomic weight. For metals, the value of E_g, the band gap, is zero. Recommended values for N_v have recently been published by *Tanuma* et al. [6.84]. Free software is available to facilitate this process [6.5, 85].

The above formulae allow us to calculate the intensity for a pure element, and I^{∞}_A (for simplicity, we now omit to define the particular transition XYZ) may be considered as a pure element relative sensitivity factor (PERSF). These are what one would obtain by measuring spectra in the reference handbooks [6.39–43], after correcting for the IERF. To compute the composition, one then needs to use not (6.2), but [6.70]

$$X_A = \frac{F_{AM}\left(I_{AM}/I^{\infty}_A\right)}{\sum_i F_{iM} I_{iM}/I^{\infty}_i} , \quad (6.16)$$

where the I_{iM} are the intensities for the elements i measured in the matrix M of the sample. The matrix elements F_{iM} are given by [6.70]

$$F_{iM} = \frac{N_i}{N_M} \frac{Q_i(E_i)}{Q_M(E_i)} \frac{[1 + r_i(E_i)]}{[1 + r_M(E_i)]} \frac{\lambda_i(E_i)}{\lambda_M(E_i)} . \quad (6.17)$$

The difficulty of calculating the F_{iM} when the matrix is not known until the X_A are calculated leads most analysts to ignore the F_{iM} and effectively replace them by unity. The F_{iM} vary from 0.1 to 7 in different systems [6.78], and so this is the error involved by ignoring them.

Seah and *Gilmore* [6.78] show that (6.2) is in fact valid if the PERSF, I_A^{∞}, is replaced by the average matrix relative sensitivity factor (AMRSF) I_A^{Av}, given by

$$I_A^{Av} = \gamma_A n_A \sigma_A \sec\alpha [1 + r_{Av}(E_A)] N_{Av} Q_{Av}(E_A) \times \lambda_{Av}(E_A) \cos\theta \left(\frac{d\Omega}{4\pi}\right) . \quad (6.18)$$

In this equation, the items concerning effects inside the atom retain their original element A specificity and subscript ("A"), but those outside, such as the number density, become that for an average matrix ("Av"). Appropriate equations for the average matrix terms are given in references [6.78, 86] and may also be found in ISO 18118.

Many of the above numbers are difficult to calculate, and so experimental databases are often used. However, we may now see why lack of calibration of the spectrometers and use of the wrong measures can lead to significant errors. Tables of data for AMRSFs and their constituent parts are available on the NPL website [6.4] for the convenience of analysts.

Quantification of Inhomogeneous Samples

The general quantification of inhomogeneous layers that vary over the outermost 8 nm is a complex issue dealt with in detail elsewhere [6.87, 88]. However, for AES there is a special case of particular interest to metallurgists and those studying catalysts: the case of the segregated layer one atom thick with partial coverage. Expressed as a fraction of a monolayer at the packing density of the substrate s, the fraction of the monolayer is given by θ_A, where [6.70]

$$\theta_A = X_A \frac{L_s(E_A)}{a_s} \cos\theta , \quad (6.19)$$

where a_s^3 is the atomic volume of the substrate atoms and $L_s(E_A)$ is the attenuation length of electrons of energy E_A in the overlayer. $L_s(E_A)$ is related to $\lambda_s(E_A)$ [6.82], as discussed later at (6.21). In (6.19), θ_A is unity at a_s^{-2} atoms per unit area. Much early and some recent AES work in this area ignores the difference in concept between θ_A and X_A, leading to confusion and errors in the range 1–10.

Sputter Depth Profiling

The basic principle of sputter depth profiling is that one removes the surface layer by layer using inert gas ion sputtering, in situ, usually with 1–5 keV argon ions, whilst monitoring the remaining surface by AES. For samples with air-exposed surfaces there will be a level of hydrocarbon contamination that is first removed, and during this short period, the signals from the underlying material rise rapidly, as seen in Fig. 6.4b. This effect is not seen in Fig. 6.4a, as the surface there is not air exposed. For elemental solids, the signal then remains constant until the layer is removed. The signal then falls to an appropriate level or zero for the next layer. If the layer is a compound, one element may be preferentially sputtered so that the quantified signal no longer reflects the composition prior to sputtering. For the Ta_2O_5 layer in Fig. 6.4b, we see the composition fall from Ta_2O_5 to approximately TaO as the oxygen is depleted. The compound is not stoichiometric TaO but a distribution of chemical states [6.89–91] over a thin layer of the order of the projected range [6.92] of the sputtering ion. This range is typically slightly more than the analysis depth [6.93].

The preferential sputtering of compounds has been a long and rather frustrating area of research where theoretical models have been proposed [6.90, 94–97] but predicting the effect in any quantitative way is currently not possible. To quantify a profile involving a compound, the best approach is to sputter a reference layer of the compound under identical conditions to the sample in order to evaluate the spectral intensities expected. Generally, those who conduct such profiles are less interested in quantifying compound layers that they know are there, and are more interested in changes in the layers as a result of, say, a heat treatment that leads to changes in the interface shape. Thus there is already a built-in reference layer. To measure changes at the interfaces, good depth resolution is required.

In early studies of sputtered metallic layers, the depth resolution Δz deteriorated roughly according to

$$\Delta z = k z^{0.5} , \quad (6.20)$$

where for Δz and z in units of nm, k is approximately unity [6.90, 98]. This was caused by the development of topography, which can be measured by scanning electron microscopy (SEM; Sect. 6.2.4) or atomic force microscopy (AFM; Sect. 6.2.3). For single-crystal wafer studies, it was found that the depth resolution, which starts as an exponential decay of one monolayer (≈ 0.26 nm) for a submonolayer film, as

shown in Fig. 6.4a, degrades and saturates at approximately 1 nm [6.98, 99] for thicker films.

A major development was made by *Zalar* [6.101], who suggested rotating the sample whilst sputtering in the same manner as when preparing samples for transmission electron microscopy (TEM). With rotation speeds of about 1 rpm, excellent results of 5 nm resolution are obtained, even for the difficult polycrystalline metallic layers [6.102]. It is essential that the electron and ion beams are properly aligned to the same point on the sample surface, irrespective of the use of rotation or not, in order to obtain the best depth resolution [6.103].

In the above, we have used the term depth resolution without clearly defining it. In ISO 18115 it is defined as the depth range over which a signal changes by a specified quantity when reconstructing the profile of an ideally sharp interface between two media or a delta layer in one medium. In an attached note it adds that, for routine analytical use, a convention for the specified levels is 16–84% for layers such as those shown in Fig. 6.4b. These levels arise from the standard deviation points when the interface resolution is described by a Gaussian function. For very high-resolution profiles, the interface shape is described by exponentials [6.45, 102] and the above convention, although useful, then has no specific correlation with a physical model.

Above, we have considered Δz, but also critical is the measurement of the absolute depth z. Measurement of the sputtered depth is covered in the ISO technical report ISO/TR 15969. Usually, a stylus profilometer is used (Sect. 6.2.1), but certain laboratories prefer optical techniques (Sect. 6.2.2) or AFM (Sect. 6.2.3). AFM can be particularly useful for small, shallower craters where the roughness of the crater base is also of interest. There are several issues that analysts need to be aware of that are of increasing importance at shallower depths. At the start of sputtering, some contamination is removed. This takes a brief time. Next, the incident ions are implanted, causing a slight swelling. As the beam particles build up in the sample, the sputtering yield changes until, after sputtering for approximately 1 nm, an equilibrium is established. After this, the system remains constant if rotation is used; if not, a surface topography may develop that slowly reduces the sputtering rate. For sputtering with argon ions, the build-up of argon is typically 2.5% [6.104] and so these effects are small and are generally ignored. A further effect, seen for samples that react with air, is that the crater base will swell as it oxidizes on air exposure prior to the depth measurement. If a correlation of time and depth is made for many craters, a straight line correlation should be found, but it may not pass through the origin. Typically, the offset may be up to 1 nm for Si wafers.

Where a system comprises layers of different types, the sputtering rate will change from layer to layer, and an elapsed time to depth conversion cannot be made with one sputtering rate. Figure 6.5 shows the sputtering yield for argon incident at 45° for several energies and many elements. The rates for different elements clearly vary enormously. The rate then needs to be evaluated for

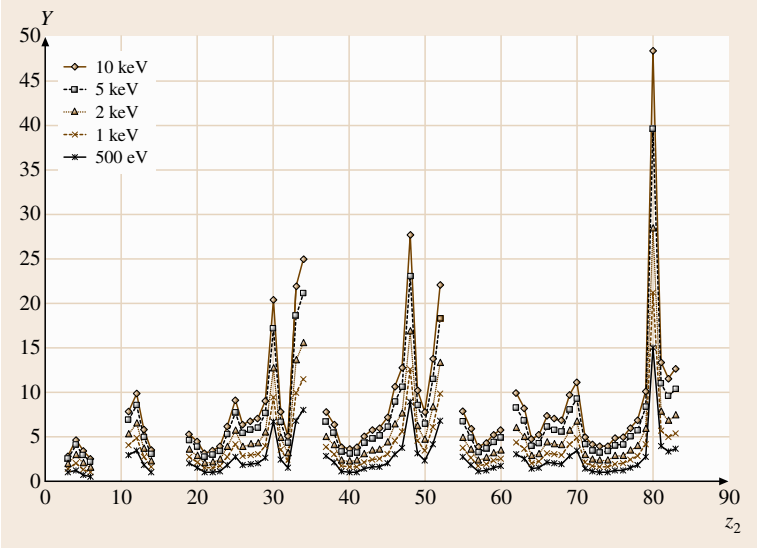

Fig. 6.5 Calculated sputtering yields of elements using argon ions at 45° to the sample surface for several energies as a function of the atomic number of the sample, Z_2 (after [6.3, 93, 100])

each layer separately or evaluated through calculation of the relevant sputtering yields Y and a measurement of the ion beam current density J at the AES measurement point

$$d = \frac{JtYa^3}{e} , \tag{6.21}$$

where t is the time for sputtering that layer, e is the electronic charge, and a^3 is the atomic volume deduced from

$$1000\rho N a^3 = A . \tag{6.22}$$

Ion beam currents generally need to be measured using a screened Faraday cup, but focused ion beam currents may be measured using an appropriately drilled hole in a sample or the sample stage [6.105]. In (6.22), ρ is the density of the element (kg/m^3) of atomic weight A, and N is Avogadro's number. Thus, d may be determined if Y is known. Values of Y have been tabulated for many elements and some compounds. Recent work has led to significant improvements in the accuracy of calculating Y for elements for Ne, Ar, and Xe bombarding ions at 0° and 45° angles of incidence [6.93, 104], with a typical uncertainty, for the calculations shown in Fig. 6.5, of 10%. The equations are rather complicated, and so plots of the yields may also be found as tables on the NPL website [6.100]. The uncertainty from this convenient route, however, means that it is not as accurate as a direct measurement of depth.

For sputter depth profiling, Ar is most popular. Occasionally, if the argon AES peaks interfere with the peaks to be measured, Ne or Xe may be used [6.104]. Some analysts prefer Xe, as the depth resolution is then improved sometimes.

6.1.2 X-ray Photoelectron Spectroscopy (XPS)

General Introduction

XPS has a considerable base in physics, in common with AES, and is often conducted using the same instrument. XPS uses characteristic x-rays to excite electrons that are energy-analyzed by the same spectrometer that is used for high-energy-resolution AES analysis. Thus, XPS instruments often have an added electron gun for AES. The x-ray source is generally of Mg or Al K_α x-rays or, in many modern instruments, monochromated Al K_α x-rays. As shown in Fig. 6.2b, the x-rays of energy $h\nu$ directly eject core electrons from the solid with kinetic energy E given by

$$E = h\nu - E_1 , \tag{6.23}$$

where it is these E_1 values, the core level binding energies, that are required in XPS. Thus, the E_1 values are usually taken to be positive values, unlike (6.1), and the binding energy scale is usually used directly rather than the Fermi level referenced kinetic energy E. The values of E_1 provide information about the chemical state of the element analyzed. Tabulated binding energies for the elements may be found in *Bearden* and *Burr* [6.106] and for elements and compounds in handbooks [6.107–109], textbooks [6.110], and websites [6.111]. Note that, whilst Bearden and Burr use the x-ray nomenclature for energy levels, as is common for AES, this is rarely used in XPS. Here, the level number and subshell letter with the spin–orbit coupling number are given, so that M_V or M_5 translates to $3d_{5/2}$. After the initial excitation, the atom is left with a core hole that can be filled by an Auger process ejecting an Auger electron. This electron also appears in the measured spectrum. Figure 6.6 shows a photoelectron spectrum for copper with the photoelectron and Auger electron peaks labeled.

The photoelectrons are mostly in the kinetic energy range 500–1500 eV, and so XPS is similar to AES in its surface sensitivity. For a few (often important) elements, the characteristic peaks may have kinetic energies as low as 200 eV.

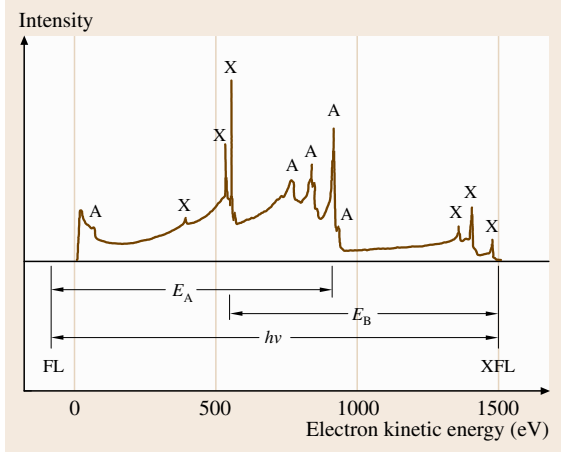

Fig. 6.6 X-ray photoelectron spectrum for Cu using an unmonochromated Al x-ray source. The photoelectron peaks are labeled "X" and the Auger electron peaks "A". The positions of the Cu Fermi level (FL) and the photoemitted Fermi level electrons (XFL) are indicated (after [6.53]). The vacuum level, indicated by the start of the spectrum, is 4.5 eV above the Fermi level (FL) and is shown exaggerated here for illustrative purposes

Handling of Samples

The handling of samples for XPS is generally the same as that for AES, except that the types of sample tend to be rather different. Environmental contaminants such as poly(dimethyl siloxane) (PDMS) and similar materials are often analyzed, and so it is rare for samples to be cleaned. More samples are insulating, and so greater consideration needs to be given to charge control and charge correction. Information on most of the important methods for these is given in ISO 19318, but what is achievable often depends on the specific instrumental setup. Samples can be in the form of polymer films or powders generally not studied by AES.

In some instruments, mounting the sample under a grid or aperture works well for charge control, but in others this leads to broader peaks. With monochromated x-rays, an electron flood gun or very low-energy ion flux may be required for charge control. Whatever is used, the analyst should ensure that the sample is not exposed to unnecessary levels of radiation, since most of these samples are easily degraded by heat, electrons or ions [6.115, 116].

Calibrating the Spectrometer Energy Scale

As for AES, Cu and Au samples set with their angle of emission $\leq 56°$ are sputtered clean, and the measured energies of the peaks listed in Table 6.7 are compared with the energy values given there. As for AES, the peak energy for the calibration is evaluated from the top of the peak without background subtraction [6.54]. In Table 6.7, peak number 3 is an Auger electron peak, and whilst this works well for unmonochromated x-rays, it cannot be used accurately with a monochromator. The lineshapes and energies of the K_{α_1} and K_{α_2} x-rays that characterize $h\nu$ in (6.23) appear to be the same in all unmonochromated instruments. However, the lineshapes and energies of the K_α x-rays, when monochromated, vary significantly and depend on the setup of the monochromator and its thermal stability. By altering the monochromator settings, the measured energies of the peak may be moved over a kinetic energy range of 0.4 eV without too much loss of intensity [6.113]. Thus, for monochromated systems, in Table 6.7 the Cu Auger electron peak is replaced by the $3d_{5/2}$ photoelectron peak from Ag. This action requires the cleaning of an additional sample.

In ISO 15472, the calibration given in Table 6.7 is included into a full protocol that includes methods of conducting the calibration, assessing the uncertainties, establishing tolerance limits, and evaluating a calibration schedule. For laboratories operating under a quality system [6.117], and for analysts trying to ensure the validity of their data, these are essential. Use of the standard with a modern, well-maintained spectrometer should result in calibration within tolerance limits of ± 0.2 eV over 4 months or ± 0.1 eV over 1 month before recalibration is required. For many purposes ± 0.2 eV is satisfactory.

Repeatability of the Intensity Scale

For XPS, the evaluation of the repeatability of the intensity scale is similar to that for AES in Sect. 6.1.1. Of critical importance are the comments made there in relation to detectors and especially ISO 21270 on the linearity of the intensity scale. For XPS, the intensity ratio is determined from cleaned copper using the Cu 3p and Cu $2p_{3/2}$ peak areas after subtracting a Shirley background [6.118]. Smoothing of the end-points for establishing the Shirley background can improve the precision and enable repeatabilities as good as 0.2% to be achieved in a series of measurements. ISO 24237 describes the signal levels and procedures needed to get the best quality data from a sample of copper, how to build that into a monitoring protocol, and how to set up tolerance limits for a control chart to try to ensure that the intensity measurements remain fit for purpose.

Calibrating the Intensity Scale

Interlaboratory studies to compare the shapes of spectra obtained in different laboratories unfortunately show

Table 6.7 Reference values for peak positions on the binding energy scale [6.113, 114] $E_{\mathrm{ref}\,n}$

Peak number n	Assignment	$E_{\mathrm{ref}\ n}$ (eV) Al K_α	Mg K_α	Monochromatic Al K_α
1	Au $4f_{7/2}$	83.95	83.95	83.96
2	Ag $3d_{5/2}$	–	–	368.21
3	Cu L_3VV	567.93	334.90	–
4	Cu $2p_{3/2}$	932.63	932.62	932.62

This table is a refinement of earlier tables (after [6.53, 112])

that there are marked differences [6.63]. These lead to variations of a factor of two in quantification if the same relative sensitivity factors were to be used in all laboratories.

The situation here and the rationale and protocol for evaluating and using the IERF are precisely the same as in *Calibrating the Intensity Scale* for AES, except that, instead of measuring the spectra from the Cu, Ag, and Au reference foils using 5 keV electrons, we use the Al or Mg x-rays at incident angles in the range 0−50° from the surface normal.

Relative sensitivity factors for (6.3) are available from several handbooks [6.107–109], textbooks [6.119], and publications [6.69, 120]. Early sensitivity factors varied significantly [6.69], and it is not clear if these later values are consistent for the instruments intended or if significant uncertainties still persist. An analysis has not been made since the assessment in 1986 [6.69] showed that the sensitivity factor datasets were very variable. This partly arose because the IERFs of the instruments used were not measured in these handbooks. In the next section we address the basic concept of the peak intensities.

Quantitative Analysis of Locally Homogeneous Solids

Following the procedure for AES, the x-ray photoelectron intensity per photon of energy $h\nu$ into a small solid angle $d\Omega$ for a pure element A from the subshell X_i is given by

$$I^{\infty}_{AX_i} = n_{AX_i}\sigma_{AX_i}\sec\alpha N_A Q_A(E_{AX_i})\lambda_A(E_{AX_i}) \times\left[1+\tfrac{1}{2}\beta_{effAX}\left(\tfrac{3}{2}\sin^2\gamma-1\right)\right] \times\cos\theta\left(\frac{d\Omega}{4\pi}\right), \quad (6.24)$$

where n_{AX_i} is the population of electrons in the subshell i of the core level shell X of element A, σ_{AX_i} is the ionization cross section for that core level for photons of energy $h\nu$, α is the angle of incidence of the x-ray beam from the surface normal, γ is the angle between the incident x-ray beam and the direction of the photoemitted electrons, and the other terms are as for AES. Values of the product of n_{AX_i} and σ_{AX_i} are taken from the data of *Scofield* [6.121]. Other cross sections exist but have been shown to be less accurate [6.122].

At the magic angle, where $\gamma = 54.7°$, the final term in square brackets in (6.14) is unity. However, at other angles this function is generally higher than unity for $\gamma > 54.7°$. The values of β are tabled by *Yeh* and *Lindau* [6.123] and by *Reilman* et al. [6.124] as well as others. The parameter β is valid for gas-phase work, but in solids *Jablonski* [6.81] has shown that β is reduced to β_{eff} by elastic scattering. *Seah* and *Gilmore* [6.82] reduce Jablonski's Monte Carlo data to sets of equations

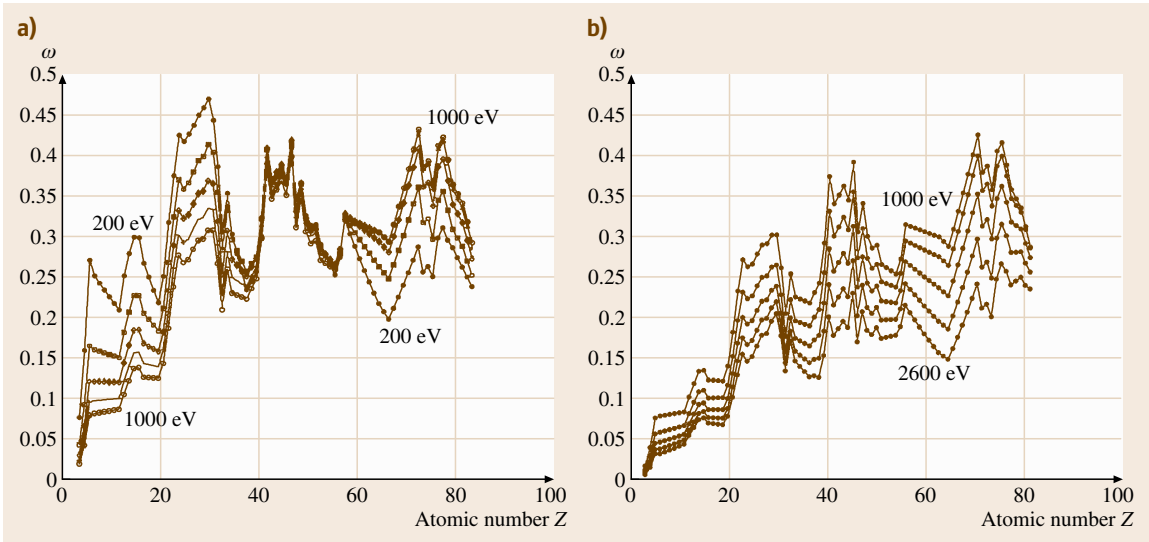

Fig. 6.7a,b Dependence of ω on Z for various electron kinetic energies: **(a)** at 200 eV intervals from 200 to 1000 eV and **(b)** at 400 eV intervals from 1000 to 2600 eV (after [6.82])

such as

$$\beta_{\mathrm{eff}}(\theta) = \beta_{\mathrm{eff}}(0)(1.121 - 0.208\cos\theta + 0.0868\cos^2\theta)\,, \tag{6.25}$$

where

$$\frac{\beta_{\mathrm{eff}}(\theta)}{\beta_{\mathrm{eff}}} = 0.876[1 - \omega(0.955 - 0.0777\ln Z)]\,, \tag{6.26}$$

where the value of ω may be read from graphs [6.82] or Fig. 6.7.

The above calculation gives the PERSFs for XPS. However, for quantification, as discussed above for AES, we really need AMRSFs and so may use (6.3). If we use PERSFs in (6.3) and effectively ignore the relevant matrix factors, the errors involved range from 0.3 to 3 [6.86]. Using PERSFs we obtain (6.16) and (6.17), except that the $[1 + r(E)]$ term is replaced by the term $[1 + 1/2\beta_{\mathrm{eff}}(3/2\sin^2\gamma - 1)]$. Then [6.86, 125]

$$I_{\mathrm{A}}^{\mathrm{Av}} = n_{\mathrm{AX}_i}\sigma_{\mathrm{AX}_i}N_{\mathrm{Av}}Q_{\mathrm{Av}}(E_{\mathrm{AX}_i})\lambda_{\mathrm{Av}}(E_{\mathrm{AX}_i}) \times G_{\mathrm{Av}}(E_{\mathrm{AX}_i})\,, \tag{6.27}$$

where [6.125]

$$G_{\mathrm{Av}}(E_{\mathrm{AX}_i}) = 1 + \tfrac{1}{2}\beta_{\mathrm{effAvAX}_i}(\theta)\left(\tfrac{3}{2}\sin^2\gamma - 1\right)\,. \tag{6.28}$$

Here, β_{eff} is calculated via (6.25) and (6.26) with $Z_{\mathrm{Av}} = 41$ and ω_{Av} deduced from Fig. 6.7 or the NIST databases [6.5, 126].

In the past, the differences between the PERSFs and AMRSFs have not been recognized, and in general, the experimental data have been for compounds and not elements and so relate more closely to AMRSFs. However, these had no spectrometer calibration and furthermore were often blended with PERSF calculations, leading to parameters that were ill defined but which were adjusted by manufacturers to give valid results on their equipment when tested against certain reference compounds. As noted in Sect. 6.1.1, tables of data for AMRSFs and their constituent parts are on the NPL website [6.3] under *Reference data* for the convenience of analysts.

Quantification of Thin Homogeneous Overlayers

An important use of XPS is the measurement of overlayer thicknesses of up to 8 nm. The intensities of a pure layer of A of thickness d on a substrate of B are given by

$$I_{\mathrm{A}} = I_{\mathrm{A}}^{\infty}\left\{1 - \exp\left[-\frac{d}{L_{\mathrm{A}}(E_{\mathrm{A}})\cos\theta}\right]\right\} \tag{6.29}$$

and

$$I_{\mathrm{B}} = I_{\mathrm{B}}^{\infty}\exp\left[-\frac{d}{L_{\mathrm{A}}(E_{\mathrm{B}})\cos\theta}\right]\,. \tag{6.30}$$

In the approximation of no elastic scattering, the L_{A} values would be the IMFPs λ_{A}. However, in the presence of elastic scattering, *Cumpson* and *Seah* [6.127] showed that λ_{A} should be replaced by the attenuation length L_{A} and that (6.29) and (6.30) were valid for $\theta \leq 58°$. *Seah* and *Gilmore* [6.82] analyze these data to show, as an analog to (6.16), that elastic scattering leads to

$$\frac{L}{\lambda} = 0.979[1 - \omega(0.955 - 0.0777\ln Z)]\,. \tag{6.31}$$

More detailed calculations by *Jablonski* and *Powell* [6.128] give similar results.

For general films, (6.29) and (6.30) are not easy to solve for d from values of I_{A} and I_{B}, since if $E_{\mathrm{A}} \neq E_{\mathrm{B}}$, the analysis must become iterative. For this reason, Cumpson devised the *Thickogram* to help solve this problem [6.129]. For metals and their oxides as overlayers, (6.29) and (6.30) can be used for the oxygen peak and the substrate in the metallic form. However, any adsorbed moisture on the surface adds to the oxygen peak [6.130], and a better method is to use the substrate metal intensities in the oxide (o) and elemental (e) states using XPS with peak synthesis. This has the advantage that $E_{\mathrm{A}} = E_{\mathrm{B}}$ sufficiently closely that their difference may be ignored. Thus, in XPS,

$$d = L_{\mathrm{o}}\cos\theta\ln(1 - R_{\mathrm{expt}}/R_{\mathrm{o}})\,, \tag{6.32}$$

where $R_{\mathrm{expt}} = I_{\mathrm{o}}/I_{\mathrm{e}}$ and $R_{\mathrm{o}} = I_{\mathrm{o}}^{\infty}/I_{\mathrm{e}}^{\infty}$. The value of R_{o} may be calculated, but for accurate measurements of d, it is recommended that R_{o} is measured experimentally using the same peak fitting as will be used for the analysis. If the samples can be reasonably cleaned, and if there is a significant range of thicknesses, a plot of I_{o} versus I_{e} gives the sought-after I_{o}^{∞} and I_{e}^{∞} as the intercepts of the axes, since from (6.29) and (6.30),

$$\frac{I_{\mathrm{o}}}{I_{\mathrm{o}}^{\infty}} + \frac{I_{\mathrm{e}}}{I_{\mathrm{e}}^{\infty}} = 1\,. \tag{6.33}$$

The use of (6.32) to quantify the thicknesses of thermal SiO_2 layers on Si wafers has been evaluated in a major international study [6.130, 131] involving comparison with medium-energy ion scattering (MEIS), Rutherford backscattering spectrometry (RBS), elastic backscat-

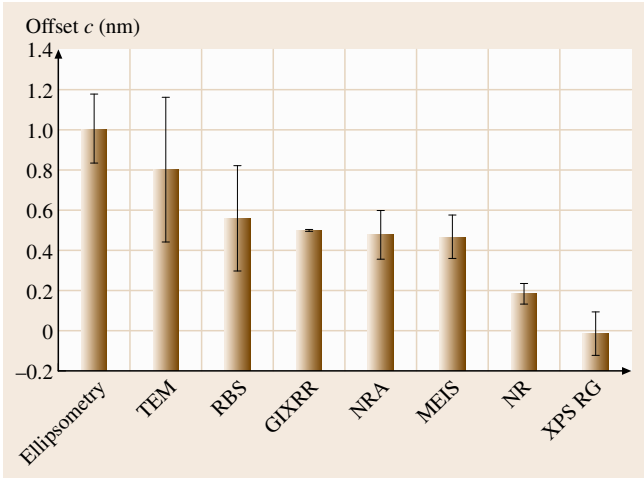

Fig. 6.8 The offsets c measured for various techniques, shown by their averages and standard deviations when compared with XPS (after [6.130]), updated for data in [6.134]. Note that one atomic layer is approximately 0.25 nm thick

tering spectrometry (EBS), nuclear reaction analysis (NRA), secondary ion mass spectrometry, ellipsometry, grazing-incidence x-ray reflectance (GIXRR), neutron reflectance (NR), and transmission electron microscopy (TEM). The thicknesses were in the range 1.5 nm to 8 nm to cover the range for ultrathin gate oxides. In order to use (6.32) reliably in XPS, the diffraction or forward-focusing effects of the crystal substrate need to be averaged or avoided [6.132]. To do this, a reference geometry (RG) is used with the emission direction at 34° to the surface normal in an azimuth at 22.5° to the [011] direction for (100) surfaces, and 25.5° from the surface normal in the [101] azimuth for (111) surfaces [6.132]. If these orientations are not chosen, R_o tends to be smaller and (6.32) gives a result that is progressively in error for thinner layers. Using the above approach, excellent linearity is obtained [6.133], and excellent correlations with the other methods show that L_o can be calibrated to within 1%, allowing XPS to be used with very high accuracy. Care needs to be taken, when working at this level, to ensure that the angles of emission are accurately known [6.134].

In the study, when matched against the XPS thickness d_{XPS}, most of the other methods lead to offsets c in the relation

$$d = md_{XPS} + c. \qquad (6.34a)$$

These offsets c are shown in Fig. 6.8 [6.130]. For MEIS, NRA, and RBS, the offset represents the thickness of the adsorbed oxygen-containing species, such as water, since these methods measure the total oxygen thickness rather than oxygen in SiO_2. An offset of 0.5 nm represents between one and two monolayers of water. For ellipsometry, where the measurements are in air, there is a further layer of hydrocarbon and physisorbed water that builds this up to around 1 nm. The offset for TEM is not understood and may arise from progressive errors in defining the thicknesses of thinner films. The offsets for GIXRR and NR also arise from the contaminations but are weaker in NR and may, in the future, be fully removed by modeling.

For quantitative measurement of the thicknesses of organic layers A, *Seah* and *Spencer* [6.135] use (6.30) where the attenuation length $L_A(E_B)$ is given by

$$L_A(E_B) = 0.00837E_B^{0.842}. \qquad (6.34b)$$

The analyses of more complex profiles are discussed by *Cumpson* [6.87] and by *Tougaard* [6.88].

Sputter Depth Profiling

There is essentially very little difference between sputter depth profiling using XPS and that using AES except concerning certain practical issues. Firstly, if unmonochromated sources are used, the larger area analyzed requires a larger area to be sputtered and generally a poorer depth resolution is obtained. This arises from the difficulty in retaining a flat, uniform depth over a larger area. With focused monochromators this should not be a problem, but the depth resolution is rarely as good as for AES. Secondly, the need to maintain a good vacuum environment around the x-ray source discourages the use of in situ, large-area ion guns with their higher gas loads.

Much of the advantage of XPS – of measuring the chemical state – is lost as a result of the changes in composition brought about by preferential sputtering by the ion beam. Thus, XPS depth profiling has been less popular than AES, but recent work has shown that, in organic materials, the chemical state may be retained if the primary sputtering ions are C_{60} [6.136] or argon clusters [6.137]. These have excellent promise for XPS and SIMS [6.138].

6.1.3 Secondary Ion Mass Spectrometry (SIMS)

General Introduction

In secondary ion mass spectrometry, atoms and molecules in the surface layers are analyzed by their removal using sputtering and subsequent mass analysis

in a mass spectrometer. The majority of emitted ions come from the outermost atom layer. Unfortunately, most of the particles are emitted as neutral atoms and only 10^{-4}–10^{-2} are emitted as ions. Nevertheless, the detection capability of SIMS is generally far superior to those of AES or XPS. A second problem is that the intensity of the ion yield is extremely matrix sensitive, and there are, as yet, no methods for calculating this effect accurately [6.139]. These properties have led to SIMS becoming very important in two major fields and being used in two distinct ways.

Historically, the most important approach has been that of dynamic SIMS, and this has found major use in characterizing wafers for the semiconductor industry. It is here that measurement issues are critical, and so it is here that we shall focus. More recently, the second approach – that of static SIMS – has been able to provide unique information concerning complex molecules at surfaces. Static SIMS has been in use for more than 30 years, but recent instrumental developments have made the method reliable and more straightforward for industrial analysts to use. We shall treat these fields separately below, but note that their separation is reducing. In a recent analysis of publications for the biennial SIMS conferences [6.141], the historical dominance of dynamic SIMS has disappeared, and research effort is currently slightly biased in favor of static SIMS.

Dynamic SIMS

In dynamic SIMS, the use of well-focused ion beams or imaging mass spectrometers allows submicrometer images of the surface to be obtained with very high sensitivity and facilitated isotope detection. At present, 50 nm spatial resolution can be achieved. High-resolution imaging is usually achieved with the removal of a significant amount of the surface material, which is why it is called dynamic SIMS or (historically) just SIMS. The dynamic removal of material allows composition depth profiles to be measured, and it is these profiles for the semiconductor industry that account for much of the routine industrial analysis. All of the ISO standards in this area (Tables 6.2, 6.3), certified reference materials, and two-thirds of the dynamic SIMS applications at meetings [6.141] concern depth profiling with semiconductors. There are two essential measurement issues that require quantification in sputter depth profiles for dopants in semiconductors: the composition and the depth scale. However, these cannot be evaluated in many cases without considering the depth resolution. SIMS is very powerful when studying dopants, since the method has the high sensitivity required for the low concentrations, as shown in Fig. 6.9. Fortunately, the peak concentration levels are still sufficiently low that linearity of composition and signal can still, generally, be assumed. We shall start by considering the depth resolution.

Depth Resolution. In AES and XPS, we have defined the depth resolution from the profile width of a sample characterized by a step-function composition. This is very useful for the small dynamic range of those spectroscopies, but in SIMS it is more useful to char-

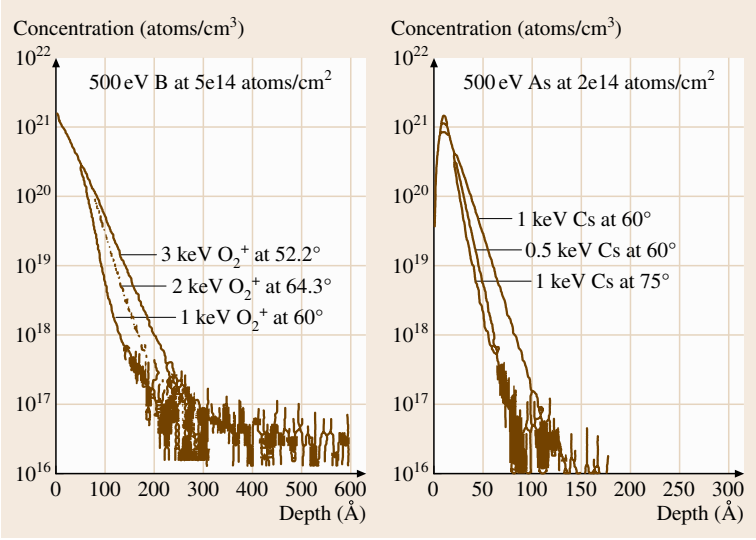

Fig. 6.9 Profiles of 500 eV boron and 500 eV arsenic implants in silicon using O_2^+ and Cs^+ ion beams (after *Hitzman* and *Mount* [6.140]). These show the benefit of very low-energy primary ion beams

acterize the resolution by the slope of the exponentials describing the up or down slopes as the new region is entered or exited. These slopes are termed the leading edge decay length λ_c and the trailing edge decay length λ_t in ISO 18115, and are defined as the characteristics of the respective exponential functions. These have a physical basis, unlike the descriptions used for AES or XPS. Since one is often dealing with dilute levels, the depth resolution is best characterized by the up and down slopes from delta layers. The method for estimating depth resolution in this way is described in ISO 20341, based on the analytical description of *Dowsett* et al. [6.142] and illustrated, with detailed data, by *Moon* et al. [6.143] using five GaAs delta layers in Si at approximately 85 nm intervals.

In Fig. 6.9, one clearly sees that the ion beam species, angle of incidence, and energy all affect the depth resolution, and that this affects the tail of the dopant distribution, its half-width, and the position and magnitude of the peak. It is generally also true that, the lower the beam energy and more grazing the incidence angle, the better the depth resolution. In many mass spectrometers, a high extraction field is used to focus all of the ions ejected from the sample into the mass spectrometer, and the consequent field around the sample effectively limits the choice of energy and angle of incidence. To avoid this limitation, the traditional quadrupole mass spectrometer has retained its popularity. With these mass spectrometers, the low extraction field allows very low-energy ion guns to be utilized [6.144, 145]. For instance, *Bellingham* et al. [6.146] show that, for a 1 keV ^{11}B implant, the trailing edge decay length λ_t, when profiled using O_2^+ at normal incidence, increased with the beam energy E approximately as

$$\lambda_t = 0.13 + 0.1E\,, \tag{6.35}$$

where λ_t is in nm and E is in keV. The lowest value, 0.14 nm, was obtained using a 250 eV O_2^+ beam (125 eV per atom). For delta layers, the trailing edge decay length is always greater than the leading edge decay length as a result of the forward projection of the dopant atoms. Therefore, attention is directed above to λ_t.

Considerable effort is expended designing focused ion beams that work at these low energies and yet still have sufficient current density to be able to profile significant depths in a reasonable time for practical analysis. Use of more grazing incidence angles is also beneficial [6.145, 146], but this can usually only be achieved by tilting the sample, and this generally detrimentally affects the ion collection efficiency. The choice of ion species also affects the depth resolution, and in general, the larger the incident ion cluster, the lower the energy per constituent atom and the shorter the trailing edge decay lengths. Thus, *Iltgen* et al. [6.147] show that, when profiling delta layers of B in Si with 1 keV ions and with O_2 flooding of the sample, SF_5^+ is better than O_2^+, which in turn is better than Xe^+, Kr^+, Ar^+, and Ne^+.

Recognizing the limitation of λ_t for shallow implants being affected by the atomic mixing, many authors [6.148–150] now experiment with removing the substrate chemically and profiling the critical layer from the backside. This reduces the atomic mixing and should improve the detection limit, but issues then arise from the flatness of the substrate removal.

Depth. The depth scale may be obtained by using the signal from a marker layer at a known depth, or by measuring the depth of the crater after profiling, or by calculating from the sputtering yield. The latter route [6.93,104] is very convenient but only accurate, as noted earlier, to some tens of percent. The usual route is to use a stylus depth-measuring instrument, as described in Sect. 6.2.1, to define the crater depth in the region from which the signal is obtained. Alternatively, as discussed in ISO 17560, optical interferometry, as described in Sect. 6.2.2, may be used. Both of these give an accurate measurement of the crater depth d_o at the end of the profile at time t_o. Analysts then generally scale the depth d at time t according to

$$d = \frac{d_o}{t_o} \tag{6.36}$$

using the assumption that the sputtering yield or sputtering rate is constant. Unfortunately, this is only true once equilibrium is established.

At the present time, we cannot accurately calculate how the sputtering rate changes as the surface amorphizes and the incident ions dynamically accumulate in the eroding surface layer, but the effect can be measured. *Moon* and *Lee* [6.151] show, for instance, that the sputtering yield of Si falls from 1.4 to 0.06 as a result of 3.5×10^{16} 500 eV O_2^+ ions cm^{-2} incident normally on an amorphous Si layer. *Wittmaack* [6.152] finds that the rate for O_2^+ ions at 1 and 1.9 keV, at 55–60° incidence, falls to 40% after sputtering 2–5 nm. In more recent work studying thermal SiO_2 films, *Seah* et al. [6.130] find that the rate, when using 600 eV Cs^+, falls similarly by a factor of two over the initial 1.5 nm.

In a recent study by *Homma* et al. [6.153] using multiple BN delta layers in Si with pitches of 2 or 3 nm,

it is shown that the sputtering rate for 250 eV O_2^+ ions falls by a factor between 1.2 and 1.43, depending on the delta layer pitch and the ion beam angle of incidence. At 1000 eV, a factor of 3.5 is seen for the 3 nm pitch delta layers. In an interlaboratory study of seven laboratories profiling these samples, this effect has been further studied by *Toujou* et al. [6.154]. Homma et al.'s data were repeated but, with the addition of O_2 flooding, the effect could be largely removed.

In addition to the nonlinearity occurring whilst the equilibrium is being established, a longer-term nonlinearity arising from the development of surface topography also occurs. This occurs when using O_2^+ bombardment to enhance the ion yields and to homogenize the matrix. It has been found for both Si and GaAs [6.155]. The surface starts smooth, but at a critical depth, ripples develop on the surface, orientated across the incident beam azimuth [6.156]. The critical depth for the onset of roughening has been reviewed by *Wittmaack* [6.157], who shows that, in vacuum without O_2 flooding, the critical depth for impact angles in the range 38–62° falls from 10 μm at 10 keV approximately linearly with energy to 1 μm at 3 keV, but then approximately as $E^{4.5}$ to 15 nm at 1 keV beam energy. Once roughening has been established, the Si^+ and other signal levels used to normalize the sputtering rate change and, at the same time, the sputtering rate reduces. In many studies, O_2 flooding is used, but *Jiang* and *Alkemade* [6.158] show that this causes the roughening to occur more rapidly, such that, for a 1 keV beam at 60° incidence and intermediate O_2 pressures, the erosion rate had fallen after a critical depth of 50 nm and, above 3×10^{-5} Pa, the critical depth reduces to 20 nm. Use of other ion sources, such as Cs^+, does not improve things [6.159].

The final issue that affects the measured rate of sputtering is that the crater depth only measures the thickness of material removed for deep craters. For shallow craters, as noted for AES, there will be some swelling of the crater floor resulting from implanted primary ions as well as postsputtering oxidation when the sample is removed from the vacuum system for measurement. For inert gas sputtering, the swelling should be small, since the take-up of inert gas is only some 2–3% over the projected range of the ion [6.104]. Similarly, on exposure to air, for Si, approximately 1 nm of oxide will be formed, which will cause a net swelling of around 0.6 nm. The whole swelling, therefore, may be 1 nm, and this is generally ignored for craters with depths greater than 100 nm. For other ion beams, the swelling arising from implantation may well be significantly higher than this, but data do not exist to estimate the effect, except for, say, O_2^+, where if a zone 1 nm thick is converted to SiO_2, we get the above 0.6 nm swelling but nothing further upon air exposure.

Even if we have the correct depth scale, there is a final issue that profiles appear to be shifted from their true positions, since the atoms of a marker layer of interest are recoiled to a different depth from that of the matrix atoms [6.160]. Further shifts in the centroids and the peaks of delta layers arise from the atomic mixing and interface broadening terms as well as the effects of nearby delta layers [6.161]. The shifts seen by *Dowsett* et al. [6.161] were all less than 3 nm and arise from the overall asymmetry of the measured profile for each delta layer.

Thus, obtaining a repeatable depth scale with modern instruments when profiling dopants in Si is relatively simple. The ion beam sources are reasonably stable, and that stability may be monitored in situ via a matrix signal such as Si^+. However, translating that to an accurate depth scale, particularly for ultrashallow depth profiles, is currently not routine and (depending on the sample) may involve significant errors.

Quantification. Quantification in dynamic SIMS is very important for semiconductor studies. Equations such as (6.3) can be used, but it is found that the sensitivity factors cannot really be used from lookup tables, since the factors vary too much from instrument to instrument and condition to condition. However, by using a reference material, this may be overcome. Two types of reference material are employed: bulk doped and ion implanted. Either type of sample may be used just prior to or following the sample to be analyzed with identical analytical conditions. If these analyses occur regularly, the data from the reference material may be used in statistical process control procedures to underpin a quality system and ensure consistent instrument operation.

ISO 18114 shows how to deduce relative sensitivity factors (RSFs) from ion-implanted reference materials. At the present time, not many of these exist at the certified reference material level. NIST sells ^{75}As-, ^{10}B-, and ^{31}P-doped Si as SRMs 2134, 2137, and 2133, respectively, with levels of around 10^{15} atoms/cm^2 but certified with 95% confidence limits ranging from 0.0028×10^{15} atoms/cm^2 for As to 0.035×10^{15} atoms/cm^2 for B. KRISS also provides B-doped Si thin films as KRISS CRM 0304-300. Using an implanted material, one measures the implant signal I_i^x as a function of the depth d through the profile until the implant or dopant signal has reached the back-

ground noise level I_∞^x. From the total implanted dose N (atoms/m^2), the sensitivity factor S_x may be calculated as

$$S_x = \frac{Nn}{d\sum_{i=1}^{n}\left(\frac{I_i^x - I_\infty^x}{I_i^m}\right)}\,, \tag{6.37}$$

where I_i^m is a normalizing matrix signal and n cycles of measurement are required to reach the crater depth d, which must be measured after the profile using a profilometer or other calibrated instrument.

The concentration C_i^x at any point is then given by

$$C_i^x = S_x \frac{I_i^x - I_\infty^x}{I_i^m}\,. \tag{6.38}$$

Bulk-doped reference materials are also useful, and here, if the concentration of the reference material is K^x,

$$S_x = \frac{K^x}{\left(\frac{I_i^x - I_\infty^x}{I_i^m}\right)}\,. \tag{6.39}$$

The background level I_∞^x in this case must be determined from a sample with a very low level, which may occur, for example, in part of the sample to be analyzed. In all of these situations, one must be aware that one is only measuring the intensity of one isotope and that the reference sample may have a different isotope ratio from that of the sample to be analyzed. If this is the case, corrections will be needed in (6.37–6.39) to allow for the relevant fractions. These issues are dealt with in detail for B in Si using bulk-doped material and ion-implanted reference materials in ISO 14237 and ISO 18114, respectively.

A number of interlaboratory studies have been carried out on these materials, and it is useful to summarize the results here so that users can see the level of agreement possible. In very early studies for B in Si, *Clegg* and coworkers [6.162] showed very good results for a 70 keV ^{11}B ion-implanted wafer between ten laboratories using either O_2^+ or Cs^+ ion sources in the range 2–14.5 keV. For this relatively broad profile, the average standard deviation of the widths at concentrations equal to 10^{-1}, 10^{-2}, 10^{-3}, and 10^{-4} of the maximum concentration was 2.8%, the depth typically being 500 nm. Later work [6.163] using ^{66}Zn, ^{52}Cr, and ^{56}Fe sequentially implanted into GaAs showed slightly poorer results. That work also showed that elements accumulating near the surface, where the sputtering equilibrium is being established, would lead to variable results. A later study by *Miethe* and *Cirlin* [6.164] analyzing Si delta-doped layers in GaAs found good results but that, to obtain meaningful depth resolution, laboratories at that time needed both better control of their scanning systems for the flat-bottomed crater, and to use sample rotation to avoid the degrading effects of developing sample topography.

To cover a wider range of dopant concentrations, *Okamoto* et al. [6.165] analyzed 50 keV $^{11}B^+$-implanted wafers with doses from 3×10^{14} to 1×10^{17} ions/cm^2. Eighteen laboratories profiled these samples using $^{11}B^+$ and $^{27}BO^+$ when using positive ion detection with O_2^+ incident ions, or $^{39}BSi^-$ and $^{11}BO^-$ when using negative ion detection with Cs^+ incident ions. The signals are, of course, ratioed to those of the relevant matrix ions. These results showed good consistency but that the RSFs for $^{11}B^+$ and $^{11}B^-$ were affected by the matrix for the two higher B implant levels, the RSFs being slightly reduced. In an extension of this work for shallow implants for ultralarge-scale integration (ULSI) devices, *Toujou* et al. [6.166] note that, at 1×10^{16} ions/cm^2, the peak B concentration is over 10^{21} atoms/cm^2, in other words over 1% atomic fraction. They find that, for 4 keV O_2^+ at impact angles $\theta > 30°$, the B and Si ion yields increased for concentrations $> 10^{21}$ atoms/cm^3, but, under 4 keV Cs^+ bombardment, no increase occurred up to 60°. They therefore recommend using O_2^+ at $\theta < 20°$ or Cs^+ at $\theta < 60°$ incidence angle to avoid the nonlinearity at high concentrations. These angle issues are not discussed in the relevant standards ISO 14237 and ISO 17560, but there it is recommended to measure both $^{10}B^+$ and $^{11}B^+$ when using an oxygen beam and $^{10}B^{28}Si^-$ and $^{11}B^{28}B^-$ with a cesium ion beam. The ^{28}Si ion or its molecular ions should be used as the matrix ion, and the ratios of the dopant and matrix ions are determined for each cycle of measurement as in (6.36–6.38).

In more recent work for the draft ISO 12406, *Tomita* et al. [6.167] have studied the depth profiling of 100 keV $^{75}As^+$ implants in Si for doses between 3×10^{14} and 3×10^{16} ions/cm^2 with peak concentrations up to 5.8×10^{21} atoms/cm^3 (12 at. %). They find that, for Cs^+ incident ions, use of the ion intensity ratios $AsSi^-/Si_2^-$ or As^-/Si^- as the measured intensities, with point-by-point normalization, leads to constant RSFs for all doses and for angles of incidence in the range 24–70°. However, use of the intensity ratios $AsSi^-/Si^-$ or As^-/Si_2^- led to 10% changes in the RSF at arsenic doses of 10^{16} ions/cm^2 and above and were not recommended. It is likely that these issues will be included in a future ISO standard.

Static SIMS

In dynamic SIMS, with the use of low energies and high incidence angles, many uncertainties are focused into the first 1 nm of depth, during which the sputtering process comes to equilibrium. In static SIMS, it has traditionally been suggested that the upper limit of fluence should be restricted to about 0.1% of this, and early work suggested that it should be less than 10^{13} ions/cm^2 for molecular analysis. The intensities of certain peaks may be expressed as

$$I = I_o \exp(-N\sigma t)\,, \tag{6.40}$$

where N is the number of ions/(m^2 s) arriving at the surface, t is the time, and σ is a damage cross section. For I to represent I_o to within 10%, and for a sputtering yield in the range 1–10, one can see that elements at the surface can only be analyzed using fluences up to 10^{13} ions/cm^2. However, *Gilmore* and *Seah* [6.168] showed that, the larger the fragment studied, clearly the larger the physical cross section of the molecular fragment and the higher the value of σ, so that a 10% loss of intensity of the group $C_{10}H_9O_4$ from poly(ethylene terephthalate) occurred at an argon fluence of 10^{12} ions/cm^2. For the smaller C_6H_4 ion, 5×10^{12} argon ions/cm^2 could be tolerated.

Today, molecules of very much larger physical sizes are analyzed with concomitantly lower damage thresholds, but fortunately, modern time-of-flight mass spectrometers used for SIMS studies only need a total of 10^9 ions, and with a useful ion yield of 10^{-4}, the spectrum has an excellent 10^5 ions. This may be achieved in typical systems using a pulsed ion source delivering 600 ions per pulse every 100 µs for a total spectrum acquisition time of 3 min. If this dose is spread out over a raster area of 300 µm by 300 µm, the fluence is just at the 10^{12} cm^{-2} static limit. However, for spatially resolved data this is no longer possible, and damage becomes an important issue. This needs consideration in order to generate reliable and repeatable data. The next important issue is to interpret that data, and we shall deal with these aspects in the next sections.

Control of Damage. Two sources of damage arise in static SIMS: the primary ions, and the electrons from the electron flood neutralizing system for discharging insulators for analysis. As noted earlier, most analysts keep the ion fluence below 10^{12} ions/cm^2 to avoid damage, although for the study of larger molecules, such as proteins, which may have a cross-sectional area of 20 nm^2, one may expect 20% to be damaged at this dose and 2×10^{11} ions/cm^2 may be a safer limit. This leads to an optimum spatial resolution of 0.7 mm for spectra with 10^5 counts.

Depending on the information required, one can, of course, work at much better spatial resolution, as shown in Fig. 6.10. In the study in Fig. 6.10, it is known that there are essentially two regions, since the sample was made to be a polymer blend of polyvinylchloride (PVC) and polycarbonate (PC) that are phase separated but may be partially miscible. Here, one can work to lower signal levels per pixel and then sum pixels to obtain low-noise spectra. One may also use a higher dose to consume more of the material. Thus, for PVC one may use the Cl^- signal, and for PC the sum of the O^- and OH^- signals. In Fig. 6.10, the images comprise 256×256 pixels with a dose per pixel of 10^4 ions, giving a total of 6×10^8 ions into the 50×50 µm^2 area and a fluence of 2.5×10^{13} ions/cm^2. For a good static SIMS spectrum at the 10^{12} ions/cm^2 level, we must analyze 150×150 µm^2 using a total number of 2.25×10^8 ions, as shown in Fig. 6.11. Fortunately, here we have a useful ion yield in the negative ions of 10^{-3}–10^{-2}, so that each pixel of the left-hand image of Fig. 6.10 contains 10–100 Cl^- ions. We can see patterns of dark dots within the bright zones. These are not noise, but can be shown by AFM to be 200 nm-diameter pools of PC [6.1]. The SIMS is just resolving these generally as single pixels, indicating a static SIMS resolution, in a near-static mode, of 200 nm.

Figures 6.10 and 6.11 show typical analyses of materials using a modern time-of-flight SIMS system. The samples are insulating and need electron flooding to remove charge. This is relatively easy, but in practice we have found that many users ensure charge neutralization

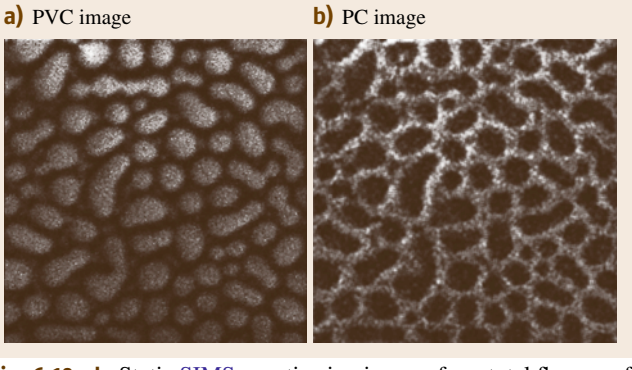

Fig. 6.10a,b Static SIMS negative ion images for a total fluence of 2.5×10^{13} ions/cm^2 of a PVC and PC polymer blend: **(a)** Cl^- for PVC and **(b)** $OH^- + O^-$ for PC; field of view 50×50 µm^2 (after *Gilmore* et al. [6.1])

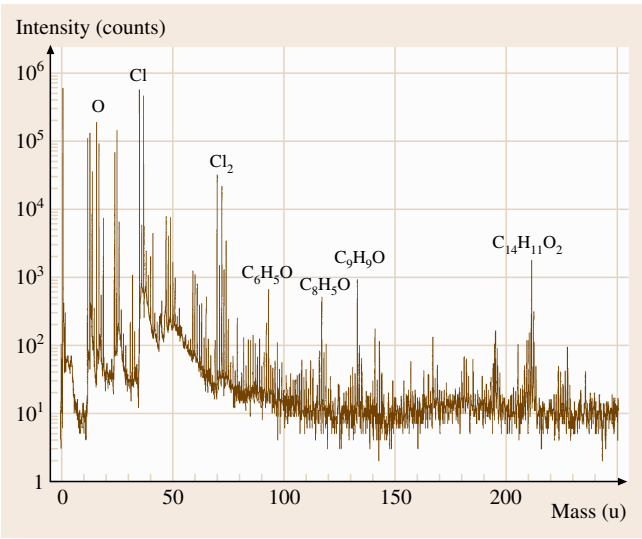

Fig. 6.11 Static SIMS negative ion spectrum for 10^{12} ions/cm^2 on a fresh $150 \times 150\,\mu m^2$ area of material as in Fig. 6.10 (after *Gilmore* et al. [6.1])

by using an electron flux density that is far too high. This ensures that there is no charging, but it damages the sample at about the same rate as the ions. Low-energy electrons have a very high cross section for bond dissociation. *Gilmore* and *Seah* [6.169] find that, at electron fluences of 6×10^{14} electrons/cm^2, polymers such as PS, PVC, poly(methyl methacrylate) (PMMA), and polytetrafluoroethylene (PTFE) are damaged, whereas some instruments have been set well above this limit. The avoidance of electron flood damage typically limits the electron flood current to 100 nA, but as a minimum, the sample needs about 30 electrons per incident ion to stop significant charging.

Identifying Materials. In static SIMS we cannot identify materials, beyond elemental species, simply by observing the masses of the peaks. For the molecules generally studied, there are very many mass peaks of high intensity in the 12–100 u range and often series of peaks at masses up to and beyond 1000 u. The unit u here is the unified atomic mass unit, often also called the dalton. The peaks mainly correspond to highly degraded fragments of the original molecules or material at the surface. This degradation is such that many organic materials look broadly similar, and experts develop their own schemes of selected significant peaks in order to measure intensities. Thus, much information is rejected. In order to identify materials in this way, static SIMS libraries have been developed. The first two libraries [6.170, 171] were in a print-on-paper format, effectively using unit mass resolution since they arose from very careful data compilations using the earlier quadrupole mass spectrometers. Despite the care, contamination and damage effects are more likely in these data. These libraries contain 81 materials and 85 polymers, respectively. The more recent library by *Vickerman* et al. [6.172] extends the earlier library [6.170] by including spectra for the higher mass resolution, early time-of-flight instruments so that the combined library now covers 519 materials. The fourth library [6.173] is for consistent high-resolution data, is available digitally, and is for calibrated, later generation time-of-flight instruments. This contains data for 147 compounds. These libraries form an invaluable resource to which analysts may add their own data. For quantification, analysts typically select one or two major characteristic peaks and simply use equations such as (6.3). Individual research groups use much more sophisticated analyses, but these are not applicable for general analysis.

The modern time-of-flight mass spectrometer should be able to determine mass to better than the 10 ppm needed to be able to associate each peak with the correct number of C, O, N, H, and so on, atoms. However, a recent interlaboratory study [6.174] shows that, even having calibrated the scale on appropriate masses, a lack of understanding of the issues involved [6.175] leads to a standard deviation of scatter of 150 ppm for the protonated Irgafos peak at 647.46 u [6.174]. Thus, at the present time, the lack of an appropriate procedure means that analysts need to check a range of possibilities to identify each peak.

The spectrum measured in a laboratory may differ from that shown in a database library for one or more of several reasons. Even when using reference samples to generate a library, great care needs to be taken to avoid contaminants, for example poly(dimethyl siloxane) (PDMS). Secondly, in the first static SIMS interlaboratory study [6.176], it was shown that, whilst some laboratories could repeat data at a 1% level, 10% was more typical and 70% occurred in some cases, indicating that some laboratories/instruments could not really generate repeatable data. In that work the 18 analysts used 21 instruments and their preferred ion sources ranged from Ar^+ and Ga^+ to Cs^+ and O_2^- with primary ion beam energies from 2.5 to 25 keV. In a more recent study [6.169], improvements in practice and equipment have led to a general improvement in repeatability, but the issue of different sources remains.

To study larger molecules, a range of new ion sources has been developed to provide a higher yield of large fragments compared with the sources listed above. *Benninghoven* et al. [6.177] show that the yields of all fragments increase through the primary ion series Ar^+, Xe^+, SF_5^+, $C_{10}H_8^+$, $C_6F_6^+$, $C_{10}F_8^+$ when analyzing Irganox 1010 at the surface of polyethylene. These results, for 11 keV ions, covered the mass range 50–1000 u and indicated a simple increase above 100 u of 0.3, 1, 4, 6, 7, and 12, respectively, when normalized to the Xe^+ data. Below 150 u the increases were stronger. For matrix-isolated biomolecules, a change from Ar^+ to SF_5^+ led to yield increases of characteristic peaks above 1000 u of 6–32 times. *Schneiders* et al. [6.178] show that, for molecular overlayers of adenine and β-alanine on Ag or Si, SF_5^+ gives significantly higher yields than Xe^+ and that this is, in turn, better than Ar^+. These overall results are nicely summarized in the studies of *Kersting* et al. [6.179, 180], who look at both the yield increase and the damage effects, as shown in Fig. 6.12, where they call σ in our (6.40) the disappearance cross section. They define the ratio of the yield to the damage cross section as the efficiency E. Clearly, if the yield doubled at the expense of twice the rate of damage, there would be no real improvement for the analyst and this would be reflected in an unchanged value of the efficiency E. However, in Fig. 6.12 it is clear, where data are given for C_{60}^+, Au_3^+, Au_2^+, Au^+, SF_5^+, Cs^+, and Ga^+, that they are 2000, 500, 200, 33, 45, and 6 times better than Ga, respectively. It seems that higher mass ions are better than low mass, and polyatomic ions are better than monatomic ions of the same beam energy.

Earlier studies of polyatomic ions identified C_{60}^+ as an interesting candidate. *Wong* et al. [6.181] have designed a suitable ion gun and show significant yield enhancements compared with Ga^+ at 15 keV. The total yield increase for the polypeptide gramicidin, spin-cast onto copper, is 41 and, in the 200–1000 u range, rises to 50. For the molecular ion, a strong signal is observed for C_{60}^+ but not at all for Ga^+. The results for bulk polyethylene terephthalate (PET) were around 60 for most of the mass range for equivalent doses of both ions. The damage rates were not measured, but the very strong result for the gramicidin molecular ion showed significant promise. More recently, *Weibel* et al. [6.182] extended this work and measured the Y, σ, and E values to show that E for masses above 250 u would range from 60 to 15 000 times higher for C_{60}^+ than for Ga^+ when analyzing thick polymer or Irganox 1010 layers.

In recent analysis of the data for Fig. 6.12, *Seah* [6.183] shows that there is a clear improvement in both sensitivity and efficiency through the series and that the larger clusters are very beneficial in studying organic materials.

To increase the mass of the projectile for the liquid metal ion gun structures used for high-resolution imaging, *Davies* et al. [6.184] have used a gold ion source. Using a gold-germanium eutectic alloy as the source for a liquid metal ion gun, they could generate Ge^{2+}, Ge^+, Au^{2+}, Au^+, Au_2^+, and Au_3^+ beams all at around the 1 pA needed. The results, compared with Ga^+ for the gramicidin and PET analyzed with the C_{60}^+, show that Au^+ gives typically a fourfold improvement and that Au_3^+ gives a tenfold improvement, except for the gramicidin

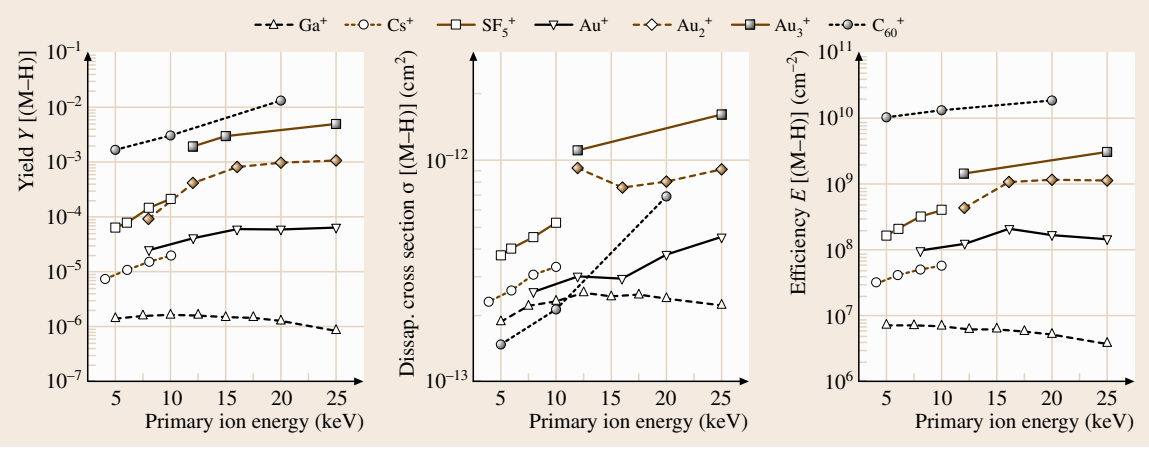

Fig. 6.12 Secondary ion yields, damage or disappearance cross section σ, and efficiency E measured for the Irganox 1010 quasimolecular ion $(M-H)^-$ as a function of the primary ion energy and type (after *Kersting* et al. [6.180])

molecular ion where the improvement is 64 times. It appears that Au_3^+ is less effective at generating the molecular ions for gramicidin than C_{60}^+, but no data are available for the damage rates to evaluate the efficiencies. Clearly, the liquid metal ion source approach will continue to provide better spatial resolution, and so we expect that there will be further new sources in the future. This does not help the analyst trying to use the spectral libraries, since the relative intensities of the peaks depend on the ion source. For the analyst there is an urgent need for

1. a routine to treat spectra so that they may be related from one source to another,
2. a procedure for accurate mass calibration, and
3. a chemometrics platform to be able to apply reliable algorithms to extract chemical information directly from the spectra.

To aid this process in static SIMS, two standards, ISO 14976 and ISO 22048, as shown in Table 6.2, have been designed to allow export and import of spectral data files so that new software may be developed to do this processing.

In recent years a variant of static SIMS has been developed called G-SIMS. This spectroscopy uses the ratio of two static SIMS spectra to generate a new spectrum called the G-SIMS spectrum that contains peaks far less degraded in the fragmentation process. As a result of the characterization for the static SIMS interlaboratory study [6.174], it was shown that the ratio of the spectrum obtained for 4 keV argon to that for 10 keV argon exhibited clusters of results near unity but with fragments of the type C_xH_y having the highest ratio for the least degradation [6.186]. The G-SIMS spectrum I_x for the mass x is given by

$$I_x = F_x^g N_x M_x \,, \tag{6.41}$$

where the ratio of the 4 and 10 keV spectra is F_x, g is the G-SIMS index, N_x is the 4 keV static SIMS spectrum, and M_x is a linear mass term. In practice, for 4 and 10 keV argon, a useful value of g is found to be 13. Tests with other sources shows that, whilst 4 and 10 keV argon is convenient and is an easy choice to be able to align the beams on the same area, SF_5^+, Cs, and Xe may be ratioed to Ar or Ga and a stronger effect obtained [6.186]. An example of G-SIMS is shown in Fig. 6.13 for poly-L-lysine [6.185]. Figure 6.13a is the static SIMS spectrum where the poly-L-lysine structure is shown. The spectrum is, as usual, dominated by the low mass fragments. In Fig. 6.13b is a G-SIMS spectrum using the ratio of 10 keV Cs to 10 keV Ar and a g index of 13 [6.185]. The intense double peak in the center arises from a separate bromide compound as the material is supplied as a salt. The G-SIMS peaks show a clear dimer with an added NH and a peak defining the amino acid side-chain. A number of polymers [6.186] and organics [6.185] have been studied, and each time the information can be related to unfragmented parts of the molecule.

In a test of the capability of G-SIMS, investigations of a small brown stain on paper identified oil of bergamot from the molecular peak that was not noticeable in the static SIMS spectrum. Identifying species from the molecular weight is thus possible using G-SIMS and, possibly, Au_3^+ or C_{60}^+. This frees the analyst from the limit of fewer than 800 materials defined by the spectra available in libraries of static SIMS spectra [6.170–

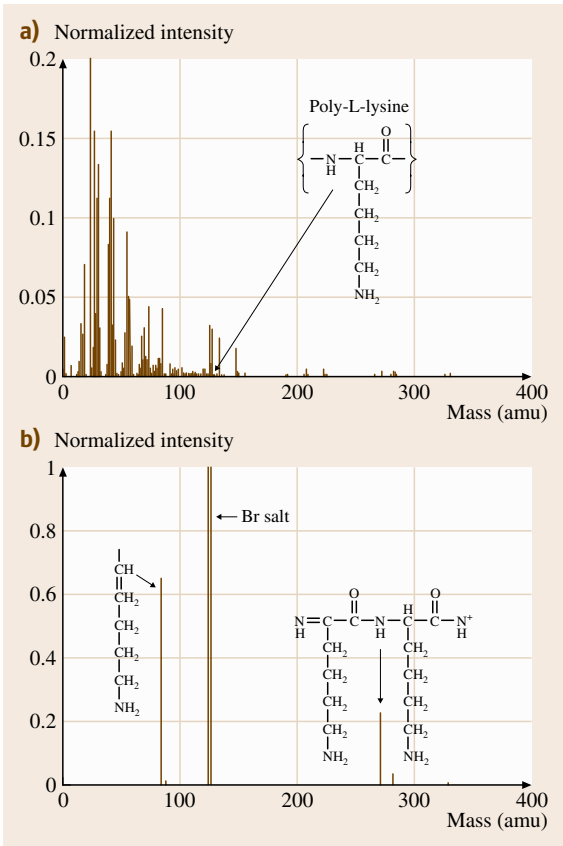

Fig. 6.13a,b Spectra for poly-L-lysine: **(a)** 10 keV Cs^+ static SIMS spectrum showing strong fragments at low mass and no peak at the repeat unit of 128 u, and **(b)** G-SIMS using the ratio of 10 keV Cs^+ to Ar^+ with strong intensity at 84.1 u for the side-chain and 271.2 u for a dimer repeat with an extra NH from the backbone (after *Gilmore* and *Seah* [6.185])

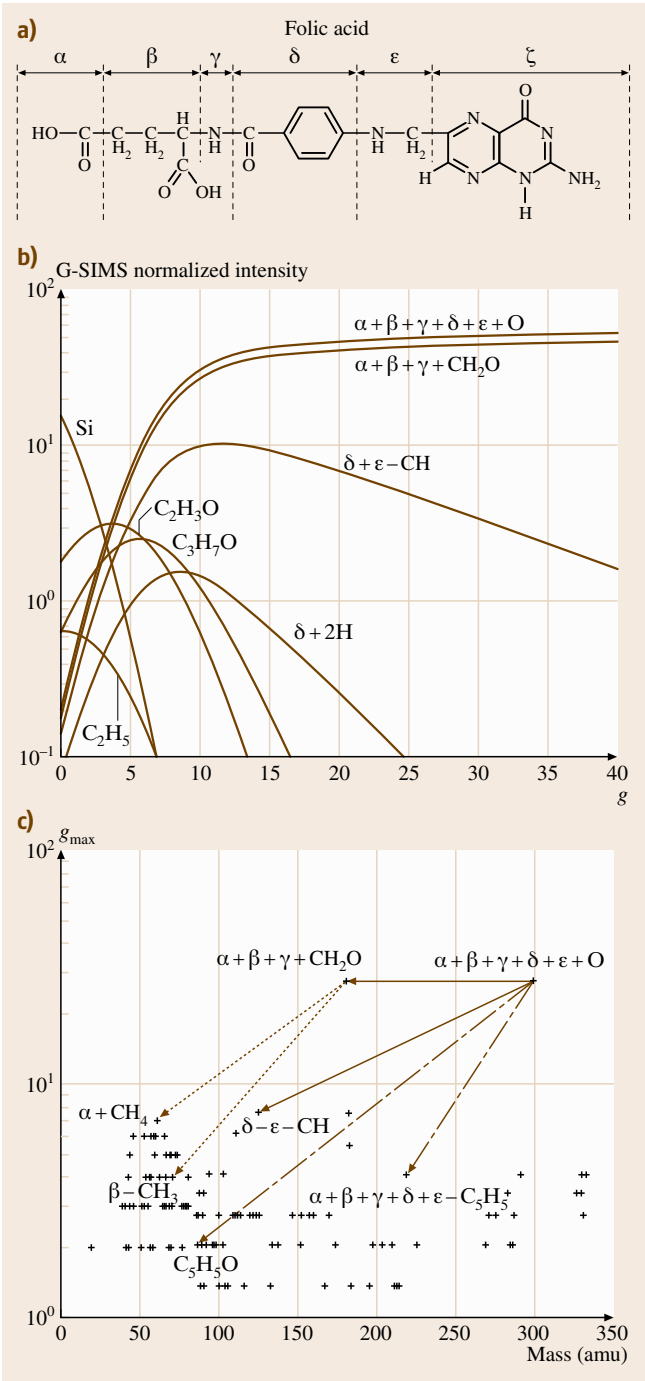

Fig. 6.14a–c G-SIMS-FPM for folic acid: **(a)** the molecular structure of folic acid identifying six subunits, **(b)** the change in relative intensities of G-SIMS peaks with g index showing the peak g values, g_{max}, and **(c)** the reassembly plot showing fragmentation pathways (after *Gilmore* and *Seah* [6.187]) ▶

173] and opens up the method to the life sciences and other areas where the libraries would need to run to hundreds of thousands of spectra. Unfortunately, in the life sciences and similar areas, the molecular weight may not be adequate to identify a molecule and knowledge is required about its structure. An extension of G-SIMS called G-SIMS with fragmentation pathway mapping (G-SIMS-FPM) shows how this may be done [6.187]. By altering the index g in (6.41), we may view spectra that move progressively from the highly fragmented static SIMS ($g = 0$) to the unfragmented G-SIMS with $g = 40$. During this process, we can see higher mass peaks being built up and parts of the molecule being reassembled in the spectra. With accurate mass calibration, the composition of each fragment may be evaluated. Figure 6.14 shows how this works for folic acid. To the left in Fig. 6.14b we see the intensities of certain peaks. As g increases, these either grow or die. Those that grow may peak at a certain g value, g_{max}, and this value is then plotted as the ordinate value in Fig. 6.14c. Molecules or large fragments to the right in Fig. 6.14b or the top in Fig. 6.14c are split into smaller mass fragments, peaking further to the left in Fig. 6.14b or down and to the left in Fig. 6.14c. Unfortunately, not all fragments are emitted as ions and so the plots are not complete, but they do add sufficient dimension to the information to permit identification where the static SIMS or G-SIMS data are insufficient. The use of cluster primary ions is important here for analyzing the larger molecules [6.188].

6.1.4 Conclusions

In Sect. 6.1, we have presented the measurement status of surface chemical analysis. The three main techniques of AES, XPS, and SIMS are all still rapidly developing in both instrumentation and applications. The spatial and spectral resolutions are still improving, and signal levels are increasing. AES, XPS, and dynamic SIMS are all relatively mature with extensive procedural standards available from ISO [6.3, 4] and ASTM [6.2]. This area is also highly active, and both these and research results also feed back into the hardware and software of the commercial instruments. Static SIMS, which has very strong development potential, is being increasingly used in industrial laboratories to obtain levels of detail and sensitivity not available with AES or XPS. The latest generation of time-of-flight (TOF)-

SIMS instruments and their new ion sources make this a very fast developing and fruitful area. New standards in ISO are expected to be developed over the coming years.

6.2 Surface Topography Analysis

The topography of a surface is the set of geometrical details that can be recorded through a measurement. Most commonly, topography is either related to the mechanical nature of the surface, typically involved in contact situations, or to its electromagnetic nature, typically involved in optical effects. Topography is of paramount importance for the functional behavior of a surface, strongly interplaying with material properties and operating conditions.

Surface topography characterization is a powerful tool in connection with design, manufacture, and function. As schematically illustrated in Fig. 6.15, it allows one to link the functional behavior of a surface to the microgeometry obtained from its generation. The three main phases of surface topography characterization are measurement, visualization, and quantification. These phases encompass a number of basic steps, nowadays prevalently involving digital techniques and extensive use of computers: data acquisition, conditioning, visualization, elaboration, and quantification. In particular, quantification typically concerns the geometry of single surface features at micrometer or nanometer scale, being based on the extraction of parameters, curves, functions or basic geometrical features from a representative profile or area on the surface. Quantifying the microgeometries of surfaces after they have been measured is important in all applications of process control, quality control, and design for functionality.

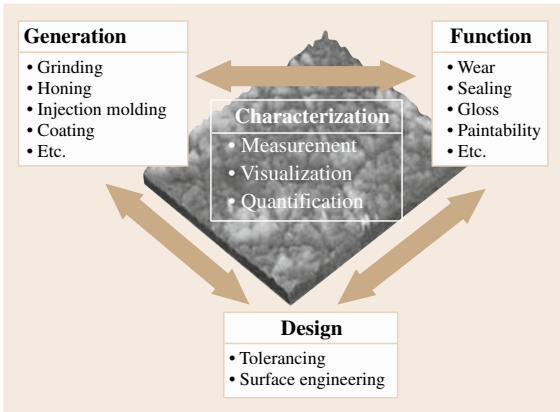

Fig. 6.15 Surface topography characterization links design, generation, and function (after [6.189])

The principal methods of surface topography measurement are stylus profilometry, optical scanning techniques, and scanning probe microscopy (SPM). These methods, based on acquisition of topography data from point-by-point scans, give quantitative information on heights with respect to position. Other methods such as scanning electron microscopy (SEM) can also be used. Based on a different approach, the so-called integral methods produce parameters representing some average property of the surface under examination. A further classification distinguishes between contacting and noncontacting instruments. While stylus instruments are inherently contacting methods and optical instruments noncontacting methods, scanning probe microscopes can be both contacting and noncontacting. We shall describe the basics of each of the methods later, but it is useful to outline the attributes of the methods here so that the reader can focus early on their method of choice.

In a stylus profilometer, the pick-up draws a stylus over the surface at a constant speed, and an electric signal is produced by the transducer. This kind of instrument can produce very accurate measurements in the laboratory as well as in an industrial environment, covering vertical ranges up to several millimeters with resolutions as good as nanometric, with lateral scans of up to hundreds of millimeters being possible. The stylus is typically provided with a diamond tip with a cone angle (total included angle) of 60° or 90° and a tip radius in the range 1–10 μm. The maximum detectable slopes using a stylus instrument are, respectively, 60° or 45°. The spatial resolution achieved by this method, generally in the range 2–20 μm, is limited by the tip geometry, and depends on the actual surface slopes and heights in the neighborhood of the point of contact. Moreover, the force applied by the stylus on the surface can generate plastic deformation on the surface, making this method inapplicable to surfaces that are soft or where even light scratches cannot be accepted.

Optical scanning techniques encompass most typically optical profilometers, confocal microscopes, and interferometers. The optical methods are noncontacting, which allows measurements on soft surfaces. However, this kind of instrument is subject to measurement errors related to achieving a useful reflection signal from surfaces that are shiny or transparent to the light source. Optical styli for profilometry can be based on the autofocusing signal of a laser beam detector. The beam has a spot diameter of about 1 μm, and this kind of instrument is similar in use to conventional stylus instruments, with vertical resolution of approximately 5 nm. The maximum detectable slope using an autofocusing stylus instrument is approximately 15°. Laser scanning confocal microscopy is another optical technique based on the focus detection principle, where one surface picture element (pixel) is imaged at a time. Topography is reconstructed as a stack of vertical optical sections, in a fashion similar to computer tomography. Confocal microscopes allow steep surface details to be assessed, the maximum detectable slope being up to 75°. Confocal microscopes have limited lateral resolution, and some commercially available instruments even have limited vertical resolution. Interference microscopy combines an optical microscope and an interferometer objective into a single instrument. These optical methods allow fast noncontacting measurements on essentially flat surfaces. Interferometric methods offer subnanometer vertical resolution, being employed for surfaces with average roughnesses down to 0.1 nm and peak-to-valley heights up to several millimeters. Interferometric microscopes are all limited with respect to the surface slopes from the finite numerical apertures. Moreover, the lateral resolution is limited by diffraction. The maximum detectable slope using interferometry amounts to about 30°.

Scanning probe microscopy, including atomic force microscopy (AFM) and scanning tunneling microscopy (STM), is based on a powerful class of tools for subnanometric acquisition of topography data on very fine surfaces. SPM uses a sharp probe scanning over the surface while maintaining a very close spacing to the surface. SPM allows measurements on surfaces with an area up to approximately $100 \times 100\,\mu m^2$ and that have local variations in surface height which are less than approximately 10 μm. SPM is a three-dimensional (3-D) microscopy technology in which the resolution is not limited by the diffraction of light. The vertical resolution of SPM is about 0.1 nm, while the horizontal resolution for most AFM devices is typically 2–10 nm, but it can be atomic. SPM requires minimal sample preparation.

Scanning electron microscopy (SEM) can also be used for qualitative surface topography analysis, primarily based on the fact that SEM allows excellent visualization achieved through the very high depth of focus of this technique. However, SEM photographs are still inherently two-dimensional (2-D), and no height information can be extracted directly from the images. The 3-D achieved by reconstructing from stereo pairs or triplets can be used to evaluate surface topography, but it is limited by a number of factors.

Figure 6.16 [6.190] shows a diagram of the spatial resolutions of the different techniques that helps to place the more popularly used methods in context. Additional information is given in Table 6.8. Documentary standards covering surface topography are published by ISO. Updated information regarding the ISO standards for surface texture can be found on the www.iso.org website and by searching in the ISO catalogue under *17.040.20 Properties of surfaces* and *17.040.30 Measuring instruments*. Surface texture is a topic covered by the technical committee TC213 Geometrical Product Specifications under the ISO, the homepage of which can be found through the above-mentioned website. Table 6.9 lists the titles of ISO standards published

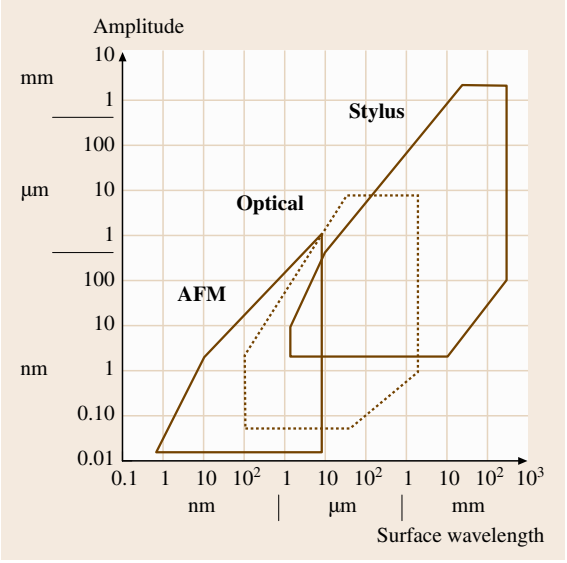

Fig. 6.16 Diagram showing the vertical and horizontal resolution achievable with different instruments for surface topography measurements (after *Stedman* [6.190])

Table 6.8 Resolutions and ranges of some techniques for surface topography analysis

Instrument	Vertical axis		Horizontal axes	
	Resolution (nm)	Range (mm)	Resolution (nm)	Range (mm)
Stylus	< 1	10	2000	> 100
Auto-focus	< 5	1	1000	> 100
WLI	0.1	1	500	< 10
SEM	1	1	2	1
AFM	< 0.1	0.01	1	0.1

WLI – white-light interferometry
SEM – scanning electron microscopy
AFM – atomic force microscopy

in the field of surface texture. Most standards cover 2-D profiling techniques, but also standards for 3-D areal measurements are currently under publication by ISO. Table 6.10 presents a list of ISO standards under development related to surface topography. Essential textbooks covering the area are [6.191–193].

Table 6.9 Published standards from ISO TC213 for surface texture

No.	ISO standard	Title [reference]
1	ISO 1302:2002	Geometrical product specifications (GPS) – Indication of surface texture in technical product documentation [6.194]
2	ISO 3274:1996, (*)	Geometrical product specifications (GPS) – Surface texture: Profile method – Nominal characteristics of contact (stylus) instruments [6.195]
3	ISO 4287:1997, (*)	Geometrical product specifications (GPS) – Surface texture: Profile method – Terms, definitions, and surface texture parameters [6.196]
4	ISO 4287:1997Amd 1:2009, (*)	Peak count number [6.197]
5	ISO 4288:1996, (*)	Geometrical product specifications (GPS) – Surface texture: Profile method – Rules and procedures for the assessment of surface texture [6.198]
6	ISO 5436-1:2000, (*)	Geometrical product specifications (GPS) – Surface texture: Profile method; Measurement standards – Part 1: Material measures [198]
7	ISO 5436-2:2002, (*)	Geometrical product specifications (GPS) – Surface texture: Profile method; Measurement standards – Part 2: Software measurement standards [6.199]
8	ISO 8785:1998	Geometrical product specification (GPS) – Surface imperfections – Terms, definitions, and parameters [6.200]
9	ISO 11562:1996, (*)	Geometrical product specifications (GPS) – Surface texture: Profile method – Metrological characteristics of phase-correct filters [6.201]
10	ISO 12085:1996, (*)	Geometrical product specifications (GPS) – Surface texture: Profile method – Motif parameters [6.202]
11	ISO 12179:2000	Geometrical product specifications (GPS) – Surface texture: Profile method – Calibration of contact (stylus) instruments [6.203]
12	ISO 13565-1:1996, (*)	Geometrical product specifications (GPS) – Surface texture: Profile method; Surfaces having stratified functional properties – Part 1: Filtering and general measurement conditions [6.204]
13	ISO 13565-2:1996, (*)	Geometrical product specifications (GPS) – Surface texture: Profile method; Surfaces having stratified functional properties – Part 2: Height characterization using the linear material ratio curve [6.205]
14	ISO 13565-3:1998	Geometrical product specifications (GPS) – Surface texture: Profile method; Surfaces having stratified functional properties – Part 3: Height characterization using the material probability curve [6.206]
15	ISO/TS 16610-1:2006	Geometrical product specifications (GPS) – Filtration – Part 1: Overview and basic concepts [6.207]
16	ISO/TS 16610-20:2006	Geometrical product specifications (GPS) – Filtration – Part 20: Linear profile filters: Basic concepts [6.208]

Table 6.9 (continued)

No.	ISO standard	Title [reference]
18	ISO/TS 16610-22:2006	Geometrical product specifications (GPS) – Filtration – Part 22: Linear profile filters: Spline filters [6.209]
19	ISO/TS 16610-28:2010	Geometrical product specifications (GPS) – Filtration – Part 28: Profile filters: End effects [6.210]
20	ISO/TS 16610-29:2006	Geometrical product specifications (GPS) – Filtration – Part 29: Linear profile filters: Spline wavelets [6.211]
21	ISO/TS 16610-30:2009	Geometrical product specifications (GPS) – Filtration – Part 30: Robust profile filters: Basic concepts [6.212]
22	ISO/TS 16610-31:2010	Geometrical product specifications (GPS) – Filtration – Part 31: Robust profile filters: Gaussian regression filters [6.213]
23	ISO/TS 16610-32:2009	Geometrical product specifications (GPS) – Filtration – Part 32: Robust profile filters: Spline filters [6.214]
24	ISO/TS 16610-40:2006	Geometrical product specifications (GPS) – Filtration – Part 40: Morphological profile filters: Basic concepts [6.215]
25	ISO/TS 16610-41:2006	Geometrical product specifications (GPS) – Filtration – Part 41: Morphological profile filters: Disk and horizontal line-segment filters [6.216]
26	ISO/TS 16610-49:2006	Geometrical product specifications (GPS) – Filtration – Part 49: Morphological profile filters: Scale space techniques [6.217]
27	ISO 25178-6:2010	Geometrical product specifications (GPS) – Surface texture: Areal – Part 6: Classification of methods for measuring surface texture [6.218]
29	ISO 25178-601:2010	Geometrical product specifications (GPS) – Surface texture: Areal – Part 601: Nominal characteristics of contact (stylus) instruments [6.219]
30	ISO 25178-602:2010	Geometrical product specifications (GPS) – Surface texture: Areal – Part 602: Nominal characteristics of noncontact (confocal chromatic probe) instruments [6.220]
31	ISO 26178-701:2010	Geometrical product specifications (GPS) – Surface texture: Areal – Part 701: Calibration and measurement standards for contact (stylus) instruments [6.221]

Note (*): Standard amended by technical corrigendum. Published corrigenda are: ISO 3274:1996/Cor 1:1998; ISO 4287:1997/Cor 1:1998; ISO 4287:1997/Cor 2:2005; ISO 4288:1996/Cor 1:1998; ISO 5436-2:2001/Cor 1:2006; ISO 5436-2:2001/Cor 2:2008; ISO 11562:1996/Cor 1:1998; ISO 12085:1996/Cor 1:1998; ISO 13565-1:1996/Cor 1:1998; ISO 13565-2:1996/Cor 1:1998

Table 6.10 Standards under development

No.	ISO standard	Title [reference]
1	ISO 1302:2002/DAmd 2	Indication of material ratio requirements [6.222]
2	ISO/DIS 16610-21	Geometrical product specifications (GPS) – Filtration – Part 21: Linear profile filters: Gaussian filters [6.223]
3	ISO/CD 25178-1	Geometrical product specifications (GPS) – Surface texture: Areal – Part 1: Indication of surface texture [6.224]
4	ISO/DIS 25178-2	Geometrical product specifications (GPS) – Surface texture: Areal – Part 2: Terms, definitions, and surface texture parameters [6.225]
5	ISO/DIS 25178-3.2	Geometrical product specifications (GPS) – Surface texture: Areal – Part 3: Specification operators [6.226]
6	ISO/DIS 25178-7	Geometrical product specifications (GPS) – Surface texture: Areal – Part 7: Software measurement standards [6.227]
7	ISO/DIS 25178-603	Geometrical product specifications (GPS) – Surface texture: Areal – Part 603: Nominal characteristics of noncontact (phase-shifting interferometric microscopy) instruments [6.228]
8	ISO/DIS 25178-604	Geometrical product specifications (GPS) – Surface texture: Areal – Part 604: Nominal characteristics of noncontact (coherence scanning interferometry) instruments [6.229]
9	ISO/CD 25178-605	Geometrical product specifications (GPS) – Surface texture: Areal – Part 605: Nominal characteristics of noncontact (point autofocusing) instruments [6.230]

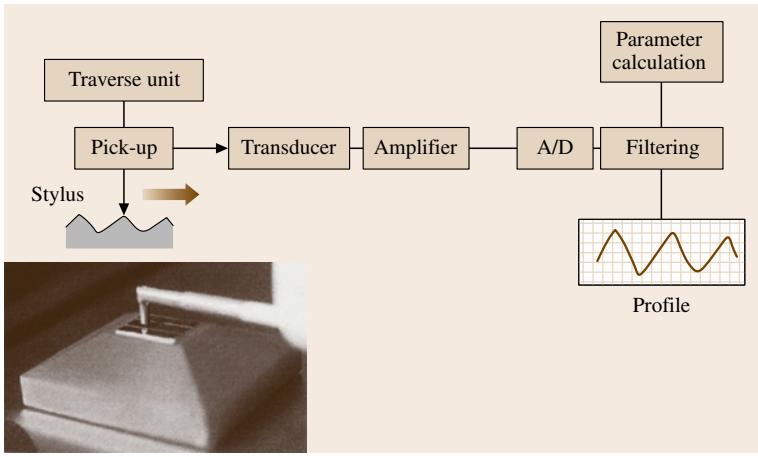

Fig. 6.17 Operational scheme for a stylus profilometer; A/D = analog-to-digital converter

6.2.1 Stylus Profilometry

General Introduction

The most well-known surface profilometer in the manufacturing industry is the stylus instrument used for conventional two-dimensional roughness measurements. This kind of instrument, shown in Fig. 6.17, has existed for over 60 years, and it yields a high degree of accuracy, robustness, and user-friendliness. In a typical surface tester, the pick-up draws the stylus over the surface at a constant speed, and an electrical signal is produced by the transducer, which can be piezoelectric, inductive or laser interferometric. The signal is amplified and digitized for subsequent data processing such as filtering and parameter calculation. In a more comprehensive laboratory stylus system, parallel tracings can be made over the workpiece, allowing reconstruction of a whole surface area, in order to perform so-called three-dimensional surface topography characterization. The versatility of the stylus instrument is underlined by the ability to use this instrument on all kinds of items, irrespective of orientation, and to mount the pick-up on other machines, such as a coordinate measuring machine or a form tester, to achieve measurement of the surface topography over complex workpieces. The stylus is provided with a diamond tip with a total cone angle of 60° or, more commonly, 90°. Standardized values for the tip radius are 2, 5, and 10 µm, but other values are also used. Stylus instruments feature vertical ranges of up to several millimeters, with best resolutions at nanometric level and scans of up to hundreds of millimeters possible. The standardized values for the maximum load corresponding to the above-mentioned radii are 0.7, 4, and 16 mN, respectively. In many cases, a tracing speed of 0.5 mm/s is used.

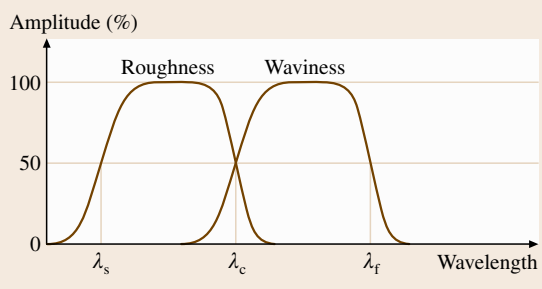

Fig. 6.18 Transmission characteristic of roughness and waviness profiles using ISO filters (after [6.196])

Measurement and Filtering

When tracing a surface profile, a stylus instrument works as schematically shown in Fig. 6.17. Filters are used to separate roughness from waviness and form. ISO operates with three different types of profile that can be extracted from the acquired profile through filtering: primary P-profile, waviness W-profile, and roughness R-profile. Filters are useful in that they permit the user to focus on wavelength components that are important from a functional point of view. Modern filter definitions introduced in ISO standards are based on digital Gaussian cut-off filters characterized by being phase-correct and robust to single features such as scratches. Referring to Fig. 6.18 and [6.196], ISO operates with cut-off filters with nominal wavelengths λ_s, λ_c, and λ_f, where the index "s" refers to sampling, "c" to cut-off, and "f" to form. An ISO filter is characterized by the wavelength at which it transmits 50% of

the amplitude. As illustrated in Fig. 6.18, the three filters λ_s, λ_c, and λ_f delimit the wavelength intervals for the roughness and waviness profiles by creating two filter windows. As an alternative, parameters can be calculated on the basis of the so-called primary profile, which results from eliminating the short-wave components only, by using the λ_s filter (λ_s is used to eliminate high-frequency components along with the mechanical filtering effect from the stylus tip radius). As indicated on the figure, the filters are not sharp but instead produce a progressive damping of the signal.

The data obtained from a measured surface are typically processed as follows.

1. A form fit, such as a least-squares arc or line (best fit), is applied to the data in order to remove the form.
2. The ultrashort-wave components are removed using a λs filter. The result is the primary profile, from which P-parameters can be calculated.
3. The primary profile is passed through a λ_c filter with a specific cut-off value that separates waviness from roughness.
4. The resultant roughness or waviness profile is then processed to calculate the roughness or waviness parameters.

The result of filtering is illustrated in Fig. 6.19. ISO 4287 operates with a number of standardized elements used for parameter calculations: the *mean line*, which is the reference line from which the parameters are calculated, such as the *mean line for the roughness profile*, which is the line corresponding to the longwave profile component suppressed by the profile filter λ_c; the *sampling length* l_P, respectively l_W and l_R, which is the length in the direction of the X-axis used to identify the irregularities characterizing the profile; and the *evaluation length* l_n, generally defined by ISO as five times the sampling length (Pt, Wt, and Rt shown in Fig. 6.19 are calculated over the evaluation length). More advanced methods of filtering are described in the new series of ISO 16610 standards [6.207–217].

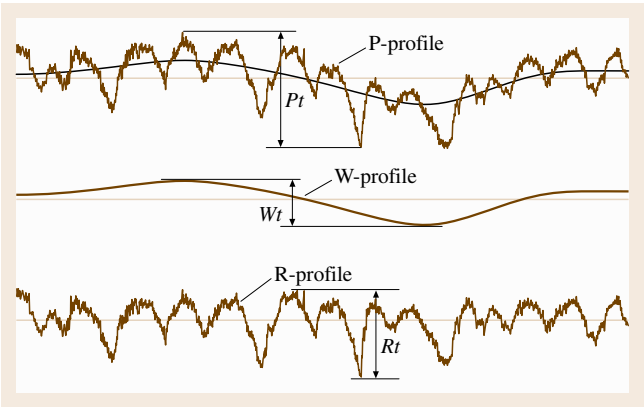

Fig. 6.19 Primary P-profile, waviness W-profile, and roughness R-profile

Visualization

The very first step in surface topography analysis consists of a visualization of the microgeometry, either as single profiles or as surface areas, to provide realistic representations of the surface. The usefulness of such an approach for qualitative characterization is well recognized: often the image inspection, possibly aided by some enhancement techniques, can be assumed as the only aim of the analysis. Indeed, the image conveys a vast amount of information, which can be easily interpreted by an experienced observer; even a single profile contains a large amount of relevant information, and moreover in a condensed way by adopting different scales for the horizontal and vertical axes. The passage from profile two-dimensional analysis to surface three-dimensional analysis enlarges the possibilities for gaining knowledge and representing the surface texture. Many techniques have been developed to display the sampled data, with the possibility of enhancing some particular features, such as

- contour plots, color plots, and grayscale mapping, techniques borrowed from soil cartography to represent the surface heights,
- isometric and dimetric (as in Fig. 6.15) projections, where the single data points are interconnected with all the neighboring points by straight or curved lines. Projections can be modified by the scales and projection angles, for enhancement of amplitudes, texture, etc.,
- inversion and truncation techniques, whereby the visual interpretation of the projections is enhanced through data manipulation. Other manipulation techniques are used, for example, to emphasize surface slopes.

Quantification of Surface Texture

Quantitative assessment of surface texture can be very useful in relation to process control, tolerance verification, and functional analysis. Nevertheless, it must be undertaken with care, since interpretation of mere parameters can lead to wrong conclusions. Unless the

topographic nature of the surface under consideration is known, it is strongly recommended that quantitative characterization should only be used in connection with a visual examination of the surface topography, as described above.

2-D Parameters Covered by ISO Standards. Conventional roughness parameters, which are those most commonly known to quantify surface texture, are often referred to as 2-D parameters, since they are computed on the basis of single profiles containing information in two dimensions (horizontal and vertical). The 2-D surface texture area has been totally revised by ISO, with the introduction of several new international standards [6.189, 194, 195, 198–206, 231]. According to current ISO terminology, as mentioned in connection with filters, the concept of surface texture encompasses roughness, waviness, and the primary profile. In the following, an overview is presented of the existing ISO parameters for surface texture. Only ISO parameters are considered here, since they adequately cover what can be quantified through 2-D parameters. A more complete review of parameters can be found in the monographs [6.187–189]. Conventional 2-D parameters are described in the current ISO standard ISO 4287 [6.197], while other 2-D parameters are covered by ISO 12085 [6.202] and ISO 13565 [6.204–206]. ISO 1302 [6.194] prescribes a detailed indication of surface texture tolerances on technical drawings, with indication of the measurement specifications to follow when verifying tolerances.

Conventional 2-D Parameters. ISO 4287 defines three series of 14 parameters each: P-parameters for the unfiltered profile, R-parameters for the roughness profile, and W-parameters for the waviness profile; see Table 6.11 and [6.197]. Filtering to obtain the R and W profiles is introduced in the same standard and specified in [6.201]. Only examples of some parameters are given in this section. The reader should refer to the standard for complete definitions of each parameter. Conventional 2-D surface texture parameters are defined in ISO 4287, but their value ranges are addressed in ISO 4288 [6.198]. ISO 4288 uses five sampling lengths as default for roughness profile parameters, indicating how to recalculate their upper and lower limits based on other numbers of sampling lengths. It should be noted that the same terminology is used in ISO 4287 and ISO 4288 to indicate the parameters computed over one sampling length and over five sampling lengths, respectively. It should be also noted that wavelengths under 13 µm and amplitudes of less than 25 nm are not covered by existing ISO standards, which therefore disregard typical ranges of interest in usual AFM metrology. However, since the ranges of definition seem to be dictated by the physical possibilities of existing stylus instruments, it can be assumed that the definitions can also be extended to values below those, but this must be investigated.

- *Ra* is the most widely used quantification parameter in surface texture measurement. It has also been known in the past as the center line average (CLA) or, in the USA, as the arithmetic average (AA). *Ra* is the arithmetic average value of the profile departure from the mean line within a sampling length, which can be defined as

$$Ra = \frac{1}{L}\int_0^L |z(x)|\,\mathrm{d}x \approx \frac{1}{n}\sum_{i=1}^{n}|z_i| \,. \qquad (6.42)$$

  Here, z is the height from the mean line defined in Fig. 6.19.
- *Rq*, corresponding to the root mean square (RMS), is preferred to *Ra* for modeling purposes. *Rq* is the geometric average value of the profile departure from the mean line within a sampling length, which can be defined as

$$Rq = \sqrt{\frac{1}{L}\int_0^L [z(x)]^2\,\mathrm{d}x} \approx \sqrt{\frac{1}{n}\sum_{i=1}^{n}(z_i)^2} \,. \qquad (6.43)$$

Table 6.11 Profile parameters defined by ISO 4287 (1997)

	Amplitude parameters									Distance parameters	Hybrid parameters	Curves and related parameters		
	Top–valley					Mean value								
Roughness parameters	*Rp*	*Rv*	*Rz*	*Rc*	*Rt*	*Ra*	*Rq*	*Rsk*	*Rku*	*RSm*	*RΔq*	*Rmr(c)*	*Rδc*	*Rmr*
Waviness parameters	*Wp*	*Wv*	*Wz*	*Wc*	*Wt*	*Wa*	*Wq*	*Wsk*	*Wku*	*WSm*	*WΔq*	*Wmr(c)*	*Wδc*	*Wmr*
Structure parameters	*Pp*	*Pv*	*Pz*	*Pc*	*Pt*	*Pa*	*Pq*	*Psk*	*Pku*	*PSm*	*PΔq*	*Pmr(c)*	*Pδc*	*Pmr*

- Rp is the maximum height of the profile above the mean line within a sampling length.
- Rv is the maximum depth of the profile below the mean line within a sampling length.
- Rz is the maximum peak-to-valley height of the profile within the sampling length.
- Rt is a parameter which basically has the same definition as Rz but the definition of which is based on the total assessment, or evaluation, length (l_n). The evaluation length covers by default five sampling lengths, see ISO 4288 [6.198].
- RSm (mean spacing) is the mean width of the profile elements at the mean line within the sampling length.

Other Parameters Defined by ISO. Other parameters defined by ISO standards are the motif parameters and the bearing curve parameters. ISO 12085 [6.202] concerns parameters calculated through profile evaluation using the motif method, so far only used by the French motor industry. The method is based on dividing the unfiltered profile into geometrical features, characterized by peaks, that may merge or remain unaltered depending on their relative magnitudes, and thus calculating a number of roughness and waviness parameters. It should be noted that waviness and roughness in ISO 12085 do not refer to the same definitions used for the conventional parameters defined in ISO 4887. ISO 13565 describes two sets of parameters extracted from the bearing curve, and was specifically developed to characterize stratified surfaces with different functional properties at different depths. ISO 13565-1 [6.204] describes filtering. Parameters developed by the German motor industry are defined in ISO 13565-2 (Fig. 6.20 and [6.178]), while ISO 13565-3 describes the parameter set developed by the US engine manufacturer Cummins [6.195,198,199,201,203,206,231,232].

3-D Parameters. Parameters calculated over an area are referred to as areal, or 3-D, parameters. Currently, 3-D surface texture measurement is the object of a number of ISO standards currently under development. Based on the research carried out within the European Program [6.233], a set of 3-D parameters has been proposed [6.234, 235]. These parameters are denoted by S instead of R to indicate that they are calculated over a surface. Table 6.12 gives an overview of the so-called field parameters currently under consideration by ISO. Most of the parameters of the set are derived from the corresponding 2-D parameters, while three are uniquely devised for surfaces. For example, the parameters Sa and Sq are calculated using equations similar to, respectively, (6.42) and (6.43). The reader should refer to the ISO documents or to the above-mentioned research reports for complete definitions of each parameter. Note that in ISO 25178 [6.236] conventional profilometry is referred to as line-profiling methods, while 3-D surface characterization is called areal-topography methods.

Table 6.12 3-D Parameters by ISO – Field parameters

Height parameters	Arithmetical mean height Sa (μm)
	Root-mean-square height of the scale-limited surface Sq (μm)
	Skewness of the scale-limited surface Ssk
	Kurtosis of the scale-limited surface Sku
	Maximum peak height Sp (μm)
	Maximum pit height Sv (μm)
	Maximum height of the scale-limited surface Sz (μm)
Spatial parameters	Autocorrelation length Sal (μm)
	Texture aspect ratio Str
Hybrid parameters	Root-mean-square gradient of the scale-limited surface Sdq
	Developed interfacial area ratio of the scale-limited surface Sdr
Other parameters	Texture direction of the scale-limited surface Std (deg)

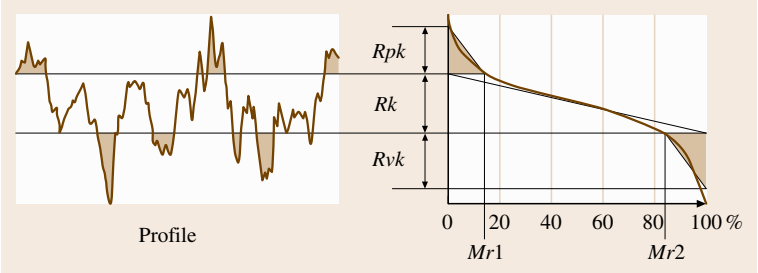

Fig. 6.20 Definition of bearing curve parameters according to ISO 13565-2:1996 (after [6.205]). Vertically, the *bearing curve* is divided into three zones, each described by a parameter: Rpk (peaks), Rk (core), and Rvk (valleys). Horizontally, two parameters are defined: $Mr1$ and $Mr2$ (material portions)

6.2.2 Optical Techniques

Many different measuring instruments based on optical techniques exist [6.191, 193, 237, 238]. In this section, the three most important ones are described: optical stylus profilometry, confocal microscopy, and interferometry. Some issues are of importance to all optical microscopy methods [6.239].

- Material response: optical probing is only possible when a signal above the detector threshold is received, which is determined by the material's reflectivity.
- Lateral resolution: this is limited by light diffraction. For an instrument numerical aperture NA and a light wavelength λ, the limit d is given by [6.196]

$$d = \frac{1.22\lambda}{\mathrm{NA}} \,. \tag{6.44}$$

- Maximum detectable slope: this depends on the kind of reflection (specular or diffused), which in turn depends on the surface topography and material, as well as on the objective working distance and numerical aperture.
- Wavelength of full-amplitude modulation: this quantity is intended as the maximum aspect ratio of a measurable surface structure.

Optical Stylus Profilometry

Optical styli for profilometry can be based on the autofocusing signal of a laser beam detector. A laser beam with a spot diameter of about 1 μm is focused onto a point on the surface through a lens characterized by a high numerical aperture (NA). The scattered light is collected by the same lens on a focus detector, which operates a control system. When the detector moves horizontally, the controller, normally piezoelectric, modifies the distance of the lens from the surface so as to keep the beam focused. Consequently, the movement of the lens follows the surface at a constant separation distance, and its trajectory describes the surface profile, as shown in Fig. 6.21. This kind of instrument is similar in use to conventional stylus instruments, with vertical resolution of approximately 5 nm. The optical method is noncontacting, which allows measurements on soft surfaces. However, this kind of instrument is connected to some problems related to achieving a useful reflection signal from surfaces that are shiny or transparent to the laser beam. The measurements obtained with the autofocusing method do not always correlate very well with those obtained with the stylus method [6.235,237], as the optical method tends to overestimate the peak heights and the stylus method to underestimate the valley heights of the surface. The optical stylus method was found to work well on very flat samples, but when measuring roughnesses below 1 μs it was very prone to error. The maximum detectable slope using an autofocusing stylus instrument is approximately 15°.

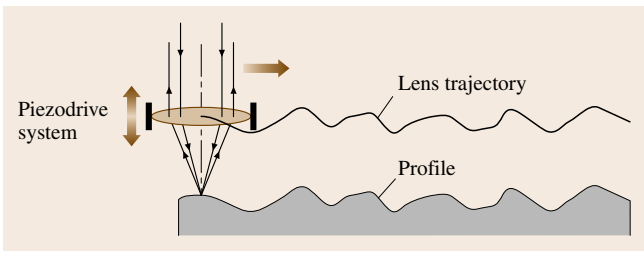

Fig. 6.21 Operating principle of the autofocusing method (after [6.237])

Confocal Microscopy

Confocal microscopy is an optical technique based on the focus detection principle. It is routinely applied in biological sciences, where relatively thick biological samples, such as cells in tissue, are investigated using fluorescence. However, it is also suitable for 3-D topography assessment, when the reflected light is detected rather than the emitted fluorescence. Here, the technique is presented with reference to the reflection mode of operation with a laser light source. The working principle is easily seen by referring to Fig. 6.22, where key components and optical ray diagrams are sketched (the scanner which moves the laser spot on the surface is not shown) [6.239].

Confocality consists in that both the light source pinhole P1 and the detector pinhole P2 are focused on the specimen. In laser scanning confocal microscopy one surface picture element (pixel) is imaged at a time. The final image is therefore built up sequentially. This has relevant consequences for the application of this technique to topography measurement; the measurement time is negatively affected while the maximum detectable surface slope is increased. Topography is reconstructed as a stack of vertical optical sections, in a fashion similar to computer tomography. In other words, it is built by overlapping a number of optical slices with normal vectors aligned with the optical axis. A single optical slice contribution to the final topography is given by all of the pixels where reflection occurs. The two pinholes shown in Fig. 6.22 allow, in principle, the detection of light back from

the focal plane. Stray light should be stopped here and should not reach the detector. This would be strictly true for an infinitesimally small pinhole, but the finite size always allows some amount of out-of-plane light to be collected by the photodetector. The pinhole diameter can be adjusted by the operator; practical values for the diameter in reflection-mode confocal microscopy go down to the diffraction limit given by (6.44). As a consequence, optical slices have a finite thickness. As regards the designs of confocal microscopes, some systems are provided with monochromatic (laser) illumination; others are based on xenon lamps which emit white light. The latter source allows detection by means of a charge-coupled device (CCD) sensor, with no scan being required in the lateral plane. As concerns laser scanners, galvanometric scanning mirrors are used to move the laser spot laterally, without physical table motion. The drive of the vertical axis determines the vertical resolution. With a piezo actuator, ranges of a few hundred microns are possible with resolution of a few nanometers. When a direct-current (DC) motor drives the objective, a range of up to 100 mm can be covered with resolution of about 100 nm. Confocal microscopes allow steep surface details to be assessed, the maximum detectable slope being up to 75°. Confocal microscopes have limited lateral resolution, and some commercially available instruments even have limited vertical resolution [6.239].

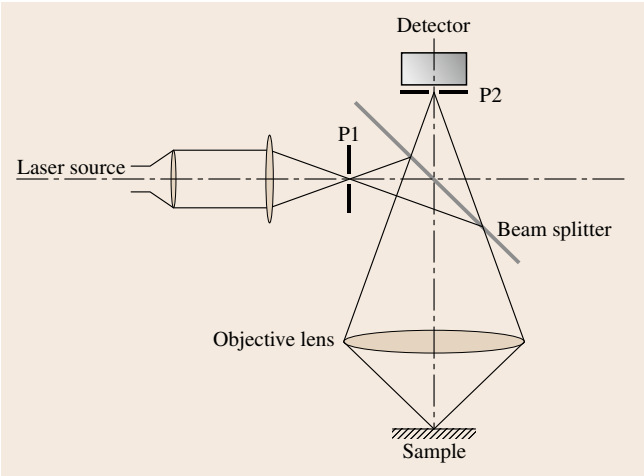

Fig. 6.22 Confocal principle

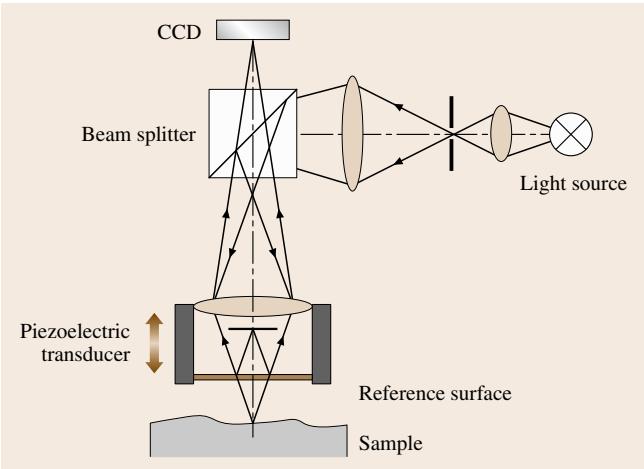

Fig. 6.23 Optical layout of an interferometric measuring system (after [6.237])

Interference Microscopy

Interference microscopy combines an optical microscope and an interferometer objective into a single instrument. Interferometric methods offer subnanometer vertical resolution, and are employed for surfaces with average roughnesses down to 0.1 nm and peak-to-valley heights of up to several millimeters.

Interferometry is a well-known optical principle that is widely used in metrology, which has recently also been applied to surface metrology [6.237]. Basically, interferometric systems are derived from the Fizeau interference microscope, as shown in Fig. 6.23. A light beam is sent through a microscope objective onto the sample surface. A part of the incident beam is reflected back by a semitransparent reference surface. The beams coming from the sample surface and the reference surface are projected onto the CCD detector, where they interfere. A piezoelectric transducer moves the objective and the interferometer vertically, causing fringe modulation. The intensity at each point of the interference pattern is proportional to

$$I(x, y) = \cos[\varphi(x, y) + \alpha(t)] \,, \tag{6.45}$$

where $\varphi(x, y)$ is the initial phase and $\alpha(t)$ is the time-varying phase. The initial phase at each point is calculated from the fringe modulation, and the corresponding height is obtained using

$$z(x, y) = \frac{\varphi(x, y)\lambda}{4\pi} \,, \tag{6.46}$$

where λ is the wavelength of the light source. Two main interferometric techniques are commonly used in connection with surface measurements [6.239]

- phase-shift interferometry (PSI),
- scanning white-light interferometry (SWLI).

In PSI, the illumination is from a monochromatic light source (laser interferometry); this technique is characterized by the highest resolving power, while the dynamic range (maximum detectable depth difference between two neighboring pixels) is limited to $\lambda/4$, typically about 150 nm. A clear interference pattern can only be observed on smooth surfaces, while the interference fringes are corrupted by speckle effects when the roughness is larger than $\lambda/4$.

SWLI can be regarded as an extension of the PSI method, where a broadband frequency (instead of a single frequency) contributes to topography measurement. With white light, the dynamic range is no longer limited to $\lambda/4$. This is explained, referring to the frequency-domain analysis technique (FDA), by the fact that an interval of wavelengths, rather than a single one, is used to evaluate the slope. FDA implementation in SWLI is based on the discrete Fourier transform (DFT).

PSI is used mainly for testing optical components and silicon wafers with high accuracy and short measuring times (below 1 s), while most technical surfaces can be inspected by SWLI. Regardless of the category, the lateral resolution is always worse than 0.3 µm, due to the diffraction limit stated in (6.44). These microscopes are all limited with respect to the surface slopes from the finite numerical apertures. The maximum detectable slope using interferometry amounts to about 30°. These optical methods allow fast noncontacting measurements on essentially flat surfaces.

6.2.3 Scanning Probe Microscopy

General Introduction

Scanning probe microscopy, including atomic force microscopy (AFM) and scanning tunneling microscopy (STM), provides a powerful tool for subnanometric acquisition of topographical data on very fine surfaces. Since the invention in 1986 of the scanning tunneling microscope [6.240], SPM and especially AFM have developed very rapidly, from scientific instruments used for basic research to their use in quality control in manufacturing [6.191, 241].

Measurement and Data Processing

In an SPM, as illustrated in Fig. 6.24a, a sharp tip with a radius of approximately 5–20 nm (the original contact-mode tip and cantilever are made out of silicon nitride using photolithography and preferential etching) is scanned over the surface by an *xyz* actuator with resolution of much less than a nanometer and a dynamic range on the order of 10 µm in the *z*-direction and up to 100 µm in the *x*- and *y*-directions. Alternatively, as shown in Fig. 6.24b, the tip is stationary while the sample is moved. The probe records a control signal; in the atomic force microscope this signal is the nondestructive force exerted by the surface on the tip; in the scanning tunneling microscope the control signal is a small current flowing from the tip into the sample. The tip is moved relative to the surface, raster-scanning over a number of nominally parallel lines; in the AFM the height of the probe as a function of the *x* and *y* position is recorded as an image and the topography of the surface is built up into a three-dimensional image. The tip is mounted on a very soft cantilever with spring constant *k* in the range of 1 N/m – so soft that the scanning probe will not move the atoms around on the surface. At the start of a measurement, the cantilever is positioned towards the sample. When the tip touches the sample, the cantilever begins to bend proportionally to the force exerted by the tip on the surface. The tip, ideally terminated by a single atom, traces the contours of the surface and is actually touching the sample surface with a very low force – so low that the atomic structures

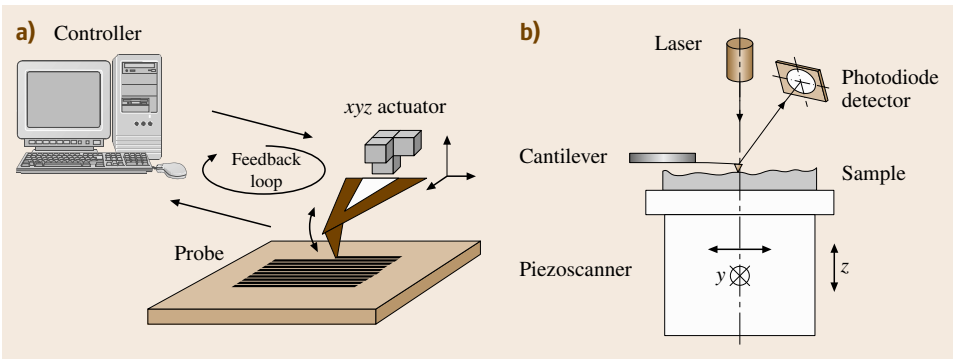

Fig. 6.24a,b Principle of a SPM: **(a)** raster-scanning the tip over a surface, **(b)** optical force detection with the sample scanned in an AFM

are unaltered – both on the sample as well as on the tip. The low force between the tip and sample is kept at a constant level during scanning, being typically lower than 10 nN in contact-mode atomic force microscopy. The most accurate and commonly used principle of detection of the cantilever deflection is optical: a focused laser beam, typically from a laser diode, is reflected from the back of the cantilever towards a photodiode with two or four segments, as illustrated in Fig. 6.24b. When the cantilever is bent, the laser spot at the photodiode will move; in other words, the relative intensity of light hitting the segments will change and produce a signal.

AFM Operation Modes

Different modes of AFM operation exist. The simplest mode of operation for an atomic force microscope is the contact mode, where the probing tip senses the small repulsive force occurring from constantly touching the sample surface. The signal from the detector is used to vertically adjust the tip position with respect to the sample surface, so as to eliminate the deflection of the cantilever. For most applications, resonant vibrating cantilever modes are preferred, although they are more complicated to understand. In the noncontact mode, the cantilever is forced to vibrate a little *above* its resonant frequency. When the vibrating tip comes so close to the surface that it begins to feel the attractive van der Waals forces, the amplitude of the vibration will become smaller. It is this (decreased) amplitude which is kept constant during scanning in noncontact mode. In intermittent contact mode, the cantilever is forced to vibrate a little *below* its resonant frequency, far away from the sample surface. When the vibrating tip comes so close to the surface that it begins to touch the sample surface during a fraction of the vibration cycle, the amplitude of the vibration, as in noncontact mode, becomes smaller relatively to the free amplitude. It is this (decreased) amplitude that is kept constant during scanning in the intermittent mode. Figure 6.25 summarizes the different modes of operation discussed above.

The atomic force microscope can be operated in several other modes than those described above, for example with the purpose of, at least qualitatively, differentiating material properties. During scanning, the tip can tilt, caused by friction between tip and sample surface. The tip also suffers from friction when it passes a ridge and, unfortunately, the friction and topography signal often become mixed. It is possible to give the tip a permanent charge that makes it sensitive to charged areas on the sample when it scans over the surface without touching it. It is also possible to have the tip covered with a permanent magnetic material. If the sample has domains with different magnetic magnitudes, the tip can detect that. In a force modulation microscope, the tip is scanned in contact with the sample and the cantilever, or sample, is forced to swing periodically by a constant control signal. The actual amplitude of the cantilever changes according to the elastic properties of the sample. Atomic force microscopy can be performed in many environments, including ultrahigh vacuum, ambient conditions, and liquids. If the atomic force microscope works in ultrahigh vacuum, it can resolve not only single atoms but also single atom defects on, say, the surface of silicon. Working in air, AFM can only resolve the unit cell structure. It is yet to be been demonstrated that it can resolve single atom defects when working in ambient air.

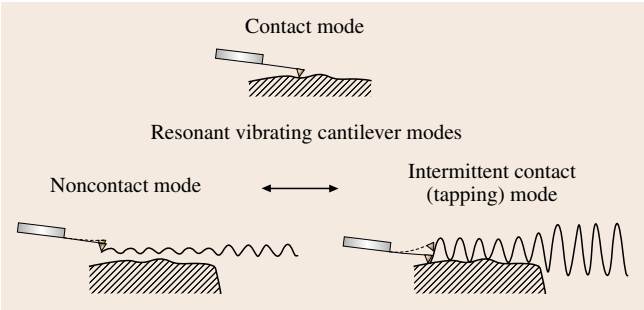

Fig. 6.25 Different operating modes of an AFM

AFM Scanners

In many commercial microscopes, the movement of the tip is performed by a scanner tube, which is a hollow cylinder made out of a piezoelectric material that will change its linear dimensions when subjected to an electric field, and wag in the x–y-plane like a dog's tail. By raising the voltage on the inner electrode, or by mounting a separate piezo element on top of the tube, one can generate movement in the z-direction. This construction has the advantage of being simple and rigid, since all three movements are performed by the same elements. The disadvantage is that the movement is not very accurate. Piezo materials have a number of undesirable properties. First of all, they are intrinsically nonlinear, and what is worse, piezoelectric materials also suffer from hysteresis. Another problem is creep, which means that, when a voltage is applied, the extension or contraction of the piezo material will not reach its final state instantly. Another problem when generating the movement is the coupling between the x- and

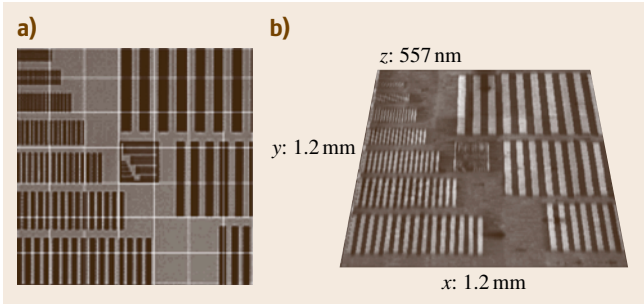

Fig. 6.26 **(a)** Scanning strategy; **(b)** 3-D plot of AFM image composed of 49 single scans stitched together (after [6.239])

the y-motion. Generally speaking, whenever the tip or the sample is moving in one direction, it will unintentionally also move a little bit in other directions. This is particularly bad for movement in the x-direction, since the associated small movement in the z-direction will make a flat surface look curved [6.231]. For smooth surfaces, this curvature can easily dominate the roughness. Over a side length of 100 µm, the peak-to-peak values for the image bow range from a few nanometers for high-quality flexure stages to more than 100 nm for some commonly used tube scanners. Part of the nonlinearity and the hysteresis can be corrected off-line by image processing software. In the x- and y-directions, correction methods can lead to an accuracy of 1–2% under optimum conditions. For the z-direction, unfortunately, it is very difficult – if not impossible – to make a model correction, because the history is generally not known. Using the most linear piezo material, which means trading away some scan range in the z-direction, an accuracy that reaches down to 1% can also be achieved in this direction. The way to overcome the nonlinearity of the piezo material is to use linear distance sensors that independently measure the movement of either the sample or the tip, as used in so-called metrology AFMs.

Large-Range AFM

An AFM allows measurement of the surface topography with very high resolution, but over a limited range. In a specially made instrument, an AFM probe is mounted on a coordinate-measuring machine (CMM), achieving free positioning of the AFM in the space covered by the CMM [6.242, 243]. In particular, this integrated system can be used for surface mapping [6.242–247]. The CMM is used to reposition the AFM probe in-between surface roughness measurements to stitch together different areas covering continuous regions larger than the range scanned by the probe. Correct stitching independently of the positioning errors of the CMM is obtained though optimization of the cross-correlation between two adjacent overlapping surface areas. A maximum uncertainty of 0.8% was achieved for the case of surface mapping of $1.2 \times 1.2\,\text{mm}^2$, consisting of 49 single AFM images, as shown in Fig. 6.26 [6.239]. Another example of large-range AFM, developed by Physikalisch-Technische Bundesanstalt (PTB), is described in [6.248].

6.2.4 Scanning Electron Microscopy

Scanning electron microscopy (SEM) can be used for qualitative surface topography analysis, primarily based on the fact that SEM allows excellent visualization. As regards topography, SEM has some unique properties that, combined together, are not matched by any other microscopy technique. These are listed below [6.239].

- Possible magnification levels from less than 100× up to 100 000×. This means that the imaged range can either be on the order of 1 mm^2 or just 1 μm^2. SEM is in fact a multiscalar technique. There is no other microscopy method as flexible as SEM in terms of the range of scalability.
- At high magnification, the ultimate resolution is as good as about 2 nm on conductive surfaces. SEM metrology is not limited by light diffraction. Such high resolving power can only be achieved by scanning probe microscopes that, on the other hand, are limited in terms of measurable range.
- Large depth of field. In a SEM, features lying at different depths can be kept simultaneously in focus.
- Long usable working distance. High-magnification images, say at 1000× or more, can easily be taken with working distances of several millimeters (ten or even more). This feature allows the development of measuring strategies based on multiple positioning. Moreover, commercially available SEMs are provided with moveable sample stages, with some degrees of freedom for observing features from different viewpoints.

Although SEM images obtained by detecting secondary electrons have a striking three-dimensional appearance (due to the shadowing effects), they are still inherently 2-D. No height information can be extracted directly from the images, and measurements in the x- and y-dimensions are only correct in a single plane. In order to reconstruct the third dimension of surface features,

photogrammetry methods can be used [6.249–255]. A specimen is imaged in the SEM under two different perspectives. Surface features of different heights on the specimen surface differ in their lateral displacement in the two images. The disparities between projections of the surface features in the two images are used to derive quantitative surface topography. A fundamental prerequisite for successful calculation is the correct matching of single surface features in the two images. In most SEMs, it is possible to take the two different stereo viewpoints by tilting the specimen about a horizontal axis.

Three-dimensional data achieved by reconstructing stereo pairs or triplets can be used to evaluate surface topography, but they are limited by a number of factors. First of all, SEM measurements require conductive sample materials, or sample preparation through deposition of a gold layer on the surface. A major limitation is that roughness parameters should be calculated over a relatively large area, while, in the case of large magnifications, the area is relatively small. Another limitation is that smooth surfaces are reconstructed with high uncertainty [6.239].

An investigation was carried out at Danmarks Tekniske Universitet (DTU) on the traceability of surface texture measurements using stereo-pair SEM. A positioning procedure that realizes pseudo-eucentric tilting was developed. A model for calculating the accuracy of topography calculation was given, based on an existing theory adapted to comply with the hypothesis of eucentric tilting [6.256, 257]. A novel design for a calibration artefact, suited for testing the performance of a three-dimensional SEM at high magnifications, was proposed [6.239].

6.2.5 Parametric Methods

Besides the above methods, which produce height scans over the surface, a number of techniques exist that produce measurable parameters representing some averaged property of the surface topography. All of the phenomena related to the interaction between a light wave and a surface are affected by the microgeometry of the surface, and methods based upon specular or diffuse reflectance, speckle, and polarization have been developed. A review by *Vorburger* and *Teague* [6.258] discusses these techniques, considering potentialities and limits. The so-called integral methods, by which surface roughness is measured and quantified as a whole, operate with parameters based on surface statistics, correlation, and frequency analysis. The main

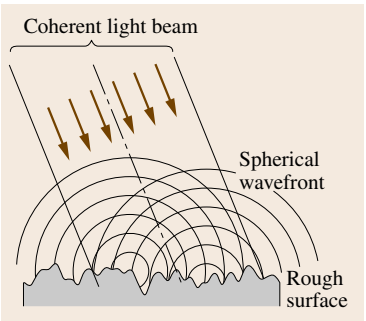

Fig. 6.27 The Huygens–Fresnel principle as the basis of light scattering from rough surfaces (after [6.218])

advantage of statistical surface description is that it describes a profile or surface with a minimum number of parameters, which enables a characterization of the profile or surface [6.259]. The statistical analysis of surface topography leads to a broad variety of parameters, which are not covered by ISO standards in general. In addition to pure statistical properties, further information can be obtained from autocorrelation and autocovariance functions of a given surface $h(x)$ (ACF and ACVF), which are identical for functions with zero mean, as well as from the power spectral density function (PSDF). These are described mathematically in (6.47) and (6.48). A simplified theoretical treatment of light scattering from rough surfaces is based on the Huygens–Fresnel principle, as shown in Fig. 6.27. Here, it may be helpful to emphasize that, irrespective of the method, data cannot be influenced by any property of the sample that is outside the sensing regime of the measuring instrument as defined in the Stedman diagram of Fig. 6.2. Thus, the data from instruments may not agree, even if they are fully calibrated according to the best procedures.

$$\mathrm{PSDF}(k_x) = L^{-1}\left|\int_0^L h(x)\exp(-\mathrm{i}k_x x)\,\mathrm{d}x\right|^2 , \quad (6.47)$$

$$\begin{aligned}\mathrm{ACF}(\tau) &= L^{-1}\int_0^L h(x)h(x+\tau)\,\mathrm{d}x \\ &= \frac{1}{2\pi}\int_{-\infty}^{\infty}\mathrm{PSDF}(k_x)\exp(\mathrm{i}k_x\tau)\,\mathrm{d}k_x\,.\end{aligned} \quad (6.48)$$

Parametric methods based on capacitive and other methods exist as well, but are not relevant to the present chapter. Parametric methods are called area-integrating methods in ISO 25178 [6.128].

6.2.6 Applications and Limitations of Surface Measurement

Visualization of the surface profile, or surface area, is perhaps the most powerful tool associated with topographic surface analysis. Significant information can be drawn directly from the plots, especially when investigating surface functionality. When quantitative information is required, the adoption of parameters becomes essential; for instance, peaks are important when considering friction and wear properties, as the interaction between surfaces concentrates around them. Valleys are important for the retention of lubrication. At the same time, fracture propagation and corrosion start in valleys. The *Rz* parameter can be useful where components are subjected to high stresses; any large peak-to-valley value could be associated with areas which are likely to suffer from crack propagation. For both qualitative as well as for quantitative characterization, 3-D analysis is a powerful tool which can give much more information compared with conventional 2-D methods. In [6.260], a method for identifying different wear mechanisms by measuring surface texture alterations was proposed and applied to deep drawing dies. Using a combination of the areal bearing curve parameters *Spk* and *Svk*, adhesive, abrasive, and fatigue wear as well as plowing and pick-up could be recognized. An important application of areal analysis concerns the quantification of 3-D features such as dominant texture direction, shape of contact asperities, lubricant reservoirs, and valley connectability.

It cannot be emphasized strongly enough that single parameters, which are inherently synthetic, cannot completely describe the complex reality of a surface. Each parameter can only give information about some specific features of the microgeometrical texture, and this requires a sound interpretation. For example, the *Ra* parameter on its own does not tell us anything about the functional behavior of a component, and many existing surfaces can be characterized by the same values of *Ra* but are extremely different with respect to functionality, as clearly illustrated by Fig. 6.28. *Ra* can be used as a process control parameter, since changes in *Ra* value may indicate that some process conditions have changed, such as cutting tool geometry, cutting speed, feed or cutting fluid action. However, being an average value, *Ra* cannot be used to control processes involving stratified surfaces, such as plateau honing. As a general rule, it is strongly recommended that parameters should only be used in connection with a visual examination of the surface topography. An example of extracting comprehensive information using commercial software (SPIP [6.218]) in connection with surface topography analysis is shown in Fig. 6.29.

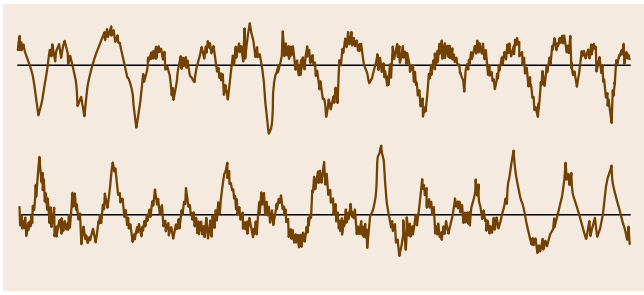

Fig. 6.28 Two profiles with the same R_a (and R_z) value but with very different functional behaviors

Other limitations are related to error sources from the measurement; for instance, roughness parameters can be subject to large variations arising from their definitions and can also be unstable due to spurious features such as dust, burrs or scratches. A metrological limitation in stylus profilometry is that the geometry of the tip acts like a mechanical filter that cannot reproduce smaller details. The resolution achieved by the stylus method depends on the actual surface slopes and heights in the neighborhood of the point of contact, as illustrated in Fig. 6.16. Some parameters describing the shape of the surface are directly influenced by the geometry of the stylus; for example, the tip radius *R* is added to the radii of peaks and subtracted from the radii of valleys. Moreover, the force applied by the stylus on the surface can generate plastic deformation of the surface and affect the measurement. Also, in AFM there are limitations on resolution imposed by the geometry of the probing tip and error sources related to instrument and measuring conditions. No existing instrument can be regarded as truly 3-D: stylus instruments, SPMs, and optical instruments can be considered, at most, as $2\frac{1}{2}$ dimensional. More typically, the vertical range is limited to about one-tenth of the lateral ones. No commercially available instrument is suitable for measuring deep cavities, pores or reentrances, not to mention hidden details. The need for true 3-D characterization of surface details has been addressed in [6.261].

6.2.7 Traceability

Traceability is defined as the property resulting from measuring to the value of a standard whereby it can be related to stated references, usually national or international standards, through an unbroken chain of

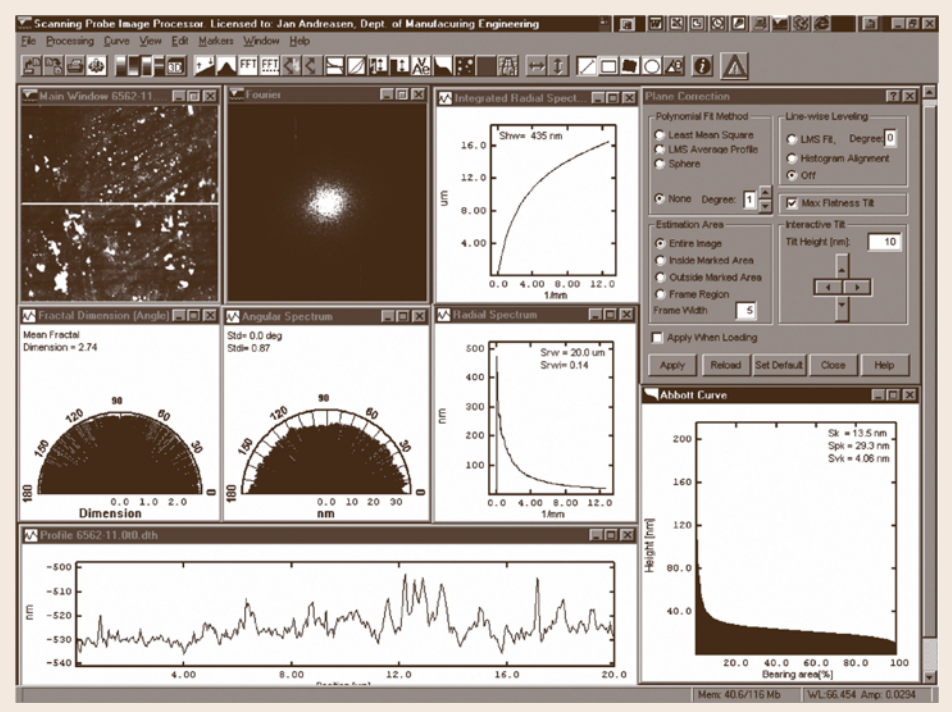

Fig. 6.29 Example of comprehensive information associated with surface analysis using SPIP (after [6.236])

comparisons, all with stated uncertainties [6.261, 262]. In the case of surface roughness measurements, several factors influence this property, for example, the measurement principle, the characteristics of the instrument, the measurement procedure, and the data evaluation [6.263]. Calibration, traceability, and uncertainty issues in surface texture metrology are addressed in a NPL report by *Leach* [6.264]. A recent international comparison regarding surface texture traceability is reported in [6.265].

Calibration of Instruments

Standards and procedures for the verification of the entire measurement system are described in international standards [6.231, 266]. These standards cover the most conventional uses of the instruments and the most common parameters. The verification of algorithms for the calculation of surface roughness parameters can be carried out by means of software gages, thereby establishing traceability for the data evaluation or software. This principle is described in [6.199]. In the case of new methods for the characterization of surface texture (for example, integral methods), new approaches have to be taken in order to establish traceability. Here, the measurement principle, including the physical principle as well as the data evaluation method, must be taken into account, and the procedure and principle are essential to the result. An example is the common effort to establish traceability for atomic force microscopy, where not only the physical principle of the instrumentation but also the data evaluation methods are investigated [6.267–269].

Some examples of 2-D surface texture calibration standards described by ISO are shown in Fig. 6.30. These calibration standards can be purchased from roughness instrument manufacturers, and their accredited calibration is provided by a large number of laboratories. Methods and standards for 3-D instrument calibration are currently under standardization by ISO TC213 (Table 6.10).

The minimum necessary equipment for calibration of a stylus instrument for general industrial use is an optical flat to check the background noise and an ISO type C or D standard with a known parameter value (Ra or Rz). The background noise, which originates from the electrical and mechanical parts in the instrument, results in a systematic error. As a main rule, the roughness measuring instrument should only be used for measurements of specimens with parameter values higher than five times the background noise. Typical background noise levels are

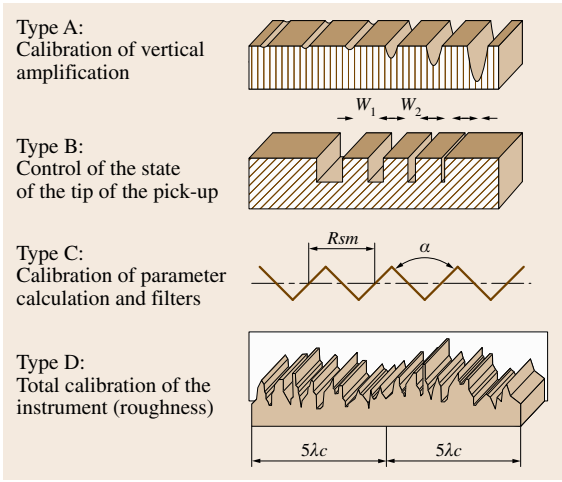

Fig. 6.30 Examples of surface texture calibration standards described by ISO 5436 (after [6.199, 231])

1. portable roughness measuring instruments *Ra*: 0.02–0.05 µm,
2. stationary roughness measuring instruments *Ra*: 0.002–0.01 µm.

The magnifications of instruments with external pick-up data can be calibrated using an ISO type A standard. It is customary to use calibration standards frequently, in connection with the use of the instruments.

Calibration of optical instruments is not as well established as calibration of stylus instruments [6.238, 258, 270, 271]. A proposal for a guideline to calibrate interference microscopes using the same artifacts and procedures that are used for stylus instruments is presented in [6.271].

Calibration of SPMs, currently still under development, encompasses scaling, nonlinearity, hysteresis, and orthogonality of *x*-*y*-*z*-axes, as well as shape, size, and dynamics of the probe [6.239, 267–269]. Transfer standards designed for certification are available through the instrument manufacturers, while their certification can be obtained from major national metrological institutes (PTB, NPL, NIST, etc.).

Uncertainty Budgeting

Upon calibration using a transfer standard, it is possible to produce an uncertainty budget for measurements with a stylus instrument. An example of an uncertainty budget for the calibration of an instrument using an ISO type C standard with a certified uncertainty U_n follows. The budget contains three components that can be calculated from knowledge about

1. reference uncertainty,
2. background noise level, and
3. measurement repeatability.

Following a convention, u indicates the standard uncertainty at the 1σ level, while U is for the 95% confidence level at a coverage factor of 2.

- Uncertainty of the calibration standard from certificate: $u_n = U_n/2$
- Uncertainty in the transfer of traceability (repeatability of the instrument): $u_r = \mathrm{STD}_r/\sqrt{n}$, where n is the number of measurements in the same track with the standard deviation STD_r;
- Uncertainty caused by the background noise: $u_b = \frac{1}{2} Rx0/\sqrt{3}$, where $Rx0$ is the measured background noise (average $Ra0$ or $Rz0$ value measured on an optical flat, assuming rectangular noise distribution);
- Total uncertainty: $U_{inst} = 2\sqrt{u_n^2 + u_r^2 + u_b^2}$.

If the same instrument is used for measurements on a workpiece, the resulting uncertainty increases with the variation in roughness of the workpiece, which is determined by taking measurements at different locations. It shall be noted that this component (estimated as u_s) depends on whether or not the measurement result is used for tolerance verification.

- u_s is the uncertainty caused by variations in the roughness of the specimen at different locations (n is the number of measurements carried out on the specimen with corresponding standard deviation STD_s)
- General (without tolerance verification): $u_s = \mathrm{STD}_s/\sqrt{n}$;
- Verification after the 16% rule (ISO 4288): $u_s = 1/2\mathrm{STD}_s/\sqrt{n}$;
- Verification after the max rule (ISO 4288 [6.198]): $u_s = 0$ (single measurements);
- Total uncertainty: $U_{tot} = 2\sqrt{u_n^2 + u_r^2 + u_b^2 + u_s^2}$.

It may be worth reminding the reader that the uncertainties only refer to the properties of the sample within the zone defined on the Stedman plot in Fig. 6.2; they are not necessarily the true uncertainties.

Current Situation and Future Developments

The present situation concerning surface metrology can be illustrated with respect to the traceability of surface

topography measurements. Figure 6.31 shows the range of different calibration standards currently available. Comparing the present possibilities with the measurement ranges covered by existing instruments (Fig. 6.16), and with the requirements from production [6.261], the need for developments in the nanometer range is clear. Traceable calibration of optical surface roughness instruments is also challenging [6.270–272]. Another clear challenge is the true three-dimensional characterization of surface details involving reentrances, as discussed in [6.241, 261, 272].

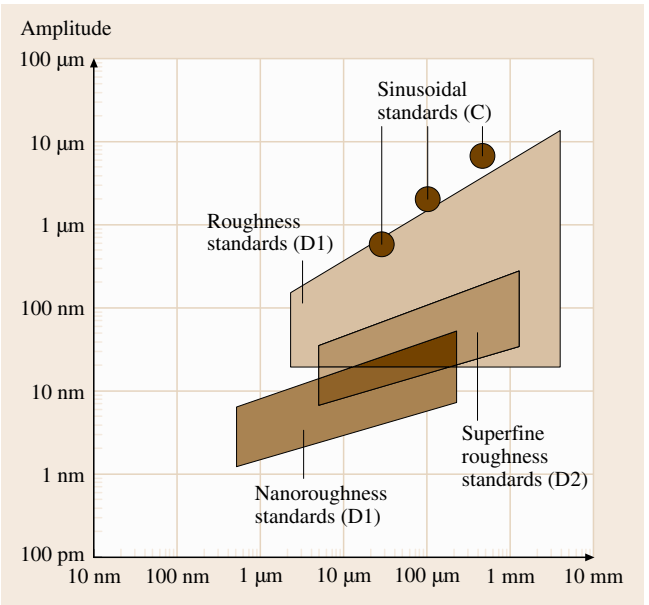

Fig. 6.31 Diagram of wavelength versus amplitude for different surface roughness calibration standards (courtesy of the PTB from [6.261])

6.2.8 Summary

Surface topography characterization encompasses measurement, visualization, and quantification. The principal methods of surface topography measurement are stylus profilometry, optical scanning techniques, and scanning probe microscopy (SPM). These methods, based on the acquisition of topography data from point-by-point scans, give quantitative information on heights with respect to position. Based on a different approach, the so-called integral methods produce parameters representing some average property of the surface under

Table 6.13 Merits, limitations, and applications of some techniques for surface topography analysis

Technique	Merits	Limitations	Applications
Stylus profilometry	Large vertical and lateral range Slopes up to 60° Robust Universally applicable externally as well as for internal measurements	Micrometer resolution Scratches soft surfaces	All kinds of industrial surfaces
Autofocus profilometry	Noncontact	Maximum slope 15° Signal problems on shiny or transparent materials	Soft as well as hard surfaces
White-light interferometry	Fast method High vertical resolving power (down to 0.1 nm)	Limited lateral resolution Maximum detectable slope up to about 30°	Roughness of flat surfaces Film thickness Low-aspect-ratio MST components (MST: Micro Systems Technologies)
Confocal microscopy	High-aspect-ratio structures Maximum detectable slope up to 75°	Limited lateral resolution Limited vertical resolution in some commercially available instruments	Dimensions of high-aspect-ratio MST components
Scanning electron microscopy	Wide range of operation, from less than 100× up to 100 000× Nanometer resolution Large depth of field Large working distance	Requires conductive sample material or preparation Small area for calculation of roughness parameters	Nanotechnology All kinds of material
Scanning probe microscopy	Nanometer/subnanometer resolution	Slow method Limited lateral and vertical range	Nanotechnology Nanoroughness

examination. Measurement methods, as well as their application and limitations, have been briefly reviewed, including standardization and traceability issues. Table 6.13, adapted from [6.239], gives an overview of the merits, limitations, and typical applications of different techniques for surface topography measurements.

References

6.1 I.S. Gilmore, M.P. Seah, J.E. Johnstone: Quantification issues in ToF-SIMS and AFM coanalysis in two-phase systems, exampled by a polymer blend, Surf. Interface Anal. **35**, 888 (2003)

6.2 ASTM: *Annual Book of ASTM Standards*, Vol. 03.06 (ASTM, West Conshohocken 2003)

6.3 ISO: *List of Technical Committees* (International Organization for Standardization, Geneva) http://www.iso.org/iso/standards_development/technical_committees/list_of_iso_technical_committees.htm

6.4 NPL: *Surface and Nano-Analysis* (National Physical Laboratory, Teddington) http://www.npl.co.uk/nanoanalysis

6.5 NIST: *Surface Data*, NIST Scientific and Technical Data Base (NIST, Gaithersburg) http://www.nist.gov/srd/surface.cfm

6.6 D. Briggs, M.P. Seah (Eds.): *Practical Surface Analysis. Auger and X-ray Photoelectron Spectroscopy*, Vol. 1 (Wiley, Chichester 1990)

6.7 D. Briggs, M.P. Seah (Eds.): *Practical Surface Analysis. Ion and Neutral Spectroscopy*, Vol. 2 (Wiley, Chichester 1992)

6.8 D. Briggs, J.T. Grant (Eds.): *Surface Analysis by Auger and X-ray Photoelectron Spectroscopy* (IM Publications and Surface Spectra, Manchester 2003)

6.9 S. Morton: UK Surface Analysis Forum http://www.uksaf.org/home.html

6.10 Y. Homma: Summary of ISO/TC 201 Standard, II ISO14237:2000 – SCA – Secondary-ion mass spectrometry – Determination of boron atomic concentration in silicon using uniformly doped materials, Surf. Interface Anal. **33**, 361 (2002)

6.11 K. Kajiwara: Summary of ISO/TC 201 Standard, IV ISO14606:2000 – SCA – Sputter depth profiling – Optimization using layered systems as reference materials, Surf. Interface Anal. **33**, 365 (2002)

6.12 K. Yoshihara: Summary of ISO/TC 201 Standard, V ISO14975:2000 – SCA – Information formats, Surf. Interface Anal. **33**, 367 (2002)

6.13 M.P. Seah: Summary of ISO/TC 201 Standard, I ISO14976:1998 – SCA – Data transfer format, Surf. Interface Anal. **27**, 693 (1999)

6.14 M.P. Seah: Summary of ISO/TC 201 Standard, VII ISO15472:2001 – SCA – X-ray photoelectron spectrometers – Calibration of energy scales, Surf. Interface Anal. **31**, 721 (2001)

6.15 S. Hofmann: Summary of ISO/TC 201 Standard, IX ISOTR15969:2000 – SCA – Depth profiling – Measurement of sputtered depth, Surf. Interface Anal. **33**, 453 (2002)

6.16 Y. Homma: Summary of ISO/TC 201 Standard, X ISO17560:2002 – SCA – Secondary-ion mass spectrometry – Method for depth profiling of boron in silicon, Surf. Interface Anal. **37**, 90 (2005)

6.17 M.P. Seah: Summary of ISO/TC 201 Standard, XII ISO17973:2002 – SCA – Medium-resolution Auger electron spectrometers – Calibration of energy scales for elemental analysis, Surf. Interface Anal. **35**, 329 (2002)

6.18 M.P. Seah: Summary of ISO/TC 201 Standard, XI ISO17974:2002 – SCA – High-resolution Auger electron spectrometers – Calibration of energy scales for elemental and chemical-state analysis, Surf. Interface Anal. **35**, 327 (2003)

6.19 D.S. Simons: Summary of ISO/TC 201 Standard: XIII, ISO 18114:2003 – SCA – Secondary-ion mass spectrometry – Determination of relative sensitivity factors from ion-implanted reference materials, Surf. Interface Anal. **38**, 171 (2006)

6.20 M.P. Seah: Summary of ISO/TC 201 Standard, VIII ISO18115:2001 – SCA – Vocabulary, Surf. Interface Anal. **31**, 1048 (2001)

6.21 M.P. Seah: Summary of ISO/TC 201 Standard: XXVIII, ISO 18115:2001/Amd.1:2006 – SCA – Vocabulary – Amendment 1, Surf. Interface Anal. **39**, 367 (2007)

6.22 M.P. Seah: Summary of ISO/TC 201 Standard: XXXIII, ISO 18115:2001/Amd.2:2007 – SCA – Vocabulary – Amendment 2, Surf. Interface Anal. **40**, 1500 (2008)

6.23 S. Tanuma: Summary of ISO/TC 201 Standard: XX, ISO 18118:2004 – SCA – Auger electron spectroscopy and x-ray photoelectron spectroscopy – Guide to the use of experimentally determined relative sensitivity factors for the quantitative analysis of homogeneous materials, Surf. Interface Anal. **38**, 178 (2006)

6.24 L. Kövér: Summary of ISO/TC 201 Standard: XXV, ISO 18392:2005 – SCA – X-ray photoelectron spectroscopy –procedures for determining backgrounds, Surf. Interface Anal. **38**, 1173 (2006)

6.25 L. Kövér: Summary of ISO/TC 201 Standard: XXX, ISO TR 18394:2006 – SCA – Auger electron spectroscopy – Derivation of chemical information, Surf. Interface Anal. **39**, 556 (2007)

6.26 J. Wolstenholme: Summary of ISO/TC 201 Standard: XXXI, ISO 18516:2006 – SCA – Auger electron spectroscopy and x-ray photoelectron spectroscopy – Determination of lateral resolution, Surf. Interface Anal. **40**, 966 (2008)

6.27 D.R. Baer: Summary of ISO/TC 201 Standard: XVIII, ISO 19318:2004 – SCA – X-ray photoelectron spectroscopy – Reporting of methods used for charge control and charge correction, Surf. Interface Anal. **37**, 524 (2005)

6.28 C.J. Powell: Summary of ISO/TC 201 Standard, XIV ISOTR19319:2003 – SCA – Auger electron spectroscopy and x-ray photoelectron spectroscopy – Determination of lateral resolution, analysis area, and sample area viewed by the analyser, Surf. Interface Anal. **36**, 666 (2004)

6.29 D.W. Moon: Summary of ISO/TC 201 Standard, XV ISO20341:2003 – SCA – Secondary-ion mass spectrometry – Method for estimating depth resolution parameters with multiple delta-layer reference materials, Surf. Interface Anal. **37**, 646 (2005)

6.30 C.J. Powell: Summary of ISO/TC 201 Standard: XXIX, ISO 20903:2006 – SCA – Auger electron spectroscopy and x-ray photoelectron spectroscopy – Methods used to determine peak intensities and information required when reporting results, Surf. Interface Anal. **39**, 464 (2007)

6.31 M.P. Seah: Summary of ISO/TC 201 Standard, XXI. ISO21270:2004 – SCA – X-ray photoelectron and Auger electron spectrometers – Linearity of intensity scale, Surf. Interface Anal. **36**, 1645 (2004)

6.32 I.S. Gilmore, M.P. Seah, A. Henderson: Summary of ISO/TC 201 Standard, XXII ISO22048:2004 – SCA – Information format for static secondary ion mass spectrometry, Surf. Interface Anal. **36**, 1642 (2004)

6.33 M.P. Seah: Summary of ISO/TC 201 Standard: XXIII, ISO 24236:2005 – SCA – Auger electron spectroscopy – Repeatability and constancy of intensity scale, Surf. Interface Anal. **39**, 86 (2007)

6.34 M.P. Seah: Summary of ISO/TC 201 Standard: XXIV, ISO 24237:2005 – SCA – X-ray photoelectron spectroscopy – Repeatability and constancy of intensity scale, Surf. Interface Anal. **39**, 370 (2007)

6.35 M.P. Seah, W.A. Dench: Quantitative electron spectroscopy of surfaces – A standard data base for electron inelastic mean free paths in solids, Surf. Interface Anal. **1**, 2 (1979)

6.36 C.P. Hunt, M.P. Seah: A submonolayer adsorbate reference material based on a low alloy steel fracture sample for Auger electron spectroscopy, I: Characterisation, Mater. Sci. Technol. **8**, 1023 (1992)

6.37 A. Savitzky, M.J.E. Golay: Smoothing and differentiation of data by simplified least squares procedures, Anal. Chem. **36**, 1627 (1964)

6.38 J. Steiner, Y. Termonia, J. Deltour: Comments on *Smoothing and differentiation of data by simplified least squares procedures*, Anal. Chem. **44**, 1906 (1972)

6.39 L.E. Davis, N.C. MacDonald, P.W. Palmberg, G.E. Riach, R.E. Weber: *Handbook of Auger Electron Spectroscopy*, 2nd edn. (Physical Electronics Industries, Eden Prairie 1976)

6.40 G.E. McGuire: *Auger Electron Spectroscopy Reference Manual* (Plenum, New York 1979)

6.41 Y. Shiokawa, T. Isida, Y. Hayashi: *Auger Electron Spectra Catalogue: A Data Collection of Elements* (Anelva, Tokyo 1979)

6.42 T. Sekine, Y. Nagasawa, M. Kudoh, Y. Sakai, A.S. Parkes, J.D. Geller, A. Mogami, K. Hirata: *Handbook of Auger Electron Spectroscopy* (JEOL, Tokyo 1982)

6.43 K.D. Childs, B.A. Carlson, L.A. Lavanier, J.F. Moulder, D.F. Paul, W.F. Stickle, D.G. Watson: *Handbook of Auger Electron Spectroscopy* (Physical Electronics Industries, Eden Prairie 1995)

6.44 M.P. Seah, I.S. Gilmore, H.E. Bishop, G. Lorang: Quantitative AES V, Practical analysis of intensities with detailed examples of metals and their oxides, Surf. Interface Anal. **26**, 701 (1998)

6.45 M.P. Seah, C.P. Hunt: Atomic mixing and electron range effects in ultra high resolution profiles of the Ta/Ta_2O_5 interface by argon sputtering with AES, J. Appl. Phys. **56**, 2106 (1984)

6.46 J. Pauwels: Institute of Reference Materials and Measurements (IRMM), Retieseweg, 2440 Geel, Belgium

6.47 C.P. Hunt, M.P. Seah: Characterisation of high depth resolution tantalum pentoxide sputter profiling reference material, Surf. Interface Anal. **5**, 199 (1983)

6.48 M.P. Seah, S.J. Spencer, I.S. Gilmore, J.E. Johnstone: Depth resolution in sputter depth profiling – Characterisation of a tantalum pentoxide on tantalum certified reference material, Surf. Interface Anal. **29**, 73 (2000)

6.49 M.P. Seah, S.J. Spencer: Ultra-thin SiO_2 on Si, I: Quantifying and removing carbonaceous contamination, J. Vac. Sci. Technol. A **21**, 345 (2003)

6.50 M.P. Seah, G.C. Smith, M.T. Anthony: AES – Energy calibration of electron spectrometers. I: An absolute, traceable energy calibration and the provision of atomic reference line energies, Surf. Interface Anal. **15**, 293 (1990)

6.51 M.P. Seah, I.S. Gilmore: AES – Energy calibration of electron spectrometers. III: General calibration rules, J. Electron Spectrosc. **83**, 197 (1997)

6.52 M.P. Seah: AES – energy calibration of electron spectrometers. IV: A re-evaluation of the reference energies, J. Electron Spectrosc. **97**, 235 (1998)

6.53 M.P. Seah, G.C. Smith: Spectrometer energy scale calibration. In: *Practical Surface Analysis. Auger and X-ray Photoelectron Spectroscopy*, Vol. 1, ed. by D. Briggs, M.P. Seah (Wiley, Chichester 1990) p. 531, Appendix 1

6.54 P.J. Cumpson, M.P. Seah, S.J. Spencer: Simple procedure for precise peak maximum estimation for energy calibration in AES and XPS, Surf. Interface Anal. **24**, 687 (1996)

6.55 M.P. Seah: Channel electron multipliers: Quantitative intensity measurement – Efficiency, gain, linearity and bias effects, J. Electron Spectrosc. **50**, 137 (1990)

6.56 M.P. Seah, C.S. Lim, K.L. Tong: Channel electron multiplier efficiencies – The effect of the pulse-height distribution on spectrum shape in Auger electron spectroscopy, J. Electron Spectrosc. **48**, 209 (1989)

6.57 M.P. Seah, M. Tosa: Linearity in electron counting and detection systems, Surf. Interface Anal. **18**, 240 (1992)

6.58 M.P. Seah: Effective dead time in pulse counting systems, Surf. Interface Anal. **23**, 729 (1995)

6.59 M.P. Seah, I.S. Gilmore, S.J. Spencer: Signal linearity in XPS counting systems, J. Electron Spectrosc. **104**, 73 (1999)

6.60 M.P. Seah, I.S. Gilmore, S.J. Spencer: Method for determining the signal linearity in single and multidetector counting systems in XPS, Appl. Surf. Sci. **144/145**, 132 (1999)

6.61 M.P. Seah, G.C. Smith: AES – Accurate intensity calibration of spectrometers – Results of a BCR interlaboratory comparison cosponsored by the VAMAS SCA TWP, Surf. Interface Anal. **17**, 855 (1991)

6.62 M.P. Seah: A system for the intensity calibration of electron spectrometers, J. Electron Spectrosc. **71**, 191 (1995)

6.63 M.P. Seah: XPS – Reference procedures for the accurate intensity calibration of electron spectrometers – Results of a BCR intercomparison cosponsored by the VAMAS SCA TWP, Surf. Interface Anal. **20**, 243 (1993)

6.64 M.P. Seah, G.C. Smith: Quantitative AES and XPS determination of the electron spectrometer transmission function and the detector sensitivity energy dependencies for the production of true electron emission spectra in AES and XPS, Surf. Interface Anal. **15**, 751 (1990)

6.65 NPL: *Systems for the Intensity Calibration of Auger and X-ray Photoelectron Spectrometers, A1 and X1* (National Physical Laboratory, Teddington 2005), see http://www.npl.co.uk/nanoanalysis/a1calib.html and follow links

6.66 M.P. Seah: Scattering in electron spectrometers, diagnosis and avoidance. I: Concentric hemispherical analysers, Surf. Interface Anal. **20**, 865 (1993)

6.67 S. Tougaard: X-ray photoelectron spectroscopy peak shape analysis for the extraction of in-depth composition information, J. Vac. Sci. Technol. A **5**, 1275 (1987)

6.68 S. Tougaard, C. Jannsson: Comparison of validity and consistency of methods for quantitative XPS peak analysis, Surf. Interface Anal. **20**, 1013 (1993)

6.69 M.P. Seah: Data compilations – Their use to improve measurement certainty in surface analysis by AES and XPS, Surf. Interface Anal. **9**, 85 (1986)

6.70 M.P. Seah: Quantitative AES and XPS. In: *Practical Surface Analysis. Auger and X-ray Photoelectron Spectroscopy*, Vol. 1, ed. by D. Briggs, M.P. Seah (Wiley, Chichester 1990) p. 201, Chap. 5

6.71 M. Gryzinski: Classical theory of atomic collisions. I: Theory of inelastic collisions, Phys. Rev. A **138**, 336 (1965)

6.72 M.P. Seah, I.S. Gilmore: Quantitative AES. VII: The ionisation cross section in AES, Surf. Interface Anal. **26**, 815 (1998)

6.73 E. Casnati, A. Tartari, C. Baraldi: An empirical approach to K-shell ionization cross section by electrons, J. Phys. B **15**, 155 (1982)

6.74 E.H.S. Burhop: *The Auger Effect and Other Radiationless Transitions* (Cambridge Univ. Press, Cambridge 1952)

6.75 J.I. Goldstein, H. Yakowitz (Eds.): *Practical Scanning Electron Microscopy* (Plenum, New York 1975)

6.76 M.P. Seah, I.S. Gilmore: A high resolution digital Auger database of true spectra for AES intensities, J. Vac. Sci. Technol. A **14**, 1401 (1996)

6.77 R. Shimizu: Quantitative analysis by Auger electron spectroscopy, Jpn. J. Appl. Phys. **22**, 1631 (1983)

6.78 M.P. Seah, I.S. Gilmore: Quantitative AES. VIII: Analysis of Auger electron intensities for elemental data in a digital auger database, Surf. Interface Anal. **26**, 908 (1998)

6.79 G.W.C. Kaye, T.H. Laby: *Tables of Physical and Chemical Constants*, 15th edn. (Longmans, London 1986)

6.80 D.R. Lide (Ed.): *CRC Handbook of Chemistry and Physics*, 74th edn. (CRC, Boca Raton 1993)

6.81 A. Jablonski: Database of correction parameters for elastic scattering effects in XPS, Surf. Interface Anal. **23**, 29 (1995)

6.82 M.P. Seah, I.S. Gilmore: Simplified equations for correction parameters for elastic scattering effects for Q, β and attenuation lengths in AES and XPS, Surf. Interface Anal. **31**, 835 (2001)

6.83 S. Tanuma, C.J. Powell, D.R. Penn: Calculations of electron inelastic mean free paths (IMFPs). V: Data for 14 organic compounds over the 50 – 2000 eV range, Surf. Interface Anal. **21**, 165 (1994)

6.84 S. Tanuma, C.J. Powell, D.R. Penn: Calculations of electron inelastic mean free paths. VII: Reliability of the TPP-2M IMFP predictive equation, Surf. Interface Anal. **35**, 268 (2003)

6.85 NIST: *SRD 71 Electron Inelastic Mean Free Path Database, Version 1.1* (NIST, Gaithersburg 2001)

6.86 M.P. Seah, I.S. Gilmore, S.J. Spencer: Quantitative XPS. I: Analysis of x-ray photoelectron intensities from elemental data in a digital photoelectron database, J. Electron. Spectrosc. **120**, 93 (2001)

6.87 P.J. Cumpson: Angle-resolved x-ray photoelectron spectroscopy. In: *Surface Analysis by Auger and X-ray Photoelectron Spectroscopy*, ed. by D. Briggs, J.T. Grant (IM Publications and Surface Spectra, Manchester 2003) p. 651, Chap. 23

6.88 S. Tougaard: Quantification of nanostructures by electron spectroscopy. In: *Surface Analysis by Auger and X-ray Photoelectron Spectroscopy*, ed. by D. Briggs, J.T. Grant (IM Publications and Surface Spectra, Manchester 2003) p. 295, Chap. 12

6.89 S. Hofmann, J.M. Sanz: Quantitative XPS analysis of the surface layer of anodic oxides obtained during

depth profiling by sputtering with 3 keV Ar^+ ions, J. Trace Microprobe Tech. **1**, 213 (1982)
6.90 S. Hofmann: Depth profiling in AES and XPS. In: *Practical Surface Analysis. Auger and X-ray Photoelectron Spectroscopy*, Vol. 1, ed. by D. Briggs, M.P. Seah (Wiley, Chichester 1990) p. 143, Chap. 4
6.91 J.M. Sanz, S. Hofmann: Quantitative evaluation of AES-depth profiles of thin anodic oxide films (Ta_2O_5/Ta, Nb_2O_5/Nb), Surf. Interface Anal. **5**, 210 (1983)
6.92 J.F. Ziegler: *The Stopping and Range of Ions in Matter SRIM-2003*, SRIM-2003 v.02 SRIM code (IBM, Yorktown Heights 2005), available for download from http://www.SRIM.org
6.93 M.P. Seah, F.M. Green, C.A. Clifford, I.S. Gilmore: An accurate semi-empirical equation for sputtering yields. I: For argon ions, Surf. Interface Anal. **37**, 444 (2005)
6.94 O. Auciello, R. Kelly (Eds.): *Ion Bombardment Modifications of Surfaces* (Elsevier, Amsterdam 1984)
6.95 R. Kelly: On the role of Gibbsian segregation in causing preferential sputtering, Surf. Interface Anal. **7**, 1 (1985)
6.96 J.B. Malherbe, R.Q. Odendaal: Models for the sputter correction factor in quantitative AES for compound semiconductors, Surf. Interface Anal. **26**, 841 (1998)
6.97 T. Wagner, J.Y. Wang, S. Hofmann: Sputter depth profiling in AES and XPS. In: *Surface Analysis by Auger and X-ray Photoelectron Spectroscopy*, ed. by D. Briggs, J.T. Grant (IM Publications and Surface Spectra, Manchester 2003) p. 619, Chap. 22
6.98 M.P. Seah, C.P. Hunt: The depth dependence of the depth resolution in composition-depth profiling with auger electron spectroscopy, Surf. Interface Anal. **5**, 33 (1983)
6.99 M.P. Seah, J.M. Sanz, S. Hofmann: The statistical sputtering contribution to resolution in concentration-depth profiles, Thin Solid Films **81**, 239 (1981)
6.100 NPL: *Sputtering Yields for Neon, Argon and Xenon Ions* (National Physical Laboratory, Teddington 2005), available for download from http://www.npl.co.uk/nanoscience/surface-nanoanalysis/products-and-services/sputter-yield-values
6.101 A. Zalar: Improved depth resolution by sample rotation during Auger electron spectroscopy depth profiling, Thin Solid Films **124**, 223 (1985)
6.102 S. Hofmann, A. Zalar, E.-H. Cirlin, J.J. Vajo, H.J. Mathieu, P. Panjan: Interlaboratory comparison of the depth resolution in sputter depth profiling of Ni/Cr multilayers with and without sample rotation using AES, XPS, and SIMS, Surf. Interface Anal. **20**, 621 (1993)
6.103 C.P. Hunt, M.P. Seah: Method for the alignment of samples and the attainment of ultra-high resolution depth profiles in Auger electron spectroscopy, Surf. Interface Anal. **15**, 254 (1990)
6.104 M.P. Seah: An accurate semi-empirical equation for sputtering yields. II: For neon, argon and xenon ions, Nucl. Instrum. Methods B **229**, 348 (2005)
6.105 I.S. Gilmore, M.P. Seah: Fluence, flux, current, and current density measurement in faraday cups for surface analysis, Surf. Interface Anal. **23**, 248 (1995)
6.106 J.A. Bearden, A.F. Burr: X-ray wavelengths and x-ray atomic energy levels, Rev. Mod. Phys. **31**, 49 (1967)
6.107 C.D. Wagner, W.M. Riggs, L.E. Davis, J.F. Moulder, G.E. Muilenberg: *Handbook of X-ray Photoelectron Spectroscopy* (Physical Electrons Industries, Eden Prairie 1979)
6.108 N. Ikeo, Y. Iijima, N. Niimura, M. Sigematsu, T. Tazawa, S. Matsumoto, K. Kojima, Y. Nagasawa: *Handbook of X-ray Photoelectron Spectroscopy* (JEOL, Tokyo 1991)
6.109 J.F. Moulder, W.F. Stickle, S.E. Sobol, K.D. Bomben: *Handbook of X-ray Photoelectron Spectroscopy* (Perkin Elmer/Physical Electronics Division, Eden Prairie 1992)
6.110 C.D. Wagner: Photoelectron and Auger energies and the Auger parameter – A data set. In: *Practical Surface Analysis. Auger and X-ray Photoelectron Spectroscopy*, Vol. 1, ed. by D. Briggs, M.P. Seah (Wiley, Chichester 1990) p. 595, Appendix 5
6.111 C.D. Wagner, A.V. Naumkin, A. Kraut-Vass, J.W. Allison, C.J. Powell, J.R. Rumble: *NIST XPS Database* (NIST, Gaithersburg 2005), http://srdata.nist.gov/xps/
6.112 M.P. Seah: Post-1989 calibration energies for x-ray photoelectron spectrometers and the 1990 Josephson constant, Surf. Interface Anal. **14**, 488 (1989)
6.113 M.P. Seah, I.S. Gilmore, S.J. Spencer: XPS – Energy calibration of electron spectrometers 4 – An assessment of effects for different conditions and of the overall uncertainties, Surf. Interface Anal. **26**, 617 (1998)
6.114 M.P. Seah, I.S. Gilmore, G. Beamson: XPS – Binding energy calibration of electron spectrometers 5 – A re-assessment of the reference energies, Surf. Interface Anal. **26**, 642 (1998)
6.115 G. Beamson, D. Briggs: *High-Resolution XPS of Organic Polymers – The Scienta ESCA300 Database* (Wiley, Chichester 1992)
6.116 M.P. Seah, S.J. Spencer: Degradation of poly(vinyl chloride) and nitrocellulose in XPS, Surf. Interface Anal. **35**, 906 (2003)
6.117 ISO 17025: *ISO: General Requirements for the Competence of Testing and Calibration Laboratories* (ISO, Geneva 2000)
6.118 D.A. Shirley: High-resolution x-ray photoemission spectrum of the valence bands of gold, Phys. Rev. B **5**, 4709 (1972)
6.119 C.D. Wagner: Empirically derived atomic sensitivity factors for XPS. In: *Practical Surface Analysis. Auger and X-ray Photoelectron Spectroscopy*, Vol. 1, ed. by D. Briggs, M.P. Seah (Wiley, Chichester 1990) p. 635, Appendix 6

6.120 C.D. Wagner, L.E. Davis, M.V. Zeller, J.A. Taylor, R.M. Raymond, L.H. Gale: Empirical atomic sensitivity factors for quantitative analysis by electron spectroscopy for chemical analysis, Surf. Interface Anal. **3**, 211 (1981)

6.121 J.H. Scofield: Hartree–Slater subshell photoionization cross-sections at 1254 and 1487 eV, J. Electron Spectrosc. **8**, 129 (1996)

6.122 M.P. Seah, I.S. Gilmore, S.J. Spencer: Quantitative AES IX and quantitative XPS II: Auger and x-ray photoelectron intensities from elemental spectra in digital databases reanalysed with a REELS database, Surf. Interface Anal. **31**, 778 (2001)

6.123 J.J. Yeh, I. Lindau: Atomic subshell photoionization cross sections and asymmetry parameters: $1 \leq Z \leq 103$, At. Data Nucl. Data Tables **32**, 1 (1985)

6.124 R.F. Reilman, A. Msezane, S.T. Manson: Relative intensities in photoelectron spectroscopy of atoms and molecules, J. Electron Spectrosc. **8**, 389 (1970)

6.125 M.P. Seah: Quantification in AES and XPS. In: *Surface Analysis by Auger and X-ray Photoelectron Spectroscopy*, ed. by D. Briggs, J.T. Grant (IM Publications Surface Spectra, Manchester 2003) p. 345, Chap. 13

6.126 NIST: *SRD 64 Electron Elastic Scattering Cross-Section Database* (NIST, Gaithersburg 2002), Version 2.0

6.127 P.J. Cumpson, M.P. Seah: Elastic scattering corrections in AES and XPS II – Estimating attenuation lengths, and conditions required for their valid use in overlayer/substrate experiments, Surf. Interface Anal. **25**, 430 (1997)

6.128 A. Jablonski, C.J. Powell: The electron attenuation length revisited, Surf. Sci. Rep. **47**, 33 (2002)

6.129 P.J. Cumpson: The thickogram: A method for easy film thickness measurements in XPS, Surf. Interface Anal. **29**, 403 (2000)

6.130 M.P. Seah, S.J. Spencer, F. Bensebaa, I. Vickridge, H. Danzebrink, M. Krumrey, T. Gross, W. Oesterle, E. Wendler, B. Rheinländer, Y. Azuma, I. Kojima, N. Suzuki, M. Suzuki, S. Tanuma, D.W. Moon, H.J. Lee, M.C. Hyun, H.Y. Chen, A.T.S. Wee, T. Osipowicz, J.S. Pan, W.A. Jordaan, R. Hauert, U. Klotz, C. van der Marel, M. Verheijen, Y. Tamminga, C. Jeynes, P. Bailey, S. Biswas, U. Falke, N.V. Nguyen, D. Chandler-Horowitz, J.R. Ehrstein, D. Muller, J.A. Dura: Critical review of the current status of thickness measurements for ultra-thin SiO_2 on Si: Part V Results of a CCQM pilot study, Surf. Interface Anal. **36**, 1269 (2004)

6.131 M.P. Seah: Intercomparison of silicon dioxide thickness measurements made by multiple techniques – The route to accuracy, J. Vac. Sci. Technol. A **22**, 1564 (2004)

6.132 M.P. Seah, S.J. Spencer: Ultra-thin SiO_2 on Si, II: Issues in quantification of the oxide thickness, Surf. Interface Anal. **33**, 640 (2002)

6.133 M.P. Seah, S.J. Spencer: Ultra-thin SiO_2 on Si, IV: Thickness linearity and intensity measurement in XPS, Surf. Interface Anal. **35**, 515 (2003)

6.134 M.P. Seah, S.J. Spencer: Ultrathin SiO_2 on Si, VII: Angular accuracy in XPS and an accurate attenuation length, Surf. Interface Anal. **37**, 731 (2005)

6.135 M.P. Seah, S.J. Spencer: Attenuation lengths in organic materials, Surf. Interface Anal. **43**, 744 (2011)

6.136 N. Sanada, Y. Yamamoto, R. Oiwa, Y. Ohashi: Extremely low sputtering degradation of polytetrafluoroethylene by C_{60} ion beam applied in XPS analysis, Surf. Interface Anal. **36**, 280 (2004)

6.137 T. Miyayama, N. Sanada, M. Suzuki, J.S. Hammond, S.-Q.D. Si, A. Takahara: X-ray photoelectron spectroscopy study of polyimide thin films with Ar cluster ion depth profiling, J. Vac. Sci. Technol. A **28**, L1 (2010)

6.138 A.G. Shard, F.M. Green, P.J. Brewer, M.P. Seah, I.S. Gilmore: Quantitative molecular depth profiling of organic delta-layers by C60 ion sputtering and SIMS, J. Phys. Chem. B **112**, 2596 (2008)

6.139 K. Wittmaack: Physical and chemical parameters determining ion yields in SIMS analyses: A closer look at the oxygen-induced yield enhancement effect, Proc. 11st Int. Conf. Second. Ion Mass Spectrom., SIMS XI, ed. by G. Gillen, R. Lareau, J. Bennett, F. Stevie (Wiley, Chichester 1998) p. 11

6.140 C.J. Hitzman, G. Mount: Enhanced depth profiling of ultra-shallow implants using improved low energy ion guns on a quadrupole SIMS instrument, Proc. 11st Int. Conf. Second. Ion Mass Spectrom., SIMS XI, ed. by G. Gillen, R. Lareau, J. Bennett, F. Stevie (Wiley, Chichester 1998) p. 273

6.141 I.S. Gilmore: Private communication (2004)

6.142 M.G. Dowsett, G. Rowland, P.N. Allen, R.D. Barlow: An analytic form for the SIMS response function measured from ultra-thin impurity layers, Surf. Interface Anal. **21**, 310 (1994)

6.143 D.W. Moon, J.Y. Won, K.J. Kim, H.J. Kang, M. Petravic: GaAs delta-doped layers in Si for evaluation of SIMS depth resolution, Surf. Interface Anal. **29**, 362 (2000)

6.144 M.G. Dowsett: Depth profiling using ultra-low-energy secondary ion mass spectrometry, Appl. Surf. Sci. **203/204**, 5 (2003)

6.145 K. Wittmaack: The "Normal Component" of the primary ion energy: An inadequate parameter for assessing the depth resolution in SIMS, Proc. 11st Int. Conf. Second. Ion Mass Spectrom., SIMS XII, ed. by A. Benninghoven, P. Bertrand, H.-N. Migeon, H.W. Werner (Wiley, Chichester 2000) p. 569

6.146 J. Bellingham, M.G. Dowsett, E. Collart, D. Kirkwood: Quantitative analysis of the top 5 nm of boron ultra-shallow implants, Appl. Surf. Sci. **203/204**, 851 (2003)

6.147 K. Iltgen, A. Benninghoven, E. Niehius: TOF-SIMS depth profiling with optimized depth resolution, Proc. 11st Int. Conf. Second. Ion Mass Spectrom., SIMS XI, ed. by G. Gillen, R. Lareau, J. Bennett, F. Stevie (Wiley, Chichester 1988) p. 367

6.148 C. Hongo, M. Tomita, M. Takenaka, M. Suzuki, A. Murakoshi: Depth profiling for ultrashallow implants using backside secondary ion mass spectrometry, J. Vac. Sci. Technol. B **21**, 1422 (2003)

6.149 J. Sameshima, R. Maeda, K. Yamada, A. Karen, S. Yamada: Depth profiles of boron and nitrogen in SiON films by backside SIMS, Appl. Surf. Sci. **231/232**, 614 (2004)

6.150 F. Laugier, J.M. Hartmann, H. Moriceau, P. Holliger, R. Truche, J.C. Dupuy: Backside and frontside depth profiling of B delta doping, at low energy, using new and previous magnetic SIMS instruments, Appl. Surf. Sci. **231/232**, 668 (2004)

6.151 D.W. Moon, H.J. Lee: The dose dependence of Si sputtering with low energy ions in shallow depth profiling, Appl. Surf. Sci. **203/204**, 27 (2003)

6.152 K. Wittmaack: Influence of the depth calibration procedure on the apparent shift of impurity depth profiles measured under conditions of long-term changes in erosion rate, J. Vac. Sci. Technol. B **18**, 1 (2001)

6.153 Y. Homma, H. Takenaka, F. Toujou, A. Takano, S. Hayashi, R. Shimizu: Evaluation of the sputter rate variation in SIMS ultra-shallow depth profiling using multiple short-period delta-layers, Surf. Interface Anal. **35**, 544 (2003)

6.154 F. Toujou, S. Yoshikawa, Y. Homma, A. Takano, H. Takenaka, M. Tomita, Z. Li, T. Hasgawa, K. Sasakawa, M. Schuhmacher, A. Merkulov, H.K. Kim, D.W. Moon, T. Hong, J.-Y. Won: Evaluation of BN-delta-doped multilayer reference materials for shallow depth profiling in SIMS: Round robin test, Appl. Surf. Sci. **231/232**, 649 (2004)

6.155 F.A. Stevie, P.M. Kahora, D.S. Simons, P. Chi: Secondary ion yield changes in Si and GaAs due to topography changes during O_2^+ or Cs^+ ion bombardment, J. Vac. Sci. Technol. A **6**, 76 (1988)

6.156 Y. Homma, A. Takano, Y. Higashi: Oxygen-ion-induced ripple formation on silicon: Evidence for phase separation and tentative model, Appl. Surf. Sci. **203/204**, 35 (2003)

6.157 K. Wittmaack: Artifacts in low-energy depth profiling using oxygen primary ion beams: Dependence on impact angle and oxygen flooding conditions, J. Vac. Sci. Technol. B **16**, 2776 (1998)

6.158 Z.X. Jiang, P.F.K. Alkemade: Erosion rate change and surface roughening in Si during oblique O_2^+ bombardment with oxygen flooding, Proc. 11st Int. Conf. Second. Ion Mass Spectrom., SIMS XI, ed. by G. Gillen, R. Lareau, J. Bennett, F. Stevie (Wiley, Chichester 1998) p. 431

6.159 K. Kataoka, K. Yamazaki, M. Shigeno, Y. Tada, K. Wittmaack: Surface roughening of silicon under ultra-low-energy cesium bombardment, Appl. Surf. Sci. **203/204**, 43 (2003)

6.160 K. Wittmaack: Concentration-depth calibration and bombardment-induced impurity relocation in SIMS depth profiling of shallow through-oxide implantation distributions: A procedure for eliminating the matrix effect, Surf. Interface Anal. **26**, 290 (1998)

6.161 M.G. Dowsett, J.H. Kelly, G. Rowlands, T.J. Ormsby, B. Guzman, P. Augustus, R. Beanland: On determining accurate positions, separations, and internal profiles for delta layers, Appl. Surf. Sci. **203/204**, 273 (2003)

6.162 J.B. Clegg, A.E. Morgan, H.A.M. De Grefte, F. Simondet, A. Huebar, G. Blackmore, M.G. Dowsett, D.E. Sykes, C.W. Magee, V.R. Deline: A comparative study of SIMS depth profiling of boron in silicon, Surf. Interface Anal. **6**, 162 (1984)

6.163 J.B. Clegg, I.G. Gale, G. Blackmore, M.G. Dowsett, D.S. McPhail, G.D.T. Spiller, D.E. Sykes: A SIMS calibration exercise using multi-element (Cr, Fe and Zn) implanted GaAs, Surf. Interface Anal. **10**, 338 (1987)

6.164 K. Miethe, E.H. Cirlin: An international round robin exercise on SIMS depth profiling of silicon delta-doped layers in GaAs, Proc. 9th Int. Conf. Second. Ion Mass Spectrom., SIMS IX, ed. by A. Benninghoven, Y. Nihei, R. Shimizu, H.W. Werner (Wiley, Chichester 1994) p. 699

6.165 Y. Okamoto, Y. Homma, S. Hayashi, F. Toujou, N. Isomura, A. Mikami, I. Nomachi, S. Seo, M. Tomita, A. Tamamoto, S. Ichikawa, Y. Kawashima, R. Mimori, Y. Mitsuoka, I. Tachikawa, T. Toyoda, Y. Ueki: SIMS round-robin study of depth profiling of boron implants in silicon, Proc. 11st Int. Conf. Second. Ion Mass Spectrom., SIMS XI, ed. by G. Gillen, R. Lareau, J. Bennett, F. Stevie (Wiley, Chichester 1998) p. 1047

6.166 F. Toujou, M. Tomita, A. Takano, Y. Okamoto, S. Hayashi, A. Yamamoto, Y. Homma: SIMS round-robin study of depth profiling of boron implants in silicon, II Problems of quantification in high concentration B profiles, Proc. 12nd Int. Conf. Second. Ion Mass Spectrom., SIMS XII, ed. by A. Benninghoven, P. Bertrand, H.-N. Migeon, H.W. Werner (Wiley, Chichester 2000) p. 101

6.167 M. Tomita, T. Hasegawa, S. Hashimoto, S. Hayashi, Y. Homma, S. Kakehashi, Y. Kazama, K. Koezuka, H. Kuroki, K. Kusama, Z. Li, S. Miwa, S. Miyaki, Y. Okamoto, K. Okuno, S. Saito, S. Sasaki, H. Shichi, H. Shinohara, F. Toujou, Y. Ueki, Y. Yamamoto: SIMS round-robin study of depth profiling of arsenic implants in silicon, Appl. Surf. Sci. **203/204**, 465 (2003)

6.168 I.S. Gilmore, M.P. Seah: Static SIMS: A study of damage using polymers, Surf. Interface Anal. **24**, 746 (1996)

6.169 I.S. Gilmore, M.P. Seah: Electron flood gun damage in the analysis of polymers and organics in time of flight SIMS, Appl. Surf. Sci. **187**, 89 (2002)

6.170 D. Briggs, A. Brown, J.C. Vickerman: *Handbook of Static Secondary Ion Mass Spectrometry (SIMS)* (Wiley, Chichester 1989)

6.171 J.G. Newman, B.A. Carlson, R.S. Michael, J.F. Moulder, T.A. Honit: *Static SIMS Handbook of Polymer Analysis* (Perkin Elmer, Eden Prairie 1991)

6.172 J.C. Vickerman, D. Briggs, A. Henderson: *The Static SIMS Library* (Surface Spectra, Manchester 2003), version 2

6.173 B.C. Schwede, T. Heller, D. Rading, E. Niehius, L. Wiedmann, A. Benninghoven: *The Münster High*

Mass Resolution Static SIMS Library (ION-TOF, Münster 2003)
6.174 I.S. Gilmore, M.P. Seah: Static TOF-SIMS – A VAMAS interlaboratory study, Part I: Repeatability and reproducibility of spectra, Surf. Interface Anal. **37**, 651 (2005)
6.175 F.M. Green, I.S. Gilmore, M.P. Seah: TOF-SIMS: Accurate mass scale calibration, J. Am. Mass Spectrom. Soc. **17**, 514 (2007)
6.176 I.S. Gilmore, M.P. Seah: A static SIMS interlaboratory study, Surf. Interface Anal. **29**, 624 (2000)
6.177 A. Benninghoven, D. Stapel, O. Brox, B. Binkhardt, C. Crone, M. Thiemann, H.F. Arlinghaus: Static SIMS with molecular primary ions, Proc. 12nd Int. Conf. Second. Ion Mass Spectrom., SIMS XII, ed. by A. Benninghoven, P. Bertrand, H.-N. Migeon, H.W. Werner (Wiley, Chichester 2000) p. 259
6.178 A. Schneiders, M. Schröder, D. Stapel, H.F. Arlinghaus, A. Benninghoven: Molecular secondary particle emission from molecular overlayers under SF_5^+ bombardment, Proc. 12nd Int. Conf. Second. Ion Mass Spectrom., SIMS XII, ed. by A. Benninghoven, P. Bertrand, H.-N. Migeon, H.W. Werner (Wiley, Chichester 2000) p. 263
6.179 R. Kersting, B. Hagenhoff, P. Pijpers, R. Verlack: The influence of primary ion bombardment conditions on the secondary ion emission behaviour of polymer additives, Appl. Surf. Sci. **203/204**, 561 (2003)
6.180 R. Kersting, B. Hagenhoff, F. Kollmer, R. Möllers, E. Niehuis: Influence of primary ion bombardment conditions on the emission of molecular secondary ions, Appl. Surf. Sci. **231/232**, 261 (2004)
6.181 S.C.C. Wong, R. Hill, P. Blenkinsopp, N.P. Lockyer, D.E. Weibel, J.C. Vickerman: Development of a C_{60}^+ ion gun for static SIMS and chemical imaging, Appl. Surf. Sci. **203/204**, 219 (2003)
6.182 D.E. Weibel, N. Lockyer, J.C. Vickerman: C_{60} cluster ion bombardment of organic surfaces, Appl. Surf. Sci. **231/232**, 146 (2003)
6.183 M.P. Seah: Cluster ion sputtering: Molecular ion yield relationships for different cluster primary ions in static SIMS of organic materials, Surf. Interface Anal. **39**, 890 (2007)
6.184 N. Davies, D.E. Weibel, P. Blenkinsopp, N. Lockyer, R. Hill, J.C. Vickerman: Development and experimental application of a gold liquid metal ion source, Appl. Surf. Sci. **203/204**, 223 (2003)
6.185 I.S. Gilmore, M.P. Seah: G-SIMS of crystallisable organics, Appl. Surf. Sci. **203/204**, 551 (2003)
6.186 I.S. Gilmore, M.P. Seah: Static SIMS: Towards unfragmented mass spectra – The G-SIMS procedure, Appl. Surf. Sci. **161**, 465 (2000)
6.187 I.S. Gilmore, M.P. Seah: Organic molecule characterisation – G-SIMS, Appl. Surf. Sci. **231/232**, 224 (2004)
6.188 M.P. Seah, F.M. Green, I.S. Gilmore: Cluster primary ion sputtering: Secondary ion intensities in static SIMS of organic materials, J. Phys. Chem. C **114**, 5351 (2010)
6.189 L. De Chiffre, P. Lonardo, H. Trumpold, D.A. Lucca, G. Goch, C.A. Brown, J. Raja, H.N. Hansen: Quantitative characterisation of surface texture, CIRP Ann. **49**(2), 635–652 (2000)
6.190 M. Stedman: Basis for comparing the performance of surface measuring machines, Precis. Eng. **9**, 149–152 (1987)
6.191 D.J. Whitehouse: *Handbook of Surface and Nanometrology*, 2nd edn. (CRC, Boca Raton 2011)
6.192 T.R. Thomas: *Rough Surfaces*, 2nd edn. (Imperial College Press, London 1999)
6.193 K.J. Stout, L. Blunt: *Three-Dimensional Surface Topography* (Penton, London 2000)
6.194 ISO 1302:2002 Geometrical Product Specifications (GPS) – Indication of surface texture in technical product documentation (ISO, Geneva 2002)
6.195 ISO 3274:1996 Geometrical Product Specifications (GPS) – Surface texture: Profile method – Nominal characteristics of contact (stylus) instruments (ISO, Geneva 1996)
6.196 ISO 4287:1997 Geometrical Product Specifications (GPS) – Surface texture: Profile method – Terms, definitions and surface texture parameters (ISO, Geneva 1997)
6.197 ISO 4287:1997/Amd1:2009 Peak count number (ISO, Geneva 1997)
6.198 ISO 4288:1996 Geometrical Product Specifications (GPS) – Surface texture: Profile method – Rules and procedures for the assessment of surface texture (ISO, Geneva 1996)
6.199 ISO 5436-2:2001 Geometrical Product Specifications (GPS) – Surface texture: Profile method; Measurement standards – Part 2: Software measurement standards (ISO, Geneva 2001)
6.200 ISO 8785:1998 Geometrical Product Specification (GPS) – Surface imperfections – Terms, definitions and parameters (ISO, Geneva 1998)
6.201 ISO 11562:1996 Geometrical Product Specifications (GPS) – Surface texture: Profile method – Metrological characteristics of phase correct filters (ISO, Geneva 1996)
6.202 ISO 12085:1996 Geometrical Product Specifications (GPS) – Surface texture: Profile method – Motif parameters (ISO, Geneva 1996)
6.203 ISO 12179:2000 Geometrical Product Specifications (GPS) – Surface texture: Profile method – Calibration of contact (stylus) instruments (ISO, Geneva 2000)
6.204 ISO 13565-1:1996 Geometrical Product Specifications (GPS) – Surface texture: Profile method; Surfaces having stratified functional properties – Part 1: Filtering and general measurement conditions (ISO, Geneva 1996)
6.205 ISO 13565-2:1996 Geometrical Product Specifications (GPS) – Surface texture: Profile method; Surfaces

having stratified functional properties – Part 2: Height characterization using the linear material ratio curve (ISO, Geneva 1996)
6.206 ISO 13565-3:1998 Geometrical Product Specifications (GPS) – Surface texture: Profile method; Surfaces having stratified functional properties – Part 3: Height characterization using the material probability curve (ISO, Geneva 1998)
6.207 ISO/TS 16610-1:2006 Geometrical product specifications (GPS) – Filtration – Part 1: Overview and basic concepts (ISO, Geneva 2006)
6.208 ISO/TS 16610-20:2006 Geometrical product specifications (GPS) – Filtration – Part 20: Linear profile filters: Basic concepts (ISO, Geneva 2006)
6.209 ISO/TS 16610-22:2006 Geometrical product specifications (GPS) – Filtration – Part 22: Linear profile filters: Spline filters (ISO, Geneva 2006)
6.210 ISO/TS 16610-28:2010 Geometrical product specifications (GPS) – Filtration – Part 28: Profile filters: End effects (ISO Geneva 2010)
6.211 ISO/TS 16610-29:2006 Geometrical product specifications (GPS) – Filtration – Part 29: Linear profile filters: Spline wavelets (ISO, Geneva 2006)
6.212 ISO/TS 16610-30:2009 Geometrical product specifications (GPS) – Filtration – Part 30: Robust profile filters: Basic concepts (ISO, Geneva 2009)
6.213 ISO/TS 16610-31:2010 Geometrical product specifications (GPS) – Filtration – Part 31: Robust profile filters: Gaussian regression filters (ISO, Geneva 2010)
6.214 ISO/TS 16610-32:2009 Geometrical product specifications (GPS) – Filtration – Part 32: Robust profile filters: Spline filters (ISO, Geneva 2009)
6.215 ISO/TS 16610-40:2006 Geometrical product specifications (GPS) – Filtration – Part 40: Morphological profile filters: Basic concepts (ISO, Geneva 2006)
6.216 ISO/TS 16610-41:2006 Geometrical product specifications (GPS) – Filtration – Part 41: Morphological profile filters: Disk and horizontal line-segment filters (ISO, Geneva 2006)
6.217 ISO/TS 16610-48:2006 Geometrical product specifications (GPS) – Filtration – Part 49: Morphological profile filters: Scale space techniques (ISO, Geneva 2006)
6.218 ISO 25178-6:2010 Geometrical product specifications (GPS) – Surface texture: Areal – Part 6: Classification of methods for measuring surface texture (ISO, Geneva 2010)
6.219 ISO 25178-601:2010 Geometrical product specifications (GPS) – Surface texture: Areal – Part 601: Nominal characteristics of contact (stylus) instruments (ISO, Geneva 2010)
6.220 ISO 25178-602:2010 Geometrical product specifications (GPS) – Surface texture: Areal – Part 602: Nominal characteristics of noncontact (confocal chromatic probe) instruments (ISO, Geneva 2010)
6.221 ISO 26178-701:2010 Geometrical product specifications (GPS) – Surface texture: Areal – Part 701: Calibration and measurement standards for contact (stylus) instruments (ISO, Geneva 2010)
6.222 ISO 1302:2002/DAmd 2 Indication of material ratio requirements (ISO, Geneva 2002)
6.223 ISO/DIS 16610-21 Geometrical product specifications (GPS) – Filtration – Part 21: Linear profile filters: Gaussian filters
6.224 ISO/CD 25178-1 Geometrical product specifications (GPS) – Surface texture: Areal – Part 1: Indication of surface texture
6.225 ISO/DIS 25178-2 Geometrical product specifications (GPS) – Surface texture: Areal – Part 2: Terms, definitions and surface texture parameters
6.226 ISO/DIS 25178-3.2 Geometrical product specifications (GPS) – Surface texture: Areal – Part 3: Specification operators
6.227 ISO/DIS 25178-7 Geometrical product specifications (GPS) – Surface texture: Areal – Part 7: Software measurement standards
6.228 ISO/DIS 25178-603 Geometrical product specifications (GPS) – Surface texture: Areal – Part 603: Nominal characteristics of noncontact (phase-shifting interferometric microscopy) instruments
6.229 ISO/DIS 25178-604 Geometrical product specifications (GPS) – Surface texture: Areal – Part 604: Nominal characteristics of noncontact (coherence scanning interferometry) instruments
6.230 ISO/CD 25178-605 Geometrical product specifications (GPS) – Surface texture: Areal – Part 605: Nominal characteristics of noncontact (point autofocusing) instruments
6.231 ISO 5436-1:2000 Geometrical Product Specifications (GPS) – Surface texture: Profile method; Measurement standards – Part 1: Material measures (ISO, Geneva 2000)
6.232 M.C. Malburg, J. Raja: Characterization of surface texture generated by plateau honing process, CIRP Ann. **42**(1), 637–639 (1993)
6.233 K.J. Stout, P.J. Sullivan, W.P. Dong, E. Mainsah, N. Luo, T. Mathia, H. Zahouani: *The Development of Methods for the Characterisation of Roughness in Three Dimensions, Report EUR 15178 EN* (European Commission, Brussels 1993)
6.234 K.J. Stout: *Three Dimensional Surface Topography, Measurement, Interpretation and Applications* (Penton, London 1994)
6.235 L. Blunt, X. Jiang: *Advanced Techniques for Assessment Surface Topography* (Penton, London 2003)
6.236 Image Metrology A/S: *Scanning Probe Image Processor (SPIP)* (Image Metrology A/S, Lyngby 2010), www.imagemet.com
6.237 P.M. Lonardo, L. De Chiffre, A.A. Bruzzone: Characterisation of functional surfaces, Proc. Int. Conf. Tribol. Manuf. Processes, ed. by N. Bay (IPL/Technical University of Denmark, Lyngby 2004)
6.238 R. Hillmann: Surface profiles obtained by means of optical methods – Are they true representa-

tions of the real surface?, CIRP Ann. **39**(1), 581–583 (1990)
6.239 P. Bariani: Dimensional metrology for microtechnology. Ph.D. Thesis (Technical University of Denmark, Lyngby 2004)
6.240 G. Binnig, C.F. Quate, C. Gerber: Atomic force microscope, Phys. Rev. Lett. **56**, 930–933 (1986)
6.241 P.M. Lonardo, D.A. Lucca, L. De Chiffre: Emerging trends in surface metrology, CIRP Ann. **51**(2), 701–723 (2002)
6.242 N. Kofod: Validation and industrial application of AFM. Ph.D. Thesis (Technical University of Denmark and Danish Fundamental Metrology, Lyngby 2002)
6.243 L. De Chiffre, H.N. Hansen, N. Kofod: Surface topography characterization using an atomic force microscope mounted on a coordinate measuring machine, CIRP Ann. **48**(1), 463–466 (1999)
6.244 H.N. Hansen, P. Bariani, L. De Chiffre: Modelling and measurement uncertainty estimation for integrated AFM-CMM instrument, CIRP Ann. **54**(1), 531–534 (2005)
6.245 J.C. Wyant, J. Schmit: Large field of view, high spatial resolution, surface measurements, Int. J. Mach. Tools Manuf. **38**(5/6), 691–698 (1998)
6.246 K. Yanagi, M. Hasegawa, S. Hara: A computational method for stitching a series of 3-D surface topography data measured by microscope-type surface profiling instruments, Proc. 3rd EUSPEN Int. Conf. 2, ed. by F.L.M. Delbressine, P.H.J. Schellekens, F.G.A. Homburg, H. Haitjema (TU Eindhoven, Eindhoven 2002) pp. 653–656
6.247 S.H. Huerth, H.D. Hallen: Quantitative method of image analysis when drift is present in a scanning probe microscope, J. Vac. Sci. Technol. **21**(2), 714–718 (2003)
6.248 G. Dai, F. Pohlenz, H.U. Danzebrink, M. Xu, K. Hasche, G. Wilkening: A novel metrological large range scanning probe microscope applicable for versatile traceable topography measurements., Proc. 4th EUSPEN Int. Conf. (euspen, Glasgow 2004) pp. 228–229
6.249 A. Boyde: Quantitative photogrammetric analysis and qualitative stereoscopic analysis of SEM images, J. Microsc. **98**, 452–471 (1973)
6.250 W. Hillmann: Rauheitsmessung mit dem Raster-Elektronenmikroskop (REM), Tech. Mess. **47**, V9116–6 (1980), in German
6.251 G. Piazzesi: Photogrammetry with the scanning electron microscope, J. Phys. E **6**(4), 392–396 (1973)
6.252 O. Kolednik: A contribution to stereo-photogrammetry with the scanning electron microscope, Pract. Metallogr. **18**, 562–573 (1981)
6.253 S. Scherer: 3-D surface analysis in scanning electron microscopy, G.I.T Imaging Microsc. **3**, 45–46 (2002)
6.254 M. Schubert, A. Gleichmann, M. Hemmleb, J. Albertz, J.M. Köhler: Determination of the height of a microstructure sample by a SEM with a conventional and a digital photogrammetric method, Ultramicroscopy **63**, 57–64 (1996)
6.255 Alicona Imaging: *MeX Software* (Alicona Imaging, Graz 2008)
6.256 P. Bariani: *Investigation on Traceability of 3-D SEM based on the Stereo-Pair Technique, IPL Internal Report* (Technical University of Denmark, Lungby 2003)
6.257 P. Bariani, L. De Chiffre, H.N. Hansen, A. Horsewell: Investigation on the traceability of three dimensional scanning electron microscope measurements based on the stereo-pair technique, Precis. Eng. **29**, 219–228 (2005)
6.258 V.T. Vorburger, E.C. Teague: Optical techniques for on-line measurement of surface topography, Precis. Eng. **3**, 61–83 (1981)
6.259 G. Staufert, E. Matthias: Kennwerte der Oberflächenrauhigkeit und ihre Aussagekraft hinsichtlich der Charakterisierung bestimmter Oberflächentypen, CIRP Ann. **25**(1), 345–350 (1977), in German
6.260 S. Christiansen, L. De Chiffre: Topographic characterisation of progressive wear on deep drawing dies, Tribol. Trans. **40**, 346–352 (1997)
6.261 L. De Chiffre, H. Kunzmann, G.N. Peggs, D.A. Lucca: Surfaces in precision engineering, microengineering and nanotechnology, CIRP Ann. **52**(2), 561–577 (2003)
6.262 ISO: *International Vocabulary of Basic and General Terms in Metrology* (ISO, Geneva 1993)
6.263 H. Haitjema, M. Morel: Traceable roughness measurements of products, Proc. 1st EUSPEN Top. Conf. Fabr. Metrol. Nanotechnol., Vol. 2, ed. by L. De Chiffre, K. Carneiro (IPL/Technical University of Denmark, Lyngby 2000) pp. 373–381
6.264 R. Leach: *Calibration, Traceability and Uncertainty Issues in Surface Texture Metrology. NPL report CLM 7* (National Physical Laboratory, Teddington 1999)
6.265 L. Koenders, J.L. Andreasen, L. De Chiffre, L. Jung, R. Krüger-Sehm: Supplementary comparison euromet, L-S11 comparison on surface texture, Metrologia **41**, 04001 (2004)
6.266 EAL G20: *Calibration of Stylus Instruments for Measuring Surface Roughness*, 1st edn. (European Cooperation for Accreditation, Paris 1996) pp. 1–9
6.267 N. Kofod, J. Garnaes, J.F. Jørgensen: Calibrated line measurements with an atomic force microscope, Proc. 1st EUSPEN Topical Conf. Fabrication and Metrology in Nanotechnology, Vol. 2 (2000) pp. 373–381
6.268 N. Kofod, J.F. Jørgensen: Methods for lateral calibration of Scanning Probe Microscopes based on two-dimensional transfer standards, Proc. 4th Semin. Quant. Microsc. (QM), Semmering, ed. by K. Hasche, W. Mirandé, G. Wilkening (PTB, Braunschweig 2000) pp. 36–43
6.269 J. Garnaes, L. Nielsen, K. Dirscherl, J.F. Jorgensen, J.B. Rasmussen, P.E. Lindelof, C.B. Sorensen: Two-

dimensional nanometre-scale calibration based on one-dimensional gratings, Appl. Phys. A **66**, S831–S835 (1998)

6.270 R. Leach, A. Hart: *A comparison of stylus and optical methods for measuring 2-D surface texture, NPL Report CBTLM 15* (National Physical Laboratory, Teddington 2002)

6.271 R. Krüger-Sehm, J.A. Luna Perez: Proposal for a guideline to calibrate interference microscopes for use in roughness measurement, Mach. Tools Manufact. **41**, 2123–2137 (2001)

6.272 P.M. Lonardo, H. Trumpold, L. De Chiffre: Progress in 3-D surface microtopography characterization, CIRP Ann. **45**(2), 589–598 (1996)